

UNIVERSITY of CALIFORNIA

Santa Barbara

**Electronic Spectroscopy and Energy Transfer in Cadmium Selenide  
Quantum Dots and Conjugated Oligomers**

A Dissertation submitted in partial satisfaction of the  
requirements for the degree

Doctor of Philosophy

in

Chemistry

by

Artjay Javier

Committee in charge:

Professor Geoffrey F. Strouse, Chair

Professor Steven C. Buratto

Professor Bernard Kirtman

Professor Mattanjah De Vries

June 2006

The dissertation of Artjay Javier is approved.

---

Professor Steven C. Burratto

---

Professor Bernard Kirtman

---

Professor Mattanjah De Vries

---

Professor Geoffrey F. Strouse, Committee Chair

June 2006

Electronic Spectroscopy and Energy Transfer in Cadmium Selenide Quantum  
Dots and Conjugated Oligomers

Copyright © 2006

by

Artjay Javier

## **Acknowledgements**

I would like to thank my advisor, Professor Geoffrey Strouse for his guidance and use of his facilities. I would also like to thank the members in his research group for their help, especially my collaborators: Robert Meulenberg, Steven Yun, Donny Magana and Travis Jennings. I thank my committee for reviewing my work, especially Professor Bernie Kirtman, for many enlightening conversations. I thank my parents and my fiance, Melissa, for their personal support, without which this work could never have been done.

# Curriculum Vitae

Artjay Javier

## Education

1996–2000            B.S. Chemistry, University of La Verne, La Verne, CA

## Professional Employment

1997–2000            Teaching Assistant, University of La Verne, La Verne,  
CA

2000–2002            Teaching Assistant, UCSB

## Awards

2003–2004            Graduate Research Mentorship Fellowship, UCSB

## Publications

1.                    **“Synthesis and Characterization of a 1:6 Au-CdSe Nanocomposite.”** Scott L. Cumberland, Mia G. Berrettini, Artjay Javier, Geoffrey F. Strouse, *Chemistry of Materials*, (2003), 15(5); 1047-1056.
2.                    **“Quantum Dot-Organic Oligomer Nanostructures: Electronic Excitation Migration and Optical Memory Design”** Artjay Javier, C. Steven Yun, Geoffrey F. Strouse, *Materials Research Society Symposium Proceedings*, (2003), Vol. 776, Q2.1.1

3. **“Nanosecond Exciton Recombination Dynamics in Colloidal CdSe Quantum Dots Under Ambient Conditions”** Artjay Javier, Donny Magana, Travis Jennings and Geoffrey F. Strouse, *Applied Physics Letters*, (2003), 83, 1423
4. **“Inorganic Clusters as Single Source Precursors for Preparation of CdSe, ZnSe, CdSe/ZnS Nanomaterials.”** Scott L. Cumberland, Khalid M. Hanif, Artjay Javier, Greg A. Khitrov, Geoffrey F. Strouse, Stephen M. Woessner, C. Steven Yun, *Chemistry of Materials*, (2002), 14, 1576-1584.
5. **“Activated and Intermittent Photoluminescence in Thin CdSe Quantum Dot Films”** Artjay Javier, Geoffrey F. Strouse, *Chemical Physics Letters*, (2004), 391, 60-63.
6. **“Energy Transport in CdSe Nanocrystals Assembled with Molecular Wires.”** Artjay Javier, C. Steven Yun, Joseph Sorena, G.F. Strouse. *Journal of Physical Chemistry, B*, (2003), 107, 435-442.
7. **“Photothermal Melting and Energy Migration in Conjugated Oligomer Films with CdSe Quantum Dots,”** Artjay Javier, Robert W. Meulenberg, C. Steven Yun, Geoffrey F. Strouse, *Journal of Physical Chemistry, B.*, (2005), 109, 6999-7006.
8. **“Nanometal Surface Energy Transfer in Optical Rulers,**

**Breaking the FRET Barrier,”** C. Steven Yun, Artjay Javier, Travis Jennings, Melissa Fisher, Steven Hira, Stacey Peterson, Ben Hopkins, Norbert O. Reich, and Geoffrey F. Strouse, *Journal of the American Chemical Society*, (2005), 127(9), 3115-3119

9. **“Optically Probed Molecular Adsorption on Nanoscale CdSe Surfaces,”** Melissa Fisher, Artjay Javier, Joseph Sorena, Geoffrey F. Strouse (manuscript in preparation).
10. **“Maximum Entropy Analysis of CdSe Quantum Dot Lifetimes,”** Artjay Javier, Travis Jennings, Geoffrey F. Strouse (manuscript in preparation).
11. **“Time-resolved Size-dependent Energy Transfer in Quantum Dot/Molecular Wire Assemblies”** Artjay Javier, Geoffrey F. Strouse (manuscript in preparation).

## **Abstract**

Electronic Spectroscopy and Energy Transfer in Cadmium Selenide Quantum  
Dots and Conjugated Oligomers

by

Artjay Javier

The electronic excited state kinetics of CdSe quantum dots (QD) are studied through optical spectroscopy, by subjecting the quantum dots to different experimental conditions, as well as coupling them to phenylene-ethynylene oligomers. CdSe QDs feature a quantum-confined exciton state which pursues a variety of pathways once formed, such as band-edge recombination, charge separation by trapping at the dot surface, and electronic energy transfer (EnT). These phenomena are studied using different CdSe sizes, highlighting the effects of quantum confinement and surface energies on exciton decay.

The size dependence of the exciton lifetime is studied, and correlation of the radiative lifetime to theoretical expectations are found, as well as evidence that nonradiative relaxation through crystal vibrations follows the Energy Gap Law and Marcus Inverted Region kinetics. A detailed analysis of the lifetime decays using the Maximum Entropy Method (MEM) reveal the presence of distributed, dual excited states, which are assigned to band-edge recombination and charged exciton decay. Complementary time-resolved PL allows for direct measurement of excited state populations, which changes dramatically upon



addition of an inorganic capping layer to the QD, reflecting the suppression of surface carrier trapping. A strong excitation power-dependence of the photo-activated photoluminescence (PL) is correlated to the established observation of PL intermittency.

Forming a hybrid nanocomposite of CdSe QDs and phenylene-ethynylene oligomers allows a detailed study of EnT between the organic phase and the inorganic phase, as well as complex energy migration kinetics within the organic phase. The size-dependent, and chain length-dependent EnT is found to arise from the spectral overlap dependence between the phases. Finally, CdSe QDs are mixed into phenylene-ethynylene oligomers at dopant-level concentrations to study the photo-induced phase transformations and subsequent electronic energy migration. A rudimentary example of using this material for all-optical memory devices is shown.

# Contents

<b>Contents</b>	<b>x</b>
<b>List of Figures</b>	<b>1</b>
<b>1 Excited States of Semiconductor Quantum Dots</b>	<b>9</b>
1.1 Introduction . . . . .	9
1.2 Electronic Structure of Quantum Dots . . . . .	10
1.2.1 Nanomaterial Nomenclature . . . . .	10
1.2.2 Quantum Confinement . . . . .	11
1.2.3 Electron States . . . . .	12
1.2.4 Hole States . . . . .	13
1.2.5 Exciton States . . . . .	14
1.3 The Confinement Potential . . . . .	16
1.3.1 Particle-in-a-box Energies . . . . .	16
1.3.2 Oscillator Strength . . . . .	18
1.4 Carrier Interactions . . . . .	20
1.4.1 Coulombic Interaction . . . . .	20
1.4.2 Exchange Interaction . . . . .	22
1.5 Particle-in-a-sphere Model . . . . .	23
1.5.1 The Wavefunctions . . . . .	23
1.5.2 The Hamiltonian . . . . .	24

1.5.3	SCF Iterations . . . . .	26
1.5.4	Example SCF Calculations . . . . .	28
1.6	Chapter Overview . . . . .	30
<b>2</b>	<b>Time-Resolved Size-Dependent CdSe Quantum Dot Lifetimes</b>	<b>35</b>
2.1	Introduction . . . . .	35
2.2	Experimental Details . . . . .	38
2.3	Fitting and Data Analysis . . . . .	38
2.4	Chapter Summary . . . . .	43
<b>3</b>	<b>Maximum Entropy Analysis of CdSe Quantum Dot Lifetimes</b>	<b>45</b>
3.1	Introduction . . . . .	45
3.2	Experiment and Analysis . . . . .	50
3.2.1	Sample Preparation, Instrumentation and Analysis Software . . . . .	50
3.2.2	The Problem of Assessing Lifetime Distributions . . . . .	52
3.2.3	The Solution Offered by the Maximum Entropy Method . . . . .	56
3.3	Results . . . . .	59
3.3.1	CdSe Quantum Dots: Bare Core . . . . .	59
3.3.2	CdSe/ZnS Quantum Dots: Core-Shell . . . . .	62
3.4	Discussion . . . . .	66
3.4.1	A 4-state model . . . . .	66
3.4.2	Comparison to Single-Dot Studies . . . . .	70
3.5	Chapter Summary . . . . .	73
<b>4</b>	<b>Photoluminescence Activation and Intermittency</b>	<b>75</b>
4.1	Introduction . . . . .	75
4.2	Experimental Details . . . . .	76
4.3	Power-dependence of Carrier Processes . . . . .	77
4.3.1	Internal Nonradiative Quenching . . . . .	77

4.3.2	Photobrightening . . . . .	78
4.4	Charge Carrier Kinetics . . . . .	78
4.4.1	Curve Fitting Procedure . . . . .	78
4.4.2	Power-dependence for a Single Size . . . . .	80
4.5	Chapter Summary . . . . .	87
<b>5</b>	<b>Electronic Energy Transfer in a Semiconductor Nanocrystal - Molecular Wire Assembly</b>	<b>89</b>
5.1	Introduction . . . . .	89
5.2	Experimental Methods . . . . .	93
5.2.1	Synthesis of the CdSe Nanocrystals and the Organic Molecular Wires . . . . .	93
5.2.2	Sample Preparation for Optical Experiments . . . . .	94
5.3	Physical Characterization of CdSe/OPE-1 structures . . . . .	96
5.3.1	Electron Microscopy . . . . .	96
5.3.2	Optical Spectroscopy . . . . .	96
5.4	Results of Optical Studies . . . . .	98
5.4.1	Scaffolding of the CdSe Nanocrystals . . . . .	98
5.4.2	Photoluminescence Spectra . . . . .	100
5.5	Size-dependent energy transfer . . . . .	105
5.5.1	The Förster Model . . . . .	105
5.5.2	Higher Order Transitions . . . . .	112
5.5.3	Energy Migration . . . . .	115
5.5.4	Chapter Summary . . . . .	118
<b>6</b>	<b>Time-resolved Size-dependent Energy Transfer in Quantum Dot/Molecular Wire Assemblies</b>	<b>119</b>
6.1	Introduction . . . . .	119
6.1.1	Energy Migration Pathways . . . . .	121
6.2	Experiment . . . . .	125
6.3	Results . . . . .	126

6.4	Discussion . . . . .	133
6.5	Chapter Summary . . . . .	138
<b>7</b>	<b>Photothermal Melting and Energy Migration of Quantum-Dot-doped Organic Oligomer Films</b>	<b>139</b>
7.1	Introduction . . . . .	139
7.2	Experimental Details . . . . .	143
7.3	Structural Characterization . . . . .	145
7.3.1	DSC Analysis . . . . .	145
7.3.2	XRD Analysis . . . . .	150
7.4	Optical Characterization . . . . .	150
7.4.1	Raman Analysis . . . . .	150
7.4.2	PL Spectra Fitting Method . . . . .	152
7.4.3	PL Spectra Analysis . . . . .	153
7.4.4	PL Temperature Dependence . . . . .	156
7.5	Optical Manipulation . . . . .	159
7.6	Energy Transfer . . . . .	164
7.6.1	Application: Optical Memory . . . . .	168
7.7	Chapter Summary . . . . .	170
	<b>Bibliography</b>	<b>172</b>

# List of Figures

1.1	Extinction spectra of CdSe quantum dots coated in HDA of differing sizes ranging from 2.0 nm to 8.0 nm (bottom to top) derived from the size-scaled absorbance spectra. . . . .	21
1.2	Wavefunctions and radial probability distributions (insets) for a spherical quantum dot with parameters: $m_e = m_h = 1$ , $R = 50\text{bohr}$ , $s = 1$ , $\epsilon = 1$ , $V = 100$ , for the spherically symmetric $n = 1, 2, 3$ states (top to bottom). . . . .	29
1.3	An example SCF iteration for a spherical CdSe quantum dot for the 1S orbitals of the hole (left column) and electron (right column) as the iteration proceeds from start to finish (top to bottom). Parameters: $m_e = 0.13$ , $m_h = 0.4$ , $\epsilon = 10.6$ , $R = 20b$ , $s = 0.25b$ , $V_h = V_e = 100h$ . . . . .	31
1.4	A plot of the energies of a spherical CdSe quantum dot as a function of iteration (correction number) for holes and electrons corresponding to the wavefunctions in Fig. 1.3. . . . .	32
2.1	Representative data for the CdSe quantum dot sizes studied ( $\lambda_{exc} = 320\text{nm}$ , $20W$ , $\sim 10\text{ps pulse}$ ). a) Transient photoluminescence of a $22\text{\AA}$ radius CdSe quantum dot in toluene at room temperature, using a moving time average, from bottom to top, from $t=6\text{ns}$ , $18\text{ns}$ , $31\text{ns}$ , $39\text{ns}$ , $48\text{ns}$ , $60\text{ns}$ , $72\text{ns}$ , $85\text{ns}$ , $93\text{ns}$ and $106\text{ns}$ . There is a $\sim 20\text{meV}$ shift (vertical lines) to higher energy at longer times. b) Semi-log plot of time-resolved photoluminescence shown with a bi-exponential fit overlaid (white line) for CdSe $22\text{\AA}$ radius (upper curve) and CdSe $26\text{\AA}$ radius (lower curve). . . . .	37

2.2	a) cw-PL quantum yields (in percentage) as a function of CdSe radius (a). b) fractional contribution of the fast component ( $f_{fast}$ ) to the pre-exponentials ( $I_{fast}(0)/I_{total}(0)$ ) from the bi-exponential fits to the lifetimes. c) The lifetimes extracted from the bi-exponential fitting. . . . .	39
2.3	Radiative and nonradiative decay rates extracted from correlation of the quantum yields and the luminescence lifetimes. a) A plot of the radiative rate components versus the inverse cube of the radius (a), where the lines represents a $\sim a^{-3}$ fits. Closed circles correspond to the fast lifetime component and the open circles, the slow component. a) A plot of the natural logarithm of the nonradiative rate versus the energy gap (lowest energy absorption feature), with a linear fit for the slow component (BEE, lower curve) and a quadratic fit, meant only as a guide to the eye, for the fast component (CE, upper curve). . . . .	41
3.1	Streak image taken of a CdSe QD( $a=22\text{\AA}$ ) where cw-PL spectra can be taken by binning pixels vertically (a) or Time-resolved decays can be taken by binning pixels horizontally (b). The excitation pulse is also shown in (b) . . . . .	51
3.2	Comparison of 3 different fitting techniques for PL lifetime data for CdSe( $a=22\text{\AA}$ )-TOP(O) dissolved in toluene. a) PL decay traces are fit to a bi-exponential, a stretched exponential ( $\beta=0.67$ ) and a distribution function given by the MEM-NLS algorithm. b) An expanded view of the tail of the decay trace in shown in a). c) the residuals for the fits given in a). . . . .	53
3.3	The William-Watts distribution function ( $f_{WW}(\tau, \beta)$ ), evaluated at different values of the stretching parameter ( $\beta$ ) . . . . .	55
3.4	A comparison of the 3 distributions used in Fig. 3.2 for CdSe( $a = 22\text{\AA}$ ) taken at all PL energies observed. The biexponential distribution ( $f_{Bi}(\tau)$ ) is shown as the black bars, the stretched distribution ( $f_{WW}(\tau)$ ) is shown as the dashed line and the MEM-NLS distribution is shown by the solid line. . . . .	60

3.5	Transient PL data for CdSe( $a=22 \text{ \AA}$ ) analyzed in terms of PL energies centered at I(2.07eV), II(2.12eV), III(2.18eV), IV(2.23eV), V(2.30eV). a) shows the normalized decay traces for these energies. b) shows the time-averaged PL, where the shaded areas show the regions being probed in this figure. c) shows the MEM-NLS fits for I,II,III,IV and V. . . . .	62
3.6	The MEM-NLS distribution function for CdSe QD ( $a=22 \text{ \AA}$ ) (dotted line) and after it was capped with a ZnS layer (solid line). Inset: CdSe/ZnS QD ( $a=22 \text{ \AA}$ ) lifetime decay trace. The 2 sharp drops in intensity at 60ns and 80ns observed are artifacts originating from damaged channels in the MCP . . . . .	63
3.7	Transient PL data for CdSe/ZnS( $a=22 \text{ \AA}$ ) analyzed in terms of PL energies centered at I(2.17eV), II(2.24eV) and III(2.33eV). a) shows the normalized decay traces for these energies. b) shows the time-averaged PL, where the shaded areas show the regions being probed in this figure. c) shows the MEM-NLS fits for I,II,III and the dotted line is a guide to the eye, centered on the peak of I. . . . .	65
3.8	Summarized model for CdSe excited states. Shown are the Crystal Ground State (CGS), the Band Edge Exciton State (BEE), the Charged State (CS) wherein the exciton is split as a charge carrier becomes trapped outside the dot, and the Charged Exciton (CE) which forms due to secondary light absorption by the CS. Solid lines represent radiative transitions such as absorption and spontaneous emission ( $k_{r,BEE}, k_{r,CE}$ ) from each state. Dotted lines indicate possible nonradiative paths for different states and include carrier trapping( $k_{trap}$ ), Auger-processes, ( $k_{Auger}$ ) and intrinsic BEE decays ( $k_{nr,BEE}$ ). . . . .	67
4.1	Normalized peak intensity of CdSe( $a \sim 25 \text{ \AA}$ ) thin film PL under exposure to laser light ( $\lambda_{exc}=488.0\text{nm}$ ) and air at room temperature. White dotted line represents a multi-exponential fit with residuals fit shown at the bottom. Inset: Thin film PL and solution-phase extinction spectrum. White line represents a gaussian fit. . . . .	79



4.2	a) Normalized peak PL intensity of thin CdSe ( $a \sim 25\text{\AA}$ ) film tracked over exposure time to light and air at different powers: I( $5\text{ W/cm}^2$ ), II( $13\text{ W/cm}^2$ ), III( $28\text{ W/cm}^2$ ), IV( $114\text{ W/cm}^2$ ), V( $161\text{ W/cm}^2$ ), VI( $266\text{ W/cm}^2$ ). b) Inverse brightening times (closed circles) and inverse decay times (open circles) extracted from fitting data in a). c) The slower inverse brightening time from a). Error bars appear on all the points in (b) and (c), though not are all seen since some are comparable to the magnitude of the marker size. . . . .	81
4.3	a) Peak energy of PL of thin CdSe ( $a \sim 25\text{\AA}$ ) film tracked over exposure time to light and air at different powers: I( $5\text{ W/cm}^2$ ), II( $13\text{ W/cm}^2$ ), III( $28\text{ W/cm}^2$ ), IV( $114\text{ W/cm}^2$ ), V( $161\text{ W/cm}^2$ ), VI( $266\text{ W/cm}^2$ ). b) Inverse time constants for blue shift (closed circles) and red shifts (open circles) extracted from fitting data in a). c) The slower inverse blue shift time constants from a). .	83
4.4	a) Bright intervals extracted from residuals similar to Fig. 4.1. b) Histogram of the bright intervals obtained from a) with an exponential (solid line) and power law (dashed line) fit. c) Bright interval time constant ( $\tau_{On}$ ) extracted from exponential fits to histograms like b) (left axis). Percentage of fluctuating spectra (right axis). d) Correlation diagram between the bright interval time ( $\tau_{On}$ ) in c) and the fast brightening time ( $\tau_{b,f}$ ) in Fig. 4.2B . . . . .	85
5.1	Room temperature absorbance (dashed) and photoluminescence (solid) spectra for a series of CdSe nanocrystals coated with TOP/TOPO (diameters given at the right) in toluene. The two prominent exciton transitions are shown. . . . .	91
5.2	TOP: Scheme of CdSe-OPE-n assemblies. CdSe nanocrystals, coated with TOP/TOPO, form amorphous, cross linked assemblies by ligand exchange of the phosphine by the thiol moiety when reacted with OPE-n: oligo-(p-phenylethynylene dibenzylthiol dipropyl ether) (OPE-n, n= 0, 1, 3) BOTTOM: Lewis structure of OPE-n molecules. . . . .	95

5.3	Transmission Electron micrography of CdSe-OPE-n nanocrystal assemblies. TOP: TEM of CdSe-OPE-3 assembled structures. An aggregate of CdSe-OPE is suspended over one a hole of the carbon grid. BOTTOM: Small Angle Electron Diffraction (SAED) pattern from TEM. The observed rings indicate incorporation of wurzite CdSe into the composite without long range ordering of the CdSe nanocrystals. . . . .	97
5.4	Photoluminescence spectra of thin films of OPE-n (top row) and CdSe-OPE-n assemblies at room temperature ( $\lambda_{exc} = 325nm, \sim 1mW$ ). Columns pertain to OPE-n sizes (n=0, 1, 3) while rows indicate CdSe NC diameters in nanometers. Arrows indicate the expected position of nanocrystal luminescence . . . . .	99
5.5	Concentration-dependent photoluminescence spectra of OPE-1 in toluene at room temperature ( $\lambda_{exc}=325nm, \sim 1mW$ ). Inset: Room temperature absorption Spectra of OPE-1 in toluene at the corresponding PL concentrations. Note that both have been normalized to the absorption or luminescence of the molecular species. . . . .	101
5.6	Excitation energy diagram for OPE (left) and CdSe (right). The electronic excitation energies of the singlet states have been estimated from the crossing of the absorption and luminescence curves. The exciton energy for the ( $1S_{3/2} - 1S_e$ ) has been estimated from the exciton maximum in the absorbance spectrum, and is shown along with the continuum of gap states. . . . .	106
5.7	Left: The luminescence of OPE-1-protected Film, the absorption of CdSe in toluene at 298K and the spectral overlap integral (filled in) for three representative sizes of CdSe. Top: Plot of $\langle J \rangle$ for OPE-1 (closed circles) and OPE-3 (open circles). . . . .	112
5.8	Excitation is generated as a molecular exciton which then can migrate to a dimer, delocalize into an excimer or polaron-pair, B, or delocalizes/migrates to an aggregate exciton, D. All three species, molecular exciton, excimer/dimer, and aggregate can transfer energy to the nanocrystal (A,C,E). F is the back-transfer of energy from the nanocrystal to the aggregate. . . . .	117

6.1	Diagram of all possible energy transfer pathways. $k_2$ :migration from single to dimer, $k_n$ :migration from dimer to aggregate, $k_{EnT1}$ :transfer from single to CdSe, $k_{EnT2}$ :transfer from dimer to CdSe, $k_{BT2}$ :back transfer from CdSe to dimer, $k_{BTn}$ :back transfer from CdSe to aggregate . . . . .	121
6.2	Time-resolved PL decay of OPE-1p in a dilute toluene solution (dashed line) and as a drop-cast film (solid line). Inset: Transient PL spectra of OPE-1p film in 2 time regimes (0-100ps and 2-8ns) and OPE-1p dissolved in toluene. . . . .	127
6.3	Time-resolved PL decay of CdSe QDs of sizes 2.8nm, 4.0nm, 4.6nm and 5.6nm shown in descending order. The corresponding total PL spectra taken from the time-resolved experiment are shown in the inset . . . . .	128
6.4	Time-resolved PL decay of OPE-1/CdSe assemblies containing CdSe QDs with diameters of 2.8nm and 4.0nm. Insets show the transient PL spectra for the decays in 2 time regimes (0-100ps and 2-8ns) . . . . .	130
6.5	Time-resolved PL decay of OPE-1/CdSe assemblies containing CdSe QDs with diameters of 4.6nm and 5.6nm. Insets show the transient PL spectra for the decays in 2 time regimes (0-1ns and 2-140ns) . . . . .	131
6.6	Time-resolved decays of OPE-1/CdSe assemblies containing CdSe(4.6nm) and CdSe(5.6nm) wherein the contribution from directly pumped QD PL has been subtracted from the decays. Solid lines indicate fits to a function containing an exponential rise and decay . . . . .	132
6.7	MEM-NLS analysis of lifetime distributions (from top to bottom) for an OPE-1 drop-cast film, CdSe(2.8nm)/toluene, an assembly of CdSe(2.8nm)-OPE-1, CdSe(4.6nm)/toluene and an assembly of CdSe(2.8nm)-OPE-1. The solid lines indicate decaying exponential distributions while the dashed line indicates rising exponential distributions. . . . .	134
7.1	Differential Scanning Calorimetry data for OPE-1p in the drop-cast film form (Bottom) and the single crystal form (Top). Features are labelled to indicate the state-state transitions: s-l: solid-to-liquid, s-s: solid-to-solid, l-s: liquid-to-solid. . . . .	146

7.2	XRD Data used to reconstruct the morphology of single crystals of OPE-1p that formed under slow, crystallization. a) shows the electron densities at each atom b) is a 3D representation of the stacking of OPE-1p molecules and c) shows only the phenyl rings to highlight the effect of the interplane twisting within the same molecule. . . . .	149
7.3	Raman Spectroscopy of OPE-1p drop-cast film at different temperatures. Raman Spectra of OPE-1p at 298K (top) and at 420K (bottom). The frequencies of the 4 identified peaks are tracked as a function of temperature (bottom graphs). . . . .	151
7.4	PL spectra of OPE-1p under different conditions, $\lambda_{exc} = 325nm$ , unpolarized. a) Dashed: OPE-1p/toluene solution (very dilute), Solid: fit to Eqn. 7.4.2 b) OPE-1p/toluene solution (concentrated) where (a) has been subtracted. c) Spun-cast film using a dilute stock d) Drop-cast film using a dilute stock e) Drop-cast film using a concentrated stock f) Crystals that have been coarsely ground with mortar and pestle. g) Crystals formed in a chloroform solution . . . . .	154
7.5	The spectrally-integrated PL of OPE-1p drop-cast film as a function of applied temperature. The arrows indicate the direction of the heating cycle (Rise 1,2) and cooling cycle (Drop 1,2). . . . .	157
7.6	Photoluminescence spectra of OPE-1p films as a function of continuous irradiation time for spun-cast films (top) and drop-cast films (bottom). The curves (from top to bottom) represent spectra taken every 20 minutes after irradiation had begun. Insets show integrated PL Intensity as a function of irradiation time. . . . .	160
7.7	The spectrally integrated regions of the PL of OPE-1p films in 3 regions (I, II, III) shown in the insets, is plotted against continuous irradiation time for both spun-cast (top) and drop-cast (bottom) films. . . . .	162
7.8	The PL spectra of CdSe QD-doped OPE-1p films in spun-cast (left) and drop-cast (right) forms made from <i>identical</i> stock solutions, immediately after exposure to light. . . . .	165
7.9	The PL spectra of CdSe QD-doped OPE-1p drop-cast film as a function of irradiation time. The inset shows the integrated intensities in the region of OPE-1p PL and CdSe PL . . . . .	167

7.10 Digital photograph of a OPE-1p/CdSe sc-Film illuminated with UV light from a Hg-lamp where an optical mask has been used to etch "UCSB" prior to photography. Color decomposition profiles for this image are shown on the right for red and blue channels. . . . . 169

# **Chapter 1**

## **Excited States of Semiconductor**

### **Quantum Dots**

#### **1.1 Introduction**

The field of Nanomaterials[1] represents a diverse effort to develop, from a bottom-up perspective, unique materials for a wide variety of technological needs. While synthetic chemistry contributes significantly to developing novel materials in this field, the resulting physics that arise from these materials represents an important interdisciplinary challenge. The role of physical chemistry in this field is to investigate these new physical phenomena, using spectroscopy as the primary tool. Optical nanomaterials are candidates for use in applications such as solar cells, chemical sensors and information storage. A functional understanding of the electronic structure is a necessary component for engineering such devices. This chapter will discuss the aspects that are

unique to quantum dots that delineate it from the broader category of nanomaterials. The focus will be on an accurate model of quantum dot excited states, which is the unifying theme of this work. Quantum dots will be introduced in two ways in this chapter. The first description will be mostly qualitative and will include confinement effects on excited states, size-scaling laws and the particle-in-a-box model. The second description will be slightly more rigorous and quantitative

## **1.2 Electronic Structure of Quantum Dots**

### **1.2.1 Nanomaterial Nomenclature**

Some of the most dramatic and intriguing effects of quantum confinement arise from small chunks of semiconductor material, called “quantum dots” or “nanocrystals.” Nanocrystals comprises a large category of materials with the only common feature being that they are crystals that can be measured at the nanometer scale. Quantum dots form a subset of nanocrystals wherein quantum size effects are the defining feature of this class. While these two terms can be used interchangeably, the subtle difference is that not all nanocrystals demonstrate quantum size effects, while all quantum dots do, by definition.

Moreover, nanocrystals define a class within a larger body of “nanomaterials.” Nanomaterials is a supercategory containing both amorphous (“nanoparticles”) and crystalline (“nanocrystals”) materials with nanometer-sized dimensions. Within the crystalline category are dimensional sub-categories of “quan-

tum wells” (2-D films), “quantum wires” (1-D strings) and “quantum dots” (0-D particles). As an example, a small chunk of semiconductor material of CdSe with a 2-nm radius is both a quantum dot and a nanocrystal, but as the size is increased beyond the critical limit (discussed further in this chapter) then it ceases to be a quantum dot, as quantum size effects become less apparent, and as it increases beyond the nanometer dimension, it ceases to be called a nanocrystal. Beyond this size limit, it is not uncommon for these materials to be called “microcrystals” since they may fall in the micron regime, and beyond further beyond this size regime, the material is referred to as “bulk.” (3-D crystals)

The majority of the work performed is based on CdSe quantum dots within the size regime of roughly 2nm to 8nm, placing it solidly in the in the quantum dot category, and which manifest very strong confinement effects. Therefore, the following descriptions of wavefunction states apply directly only to CdSe, very weakly apply to II-VI semiconductor variants, have marginally relevant bearing on semiconductor nanoparticles as a whole, and should not in any way be applied to metal nanocrystals.

### **1.2.2 Quantum Confinement**

Quantum size effects refer to the non-intuitive changes in physical phenomena associated with a reduction in the size of the physical system beyond a critical limit. While this limit varies from system to system, it is nearly always based on the magnitude of the wavefunctions of the quantum system. Quantum confinement[2] is the phenomenon wherein shrinking the boundaries of



the physical system below the size of the wavefunction causes drastic changes in the physical properties of the material. Since the wavefunction is the origin from which quantum effects and subsequently confinement originates from, it is the most important element to understand.

### 1.2.3 Electron States

All of the electron states in a quantum dot are derived from a single subset of orbitals and atoms[2]. The interaction of the discrete atomic orbitals of cadmium with each other in CdSe will eventually lead to the formation of the conduction band. In the limit of a small number of cadmium atoms, the rudimentary conduction band is comprised of the lowest unoccupied molecular orbitals (LUMO) which are derived from cadmium's s-orbitals.  $Cd^{2+}$  has an electron configuration  $[Kr]5s^04d^{10}$  so the M.O. configuration of the C.B. has an orbital angular momentum of  $l = 0$ . Consequently, if a single electron were placed into the LUMO/C.B., it would have a spin angular momentum of  $s = 1/2$ . The interaction of the electron's spin-angular momentum ( $s = 1/2$ ) and the LUMO angular momentum ( $l = 0$ ), the so-called spin-orbit coupling will be  $J = 1/2$  since  $J = l + s$ .

It is important to note that electron wave functions will have both principal and angular momentum quantum numbers that bear some similarity to, but are not directly related to their atomic cousins. These electron wave functions are placed in a particle-in-a-box potential well, whereas their atomic variants are placed into a central potential. The resulting wave functions will have  $n$ -like and  $l$ -like characteristics, being both derived from spherical harmonics and

boundary value limitations. Conventionally these are simply referred to as  $n$  and  $L$ .

The naming structure used for quantum dot term symbols is of the form  $nL_J$  and consequently, we can label the all of the electron states starting from lowest energy as  $1S_{1/2}, 2S_{1/2}, 1P_{1/2}, 2P_{1/2}, \dots$ . As a labelling convention for most semiconductor quantum dots with a non-degenerate conduction band, the J-term of  $1/2$  is replaced with  $e$  to further indicate that this term refers to electron states rather than hole states. Therefore, for CdSe quantum dots, the naming convention for electron states appears as  $1S_e, 2S_e, 1P_e, 2P_e, \dots$

#### 1.2.4 Hole States

All of the hole states in a quantum dot are derived in a similar way as the electron states with the difference being that we start with the non-metal atom. The interaction of the discrete atomic orbitals of selenium with each other in CdSe will eventually lead to the formation of the valence band. In the limit of a small number of selenium atoms, the rudimentary valence band is comprised of the highest occupied molecular orbitals (HOMO) which are derived from selenium's  $p$ -orbitals.  $Se^{2-}$  has an electron configuration  $[Ar]4s^23d^{10}4p^6$  so the M.O. configuration of the V.B. has an orbital angular momentum of  $L = 1, 0$ , and is therefore doubly degenerate. A hole in the HOMO/V.B. ( $s = 1/2$ ) will have an electron configuration that will depend on which subband it is placed ( $L = 1$  or  $L = 0$ ). As such, the spin-orbit coupling will have two terms, each one based on a different subband:  $J = 3/2$  for  $L = 1$  and  $J = 1/2$  for  $L = 0$ . As a result, there will be two sets of hole states, one progression appearing as

$1S_{1/2}, 2S_{1/2}, 1P_{1/2}, 2P_{1/2}, \dots$  and another as  $1S_{3/2}, 2S_{3/2}, 1P_{3/2}, 2P_{3/2}, \dots$ . This scheme is complicated further by the addition of heavy hole and light hole splitting in the  $J = 3/2$  subband, making  $\Delta k \neq 0$  spectroscopic transitions (or phonon-enhanced) transitions more complicated, where  $k$  is the wavevector. The result is that there are very few good quantum numbers in this system and the spectroscopic transitions can be difficult to assign.

### 1.2.5 Exciton States

Excitons in quantum dots derive their name from their solid-state counterparts[3] with a few minor variations. In the solid-state definition, an exciton is an electron-hole pair that has localized in a crystal due to the coulombic attraction between the two partners. This entity travels through the crystal, possesses a high radiative recombination potential, and can occasionally impede electrochemical cell performance. An exciton in a quantum dot does not travel or migrate due to the size limitations of the actual crystal and has an even higher radiative recombination rate due to the resulting strong wavefunction overlap. While the electrons and holes of an exciton in a solid-state crystal feel only the periodicity of the lattice and their mutual Coulombic attraction to each other, electrons and holes in quantum dots feel a very limited lattice periodicity due to a small crystal as well as a very strong confinement potential that exceeds the Coulombic potential. Whereas the Coulomb potential lowers the energy of the system, the confinement potential increases the overall system energy. These two potential forces are at odds with each other as quantum dot size varies, with the confinement energy dominating and increasing the system energy in

small quantum dots and the Coulomb energy becoming the more dominant, stabilizing force as the dot size approaches bulk-like dimensions. In fact, the confinement potential is so overwhelming in quantum dots, that their behaviors can be accurately predicted based on this potential alone. Therefore, the only useful quantum dot exciton characteristics that are carried from their solid-state cousins are the lattice parameters and exciton bohr radius[3].

Exciton states are described as combinations between electron and hole states. The lowest energy exciton state is the “band-edge exciton” (BEE) a term that has been carried forward from solid-state terminology and represents the occasionally sharp reflectance transmission near the spectroscopic band-edge. Just as in the solid-state terminology, the band-edge transition results from the bottom of the conduction band to the top of the valence band near  $\delta k = 0$ , and is referred to as “exciton formation” when light is absorbed and “exciton recombination” when light is emitted. In the molecular sense, this is the HOMO-LUMO spectroscopic transition, or the so-called lowest energy excited states (LEES), and is phenomenologically equivalent to the “absorption” and “emission” of light. In an empirical sense, the vast majority of photoluminescence spectroscopy is based on the LEES/BEE and thus this state above all other exciton states will be the focus of our study.

Returning to our definitions of electron and hole states, we can label the BEE/LEES as  $1S_{3/2} - 1S_e$ , which is spectroscopically the strongest transition observed. The second and third highest excitons are the  $1S_{1/2} - 1S_e$  (very weak) and  $1P_{3/2} - 1P_e$  (strong).

## 1.3 The Confinement Potential

### 1.3.1 Particle-in-a-box Energies

Above all other quantum size effects, the confinement potential is the primary factor in determining size-dependent behavior in quantum dots. For actual modelling of quantum dot wave functions, a rigorous particle-in-a-sphere model is used to obtain accurate energies and wavefunctions. For the purpose of understanding the confinement effect, a particle-in-a-box description provides all of the important features that delineate it from its atomic and vibrational cousins as well as allow us to use easily obtainable solid-state and quantum constants to model the lowest energy excited state.

Using the particle-in-a-box potential, we make the approximation that the electron and hole wavefunctions will only exist within the dot boundary, which we will define as the surface of the quantum dot. The basis for this definition results from the sharp increase in dielectric constant as the wavefunction moves outward radially from semiconductor material to organic ligand and eventually vacuum. In addition, there is a loss of periodicity as the wavefunction departs the semiconductor material. Therefore, it is natural to associate the width of our box with the diameter of our particle.

For a 1-D particle-in-a-box, we will use the variable  $x$  for length, setting the origin at the center of the dot, and the parameter  $R$  as the dot radius such that the dot boundaries occur at  $x = R$  and  $x = -R$ .

Using the particle-in-a-box potential (V) of

$$V(|x| < |R|) = E_{gap} \quad (1.1)$$

$$V(|x| \geq |R|) = \infty \quad (1.2)$$

Using Schrödinger's equation for this potential, the resulting wavefunctions are

$$\Psi_n(x) = \sqrt{\frac{1}{R}} \cos\left(\frac{n\pi x}{2R}\right) \quad (1.3)$$

with the corresponding energies

$$E_n = \frac{n^2 \hbar^2 \pi^2}{8\mu R^2} + E_{gap} \quad (1.4)$$

where  $\mu$  is the reduced mass of the electron and hole.

Spectroscopically, we will be interested in direct transitions due to exciton formation or recombination. The most important of these will be the electronic transition of the band-edge exciton, which will appear as the lowest energy optical transition in the absorbance/transmission spectrum as well as the highest energy optical transition in the photoluminescence spectrum.

$$E_1 = \frac{\hbar^2 \pi^2}{8\mu R^2} + E_{gap} \quad (1.5)$$

Or, in other words, the confinement energy of a quantum dot band-edge exciton ( $E_{BEE}$ ), is the difference between the bulk energy gap and the lowest energy optical transition.

$$E_{BEE} = E_1 - E_{gap} = \frac{\hbar^2 \pi^2}{8\mu R^2} \quad (1.6)$$

The importance of this transition in the study of quantum dots cannot be understated, as it forms the basis from which new nanomaterials are optically characterized as well as the primary diagnostic tool in assessing dot size in synthetically prepared batches. Focusing on this transition, we arrive at the first scaling law for quantum dots: *In the strongly confined regime, the band edge exciton energy is inversely proportional to the square of the quantum dot radius.*

$$E_{BEE} \sim \frac{1}{R^2} \quad (1.7)$$

Correlated comparisons of structural (T.E.M.) and optical (Absorbance/ Reflectance) studies[4, 1] reveal the theoretical validity and empirical applications of this law[2].

### 1.3.2 Oscillator Strength

The oscillator strengths of all the optical transitions in quantum dots will depend on the spatial overlap of the electron and hole wavefunctions. As the size of the quantum dot decreases, we will find a proportional increase in the wavefunction overlap. This has led to the implication that oscillator strength increases with decreasing size for the first exciton. While this is theoretically true, empirically it has been found that this effect does not contribute significantly to the scaling law found for absorbance transitions of the first exciton.

In other words, if two batches of quantum dots with different sizes but possessing the same number of dots were compared, we would not find a stronger absorbance signal for the smaller batch, even though the oscillator strength is significantly stronger for the smaller size. In fact, the opposite case is observed: the absorbance strength increases with increasing quantum dot size.

To begin understanding the origin of this observation, consider the solid-state perspective of a unit cell of a quantum dot. That unit cell will have constant defined electronic transition strengths, and defined oscillator strengths that can be based on the absorption of a single photon of light. As more unit cells are added to the first, they will increase that absorption rate proportionately with the total number of unit cells. The result is that the absorption probability of a quantum dot is not only affected by wavefunction overlap but also total mass or particle volume, the latter of which has the most dramatic effect on the scaling law. The resulting second scaling law for quantum dots is: *The band edge exciton absorbance coefficient scales proportionately with the cube of the quantum dot radius.* Since sphere volume scales with the cube of the radius, so also will the absorbance rate.

$$\epsilon(\lambda) \sim R^3 \tag{1.8}$$

In our use of the particle-in-a-box description of quantum dots, we have necessarily left out an important element for assessing the oscillator strengths of electron and hole transitions having a degenerate energy level but differing angular momentum. For example, the particle-in-a-box definition can give us the oscillator strength for a  $n_e = 1$  to  $n_h = 1$  transition, but cannot give



information on a  $l_e = 1$  to  $l_h = 1$  transition. If a particle-in-a-sphere definition were used, the oscillator strength of every transition would have the additional requirement of angular dependence as manifested by including the spherical harmonic component to the wavefunctions. Once this angular overlap has been included, a complete description of the optical selection rules can be made. These selection rules are very similar to the hydrogenic atom, since s-shaped, p-shaped, d-shaped etc... wavefunctions can also be found in quantum dots.

## 1.4 Carrier Interactions

### 1.4.1 Coulombic Interaction

The coulombic attraction between the electron and hole within the exciton can be defined using Coulomb's law for charged particles

$$V_{Coulomb} = \pm \frac{q_1 q_2}{4\pi\epsilon_0\epsilon R} \quad (1.9)$$

We can define the electron and hole separation distance to be roughly proportional to the dot radius and the dielectric constant to be proportional to the bulk dielectric constant, consistent with the so-called effective mass approximation of quantum dots.

While the Coulomb force plays the primary role in exciton formation in bulk semiconductors, it plays a secondary role to quantum confinement in quantum dots. Nevertheless, its effect is more pronounced in the weakly confined size regime and provides the basis of transitioning to the bulk from the

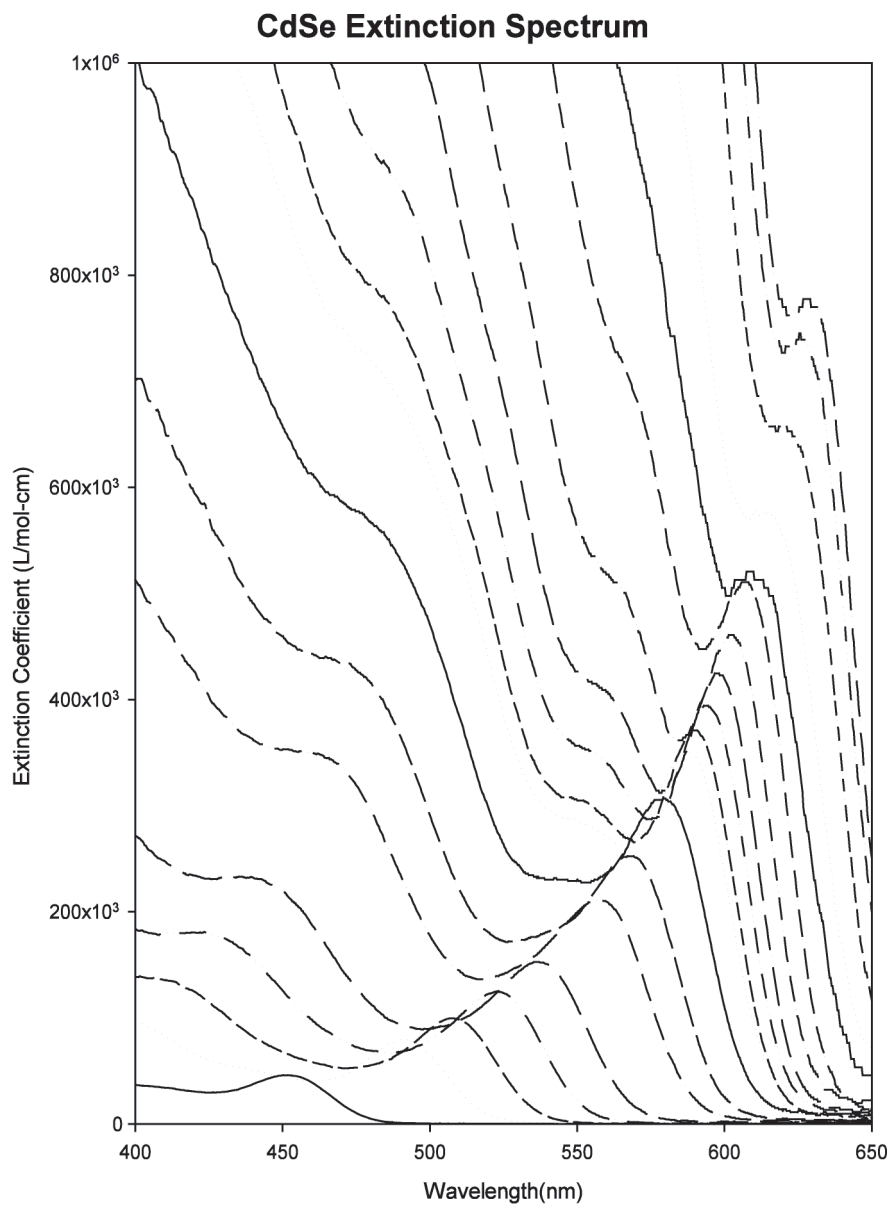


Figure 1.1. Extinction spectra of CdSe quantum dots coated in HDA of differing sizes ranging from 2.0 nm to 8.0 nm (bottom to top) derived from the size-scaled absorbance spectra.

the quantum regime in agreement with the correlation principle of quantum mechanics.

Uniting both the Coulombic effect with the confinement effect, we arrive at the Brus equation[2], which describes the band-edge energies of strongly confined quantum dots as a function of dot size.

$$E = \frac{\hbar^2 \pi^2}{2\mu R^2} - \frac{1.8}{\epsilon R} + E_{gap} \quad (1.10)$$

which has been used to accurately describe optical transitions in quantum dots. The “1.8” constant used here arises from  $1/4\pi\epsilon_0$  from Eqn. 1.9 being placed into  $eV - \text{\AA}$  units.

## 1.4.2 Exchange Interaction

In addition to the charge-based interaction of the Coulomb effect, there also exists an exchange-based interaction between the electron and hole. Similar to its atomic counterpart (electron-electron exchange), this interaction is completely quantum mechanical by nature. Moreover, the effect of this exchange interaction is incredibly small in comparison to the confinement or Coulomb interaction. Regardless, in low temperature experiments of quantum dots, the exchange interaction is pronounced and cannot be ignored[5, 6]. The resulting inclusion of the exchange interaction results in a splitting of the exciton states defining a new quantum number ( $F$ ), and a new selection rule  $\Delta F = \pm 1$  that defines optically allowed (“bright”) and optically forbidden (“dark”) transitions[7]. Under this description, the lowest energy excited state

(and thereby the emitting state) is optically forbidden, the so-called dark exciton, because it requires  $\Delta F = 2$ . However, if there is a decent amount of thermal energy present, this transition becomes allowed due to phonon participation. Since this is a 3-bodied interaction (electron, hole, phonon) it proceeds very weakly and only at high phonon density (higher temperatures). Therefore, at cryogenic temperatures, the lifetime of the band-edge exciton approaches nearly one microsecond. As the temperature is increased, the selection rule is broken both due to phonon coupling as well as thermal repopulation of the optically bright states. The energy gap between the optically bright and dark states is of the order of  $\sim 25\text{meV}$  such that at room temperature, there is a significant population of optically bright excitons.

## 1.5 Particle-in-a-sphere Model

A much more rigorous approach to examining exciton behavior in quantum dots can deliver accurate behavior and energies for a multitude of quantum dot states. One commonly used model, based on a “particle-in-a-sphere” is reviewed here, and afterward a SCF (self-consistent field) method is proposed in order to show how quantum dot energies and wavefunctions can be obtained as a function of size and varying quantum numbers.

### 1.5.1 The Wavefunctions

To study the exciton state we write out the exciton wavefunction( $\Psi_{exc}$ ) as a product wavefunction of the electron( $\Psi_e$ ) and hole( $\Psi_h$ ):

$$\Psi_{exc} = \Psi_e \Psi_h \quad (1.11)$$

The effective mass/envelope function approximation (EMA/EFA) is used for the electron and hole wavefunctions, which will be true for states that are close to the bulk conduction and valence band edges near  $k = 0$

$$\Psi_e(k, r) = \mu_{CB}(k) \psi_e(r) \quad (1.12)$$

$$\Psi_h(k, r) = \mu_{VB}(k) \psi_h(r) \quad (1.13)$$

where the bloch wavefunctions of the conduction band ( $\mu_{CB}(k)$ ) and valence band ( $\mu_{VB}(k)$ ) have been separated from from the electron ( $\psi_e(r)$ ) and hole ( $\psi_h(r)$ ) envelope wavefunctions. The envelope wavefunctions can now be calculated by solving the Schrödinger equation ( $H\Psi = E\Psi$ ). For simplicity, we show here only the spherically symmetric wavefunctions, allowing us to ignore the angular dependencies of  $\theta$  and  $\phi$ . Therefore, the following treatment will be accurate for the BEE state  $1S_{3/2} - 1S_e$  since it is S-like but will not be accurate for non-S-like states such as the  $1PS_{3/2} - 1P_e$ .

## 1.5.2 The Hamiltonian

The Hamiltonian can be written as a sum of the kinetic energy, confinement potential and coulomb potential:

$$\hat{H} = \hat{H}_{kin,e} + \hat{H}_{kin,h} + V_{Coul,e} + V_{Coul,h} + V_{conf,e} + V_{conf,h} \quad (1.14)$$

The spherically symmetric kinetic energy terms can be written as:

$$\hat{H}_{kin,e} = \frac{1}{2m_e} \left( \frac{\partial}{\partial r_e^2} + \frac{2}{r_e} \frac{\partial}{\partial r_e} + \frac{1}{r_e^2} \frac{\partial^2}{\partial r_e^2} \right) \quad (1.15)$$

$$\hat{H}_{kin,h} = \frac{1}{2m_h} \left( \frac{\partial}{\partial r_h^2} + \frac{2}{r_h} \frac{\partial}{\partial r_h} + \frac{1}{r_h^2} \frac{\partial^2}{\partial r_h^2} \right) \quad (1.16)$$

In order to obtain numerically calculable values, we choose a sigmoidal function as this possesses qualities similar to that of a particle-in-a-box and also allows for “tuning” of the “softness” of the potential barrier

$$V_{conf,e} = \frac{V_{\infty,e}}{1 + e^{-(r-R)/s}} \quad (1.17)$$

$$V_{conf,h} = \frac{V_{\infty,h}}{1 + e^{-(r-R)/s}} \quad (1.18)$$

$(V_{\infty,e(h)})$  is the potential outside the quantum dot for the electron (hole),  $R$  is the quantum dot size, and  $s$  is the softness factor, whose magnitude is directly proportional to how rapidly (in terms of length) the confinement potential changes as  $r$  approaches  $R$  radiating outward from the center of the dot. In general, it will be desirable to choose very small values of  $s$  since this will most closely resemble a particle-in-a-box potential.

The electron and hole will Coulombically interact with each other using the Hartree-Fock approximation. The Coulomb correlation potential for the electron and hole are:

$$V_{Coul}(r_e) = -\frac{1}{\epsilon} \int_0^\infty \frac{1}{|r_e - r_h|} |\psi_h(r_h)|^2 r_h^2 dr_h \quad (1.19)$$

$$V_{Coul}(r_h) = -\frac{1}{\epsilon} \int_0^\infty \frac{1}{|r_h - r_e|} |\psi_e(r_e)|^2 r_e^2 dr_e \quad (1.20)$$

To review, this Hamiltonian has seven parameters ( $m_e, m_h, \epsilon, R, s, V_{\infty,e}, V_{\infty,h}$ ) and 2 variables ( $r_e, r_h$ ). However, since we are using the effective mass approximation, we can use the bohr radius in a semiconductor ( $a_b$ ) in terms of the reduced mass of the electron and hole ( $\mu$ ) to reduce our total parameters from seven to six.

$$a_b = \frac{\epsilon}{\mu} = \epsilon \left( \frac{1}{m_e} + \frac{1}{m_h} \right) \quad (1.21)$$

Four important figures are extracted from solving the Schrödinger equation:  $E_e, \psi_e(r_e), E_h$  and  $\psi_h(r_h)$

### 1.5.3 SCF Iterations

The following simple HF-SCF method is an example of how energies and wavefunctions in quantum dots can be numerically calculated using the particle-in-a-sphere model. At the end of this section, we display a few results of what a calculation like this can generate.

In general, the SCF iterations proceed in four repeating steps, and terminate when the energies between two iterations falls below an arbitrary limit (such as 0.2%). The first step is arbitrarily started with the electron by solving Schrödinger's equation for the electron:

$$\frac{1}{2m_e} \left( \frac{\partial}{\partial r_e^2} + \frac{2}{r_e} \frac{\partial}{\partial r_e} + \frac{1}{r_e^2} \frac{\partial^2}{\partial r_e^2} \right) \psi_e(r_e) = E_e \psi_e(r_e) \quad (1.22)$$

In the second step, the wavefunctions obtained in the first step are used to calculate the Coulomb potential for the hole:

$$V_{Coul}(r_h) = -\frac{1}{\epsilon} \int_0^\infty \frac{1}{|r_h - r_e|} |\psi_e(r_e)|^2 r_e^2 dr_e \quad (1.23)$$

In the third step, the Schrödinger Equation is solved for the hole wavefunction using the hole Coulomb potential calculated in the second step:

$$\begin{aligned} \frac{1}{2m_h} \left( \frac{\partial}{\partial r_h^2} + \frac{2}{r_h} \frac{\partial}{\partial r_h} + \frac{1}{r_h^2} \frac{\partial^2}{\partial r_h^2} \right) \psi_h(r_h) + \frac{V_{\infty,h}}{1 + e^{-(r_h-R)/s}} \psi_h(r_h) \\ + V_{Coul}(r_h) \psi_h(r_h) = E_h \psi_h(r_h) \end{aligned}$$

In the fourth step, we calculate the Coulomb potential of the electron based on the hole wavefunction obtained in the third step:

$$V_{Coul}(r_e) = -\frac{1}{\epsilon} \int_0^\infty \frac{1}{|r_e - r_h|} |\psi_h(r_h)|^2 r_h^2 dr_h \quad (1.24)$$



The fifth step will be similar to the third step, except that now we will be calculating a hole potential rather than an electron potential:

$$\frac{1}{2m_e} \left( \frac{\partial}{\partial r_e^2} + \frac{2}{r_e} \frac{\partial}{\partial r_e} + \frac{1}{r_e^2} \frac{\partial^2}{\partial r_e^2} \right) \psi_e(r_e) + \frac{V_{\infty,e}}{1 + e^{-(r_e-R)/s}} \psi_e(r_e) + V_{Coul}(r_h) \psi_e(r_e) = E_e \psi_e(r_e)$$

The sixth step will identically repeat the second step, wherein a hole potential will be calculated from the electron wavefunction found in the fifth step. In general, steps 2-5 will be repeated until the energies obtained after several iterations changes by an arbitrarily small amount.

#### 1.5.4 Example SCF Calculations

The uncorrelated wavefunctions (accounting for confinement effects only, and neglecting electron-hole correlation) can be calculated. In Fig. 1.2 we show the first three spherically symmetric wavefunctions for an arbitrary quantum dot. The insets reflect the relative radial probability distributions ( $\sim |\psi(r)|^2 r^2$ ).

The confinement potential produces the desired behavior for the wavefunctions in the uncorrelated cases: each wavefunction approaches zero at the boundary,  $r = R = 50 \text{ bohrs}$ , and higher energy wavefunctions ( $n = 2, 3$ ) display the expected number of nodes ( $n - 1$ ). It is instructive to mention that if we look at the higher energy wavefunctions, we find that the their ra-

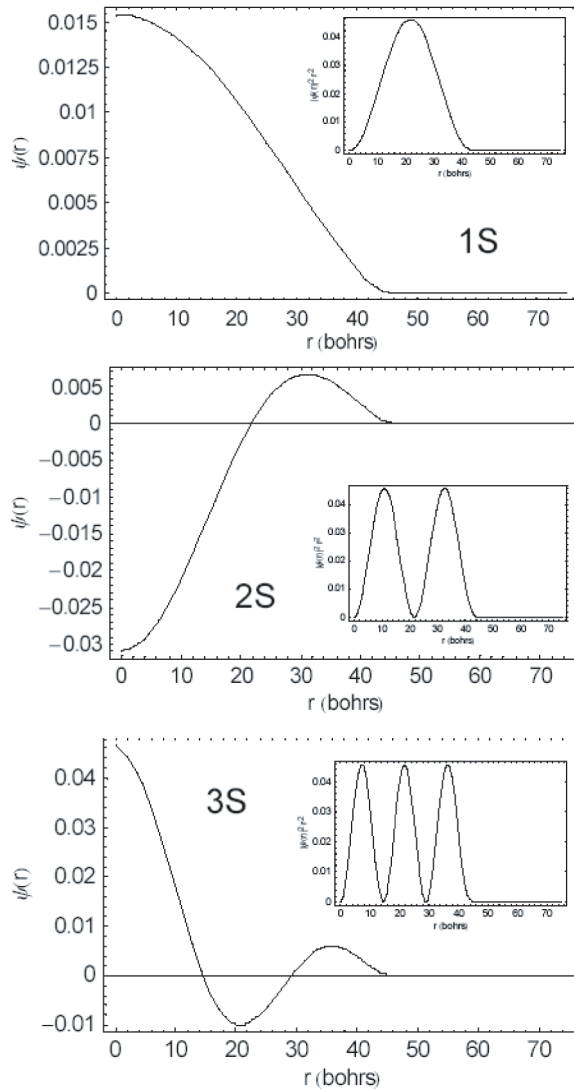


Figure 1.2. Wavefunctions and radial probability distributions (insets) for a spherical quantum dot with parameters:  $m_e = m_h = 1$ ,  $R = 50\text{bohr}$ ,  $s = 1$ ,  $\epsilon = 1$ ,  $V = 100$ , for the spherically symmetric  $n = 1, 2, 3$  states (top to bottom).

dial probability distributions display peaks (as seen in insets of Fig. 1.2 are all equally tall. This deviates from their atomic cousins wherein these peaks were all of different size, with the highest peak always being the one furthest from the nuclear center. The reason for this discrepancy arises from the shape of the potential well. In the particle-in-a-sphere potential, the confinement potential within the well is uniform, thus giving rise to equally tall peaks. In the hydrogenic atom, the potential arises through the Coulomb attraction centered at the nucleus, therefore this non-uniform potential gives rise to non-uniform peaks.

Introducing electron correlation through the Coulomb interaction between the electron and hole as performed in the recurring steps of the SCF iteration, allows us to obtain the corrected wavefunctions. An example of this iterative process is shown in Fig. 1.3 under 5 iterations. The electron and hole wavefunctions change more dramatically in the first few iterative steps (as expected) and change very little in the later iterative steps.

Within the first few iterative steps, the energy approaches a fixed value, and the change in energy between iterations quickly drops below 1%. In Fig. 1.4 the electron and hole energies are shown as a function of iteration number. As can be seen from the inset, the relative change in energy between iterations approaches 0%, making 5 iterations more than sufficient.

## 1.6 Chapter Overview

The chapters have been divided into two parts. Part I deals only with aspects studied in chemically-synthesized CdSe quantum dots, while Part II deals

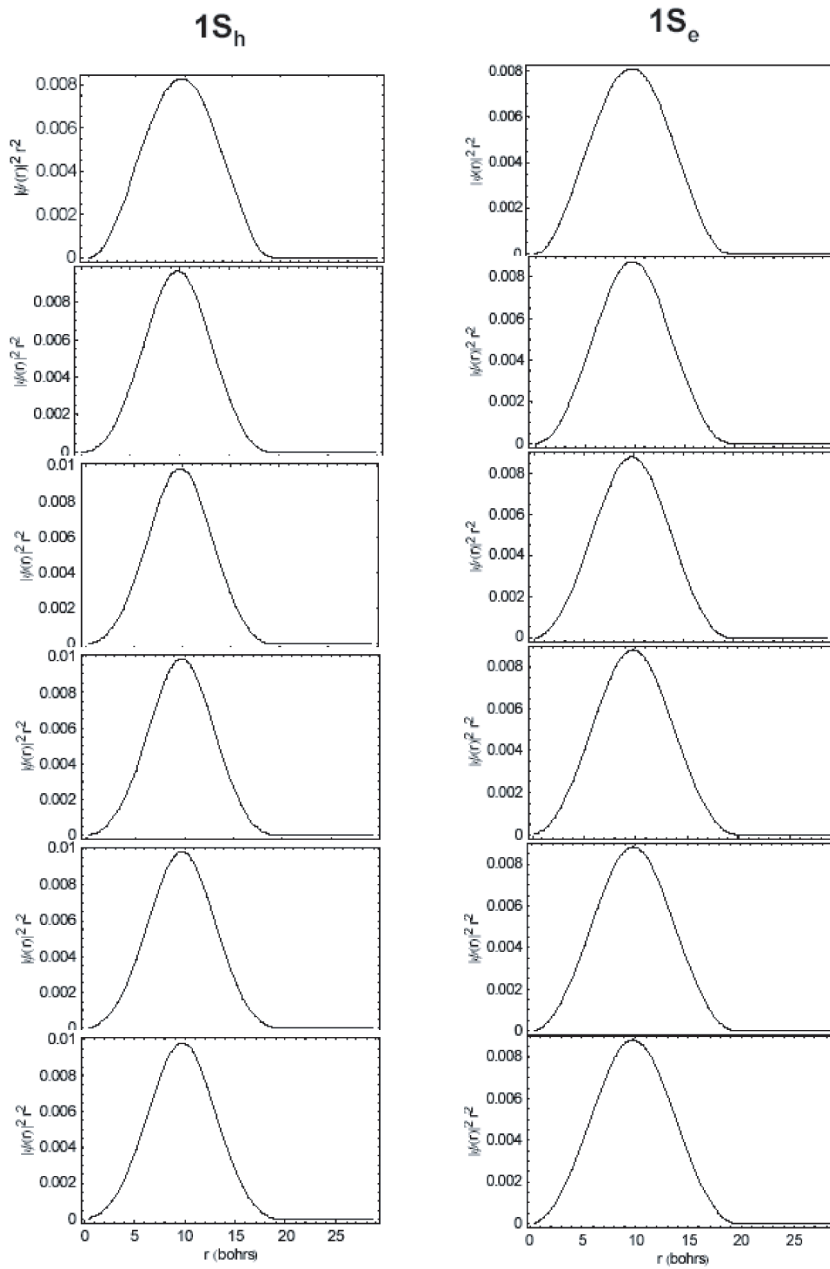


Figure 1.3. An example SCF iteration for a spherical CdSe quantum dot for the 1S orbitals of the hole (left column) and electron (right column) as the iteration proceeds from start to finish (top to bottom). Parameters:  $m_e = 0.13$ ,  $m_h = 0.4$ ,  $\epsilon = 10.6$ ,  $R = 20b$ ,  $s = 0.25b$ ,  $V_h = V_e = 100h$

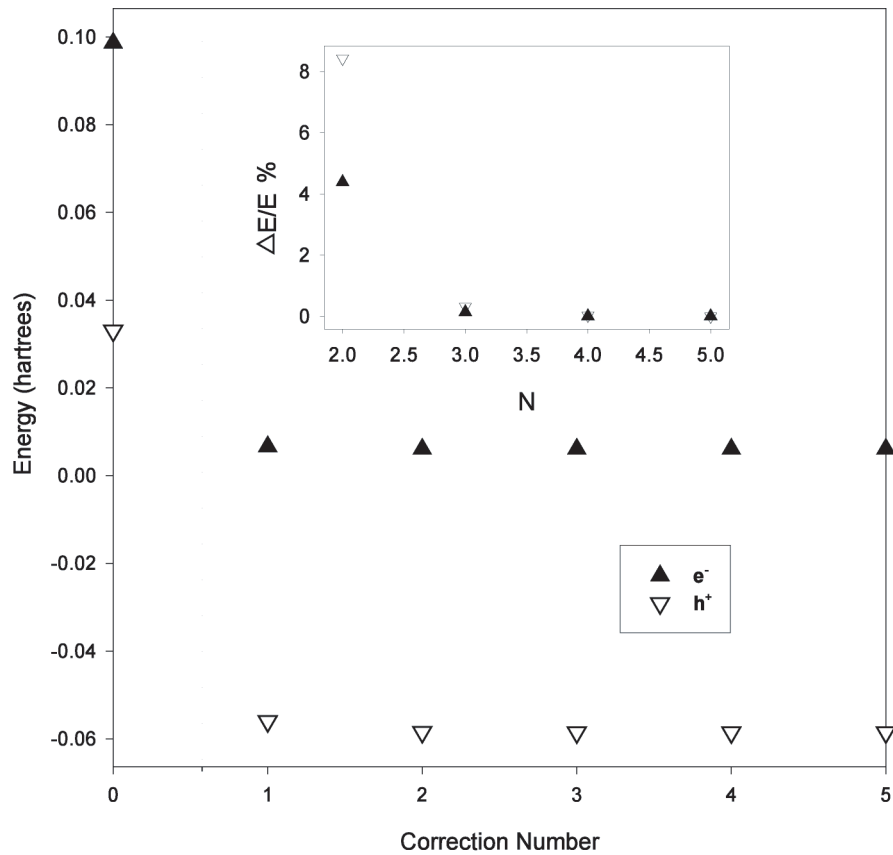


Figure 1.4. A plot of the energies of a spherical CdSe quantum dot as a function of iteration (correction number) for holes and electrons corresponding to the wavefunctions in Fig. 1.3.

with the interaction of CdSe quantum dots with organic molecular wires both in hybridized and doped forms. Chapter 2 presents a size-dependent study of CdSe Quantum Dot Lifetimes, wherein radiative and nonradiative recombination rates are shown to follow quantum confinement and lattice distortion effects, respectively. In Chapter 3, the Maximum Entropy Method is used to extract lifetime distributions from CdSe quantum dots and a comparison is made between them and a version wherein they have been coated with an inorganic passivant, ZnSe. In Chapter 4, CdSe quantum dots are studied under continuous excitation radiation under hours-long timescales to show how power-dependence can affect the complicated kinetic interplay between the band edge state and other carrier states. The unifying theme in the first four chapters is the elucidation of intrinsic quantum confinement effects as well as extrinsic surface effects through a study of the kinetics.

The remaining chapters deal with a unique combination of CdSe quantum dots and a short-chain organic polymer, where the unifying theme is the energy transfer and migration between all of the different pseudo-particle species through. Chapter 5 and 6 study a unique hybrid nanomaterial composed of CdSe quantum dots, bound tightly to organic molecular wires. Chapter 5 studies how quantum dot size and oligomer chain-length affect energy transfer and migration on the steady-state scale, while Chapter 6 elucidates how the different species involved contribute to the nanosecond timescale kinetics. Chapter 7 studies a new material wherein CdSe quantum dots have been mixed with the molecular wire film in dopant amounts. Here, a broader kinetic picture of the interplay of all the excited states, as well as the potential application for optical

memory devices is illustrated.

Topically, CdSe photophysics is the unifying theme of this entire work. Experimentally, time-resolved and energy-resolved photoluminescence is the unifying method from which all these effects are probed. Conceptually, kinetics is the unifying approach to investigating the CdSe excited states.

## Chapter 2

# Time-Resolved Size-Dependent CdSe Quantum Dot Lifetimes

Reprinted with permission from “Nanosecond Exciton Recombination Dynamics in Colloidal CdSe Quantum Dots Under Ambient Conditions” A. Javier, D. Magana, T. Jennings and G.F. Strouse, *Applied Physics Letters*, (2003), 83, 1423. Copyright 2003, American Institute of Physics.

### 2.1 Introduction

The exciton recombination dynamics of semiconductor quantum dots (QDs) of CdSe[1] have been explored in epitaxial[8] and colloidal systems[9, 10]. Following photo-induced charge separation, carriers cool[11] ( $< 200fs$ ), relax[12] ( $1 - 50ps$ ), and recombine at the band-edge[9, 10] ( $1 - 50ns$ ) with nonexponential decay dynamics at room temperature. An extrinsic effect on



the BEE can be thought of as occurring due to trapping of a charge carrier following the initial photo-excitation, preventing immediate recombination, but generating a small intra-dot electric field[13]. Within the lifetime of the trapped carrier, a second photo-excitation event can occur with subsequent radiative recombination occurring from a charged exciton (CE). It is known that carrier trapping is the primary cause for nonexponentiality in the band edge exciton (BEE) decay from single dot experiments[10]. Charged exciton photoluminescence in MBE grown quantum dots has been observed and is referred to with respect to the number of charges and charge type; however, in this study we have avoided this nomenclature since we cannot discretely assign the photo-induced carrier type[14]. A systematic study on a series of nine lyothermally prepared CdSe samples isolated from the same reaction batch[4] provide evidence that the biexponential decay process can be attributed to the independent decays of BEE and CE states. Size-dependent radiative recombination for the BEE and CE follow the cube of the size, as expected from the trends in the oscillator strengths[15]. In addition, we observe that the nonradiative recombination ( $k_{nr}$ ) for the BEE follows the energy gap law[16] (EGL) while the CE exhibits lattice perturbations arising from a behavior related to the Marcus inverted region (MIR), which results in efficient non-radiative coupling to the perturbed ground state of the charged particle. Such an effect is expected since the charging of the lattice induces Frölich coupling.

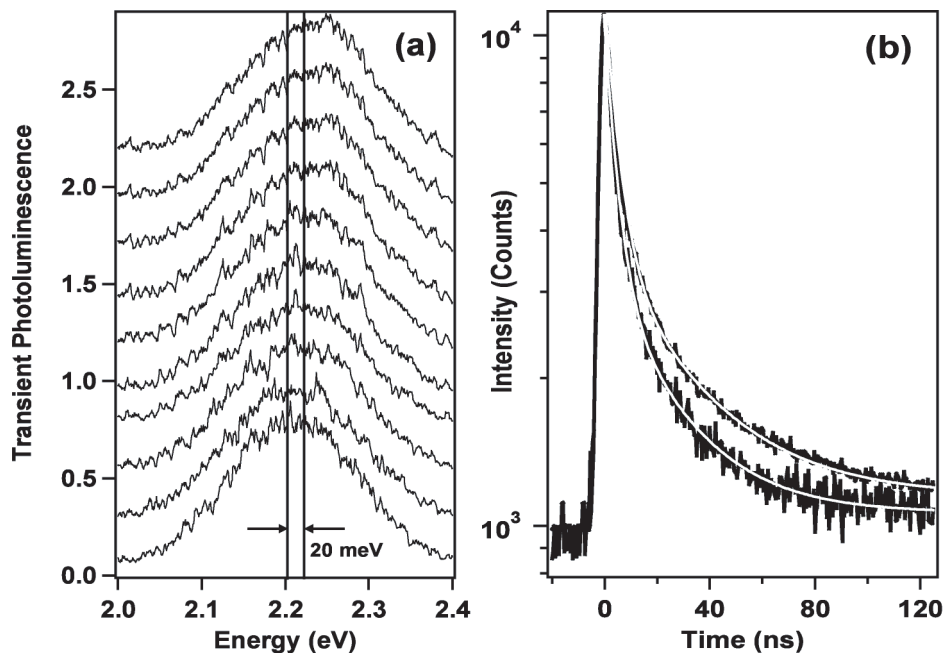


Figure 2.1. Representative data for the CdSe quantum dot sizes studied ( $\lambda_{exc} = 320nm$ ,  $20W$ ,  $\sim 10ps$  pulse). a) Transient photoluminescence of a  $22\text{\AA}$  radius CdSe quantum dot in toluene at room temperature, using a moving time average, from bottom to top, from  $t=6ns$ ,  $18ns$ ,  $31ns$ ,  $39ns$ ,  $48ns$ ,  $60ns$ ,  $72ns$ ,  $85ns$ ,  $93ns$  and  $106ns$ . There is a  $\sim 20meV$  shift (vertical lines) to higher energy at longer times. b) Semi-log plot of time-resolved photoluminescence shown with a bi-exponential fit overlaid (white line) for CdSe  $22\text{\AA}$  radius (upper curve) and CdSe  $26\text{\AA}$  radius (lower curve).

## 2.2 Experimental Details

The lyothermally prepared CdSe quantum dots possess narrow inhomogeneous linewidths ( $< 200\text{meV}$ ), with observed stokes-shifts consistent with previous studies[4] (Fig. 2.1a). Time-correlated single photon counting PL measurements were taken using  $\sim 420\text{nm}$  excitation energy,  $\sim 200\text{fs}$  wide pulses at  $\sim 1\text{kHz}$  rep. rate, with an average power of  $\sim 0.02\text{mW}$ , detected with an MCP-PMT ( $\sim 20\text{ps}$  response) and TC-SPC card. In all sizes studied, the luminescence decays were monitored at the peak of the cw-PL spectra. Transient PL measurements were taken using  $\sim 320\text{nm}$  excitation energy,  $\sim 10\text{ps}$  wide pulses at  $1\text{MHz}$  rep. Rate, with an average power of  $\sim 0.02\text{mW}$ , detected with a streak camera.

## 2.3 Fitting and Data Analysis

The time resolved traces (Fig. 2.1b) are fit to biexponential decays, consistent with observing two independent but energetically overlapping decays. This assumption is supported by the  $\sim 20\text{meV}$  shift in the PL peak at different observation times (Fig. 2.1a), indicative of two competing emissive states with different lifetimes. The shift in PL is roughly consistent with the spectral shift observed in single-dot experiments[14, 17] due to carrier trapping[18], and is analogous to the quantum confined stark effect[13]. Fits to the data reveal that the exciton lifetimes in all sizes consist of a fast component ( $\sim 1 - 3\text{ns}$ ), which we assign to the CE state, and a slow component ( $\sim 20 - 30\text{ns}$ ), assignable to the BEE state, that decrease with size (Fig. 2.2c). Time-resolved PL shifts

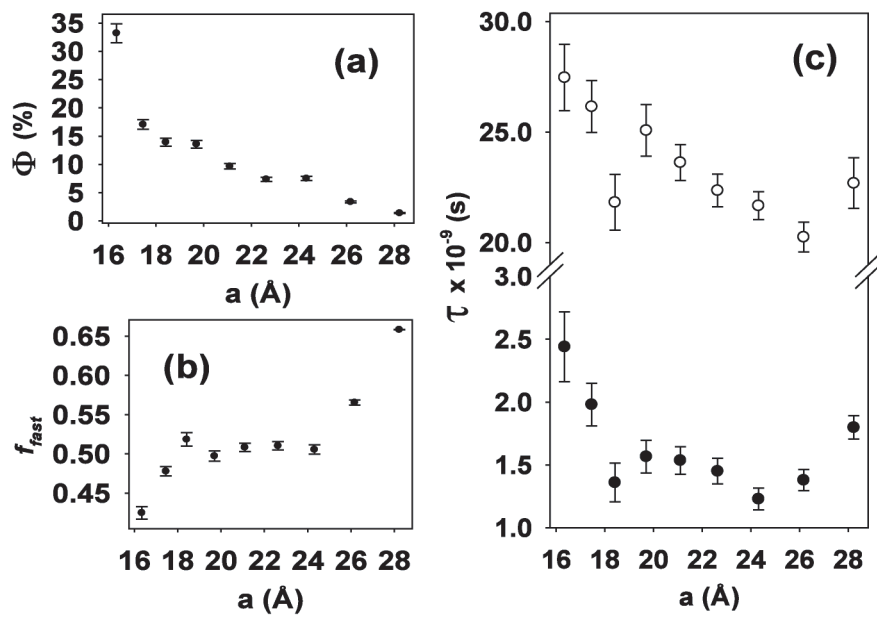


Figure 2.2. a) cw-PL quantum yields (in percentage) as a function of CdSe radius ( $a$ ). b) fractional contribution of the fast component ( $f_{fast}$ ) to the pre-exponentials ( $I_{fast}(0)/I_{total}(0)$ ) from the biexponential fits to the lifetimes. c) The lifetimes extracted from the bi-exponential fitting.

indicate that the CE emits at a lower energy than the BEE, by  $\sim 20meV$ . The pre-exponential fractions of the fast component ( $I_{fast}(0)/(I_{fast}(0) + I_{slow}(0))$ ) in Fig. 2.2b increase with size and the quantum yields[19] monotonically decrease with size from 35 to 2 (Fig. 2.2a).

With two non-interacting decays, it is straightforward to calculate the radiative lifetimes for state  $|i\rangle$ , ( $\tau_{r,i}$ ) using the total quantum yield ( $\Phi$ ) the observed lifetime ( $\tau_i$ ), and pre-exponential term ( $I_i(0)$ ) of state  $|i\rangle$  and the observed lifetime ( $\tau_j$ ) and pre-exponential ( $I_j(0)$ ) of the other state  $|j\rangle$ ,

$$\frac{1}{\tau_{r,i}} = \frac{\Phi}{\tau_i + (I_j(0)/I_i(0))\tau_j} \quad (2.1)$$

where the quantum yield for state  $|i\rangle$  is a product of the total measured quantum yield and the fraction of emitted photons coming from  $|i\rangle$ , based on the pre-exponential components and lifetimes. In general,  $> 90$  of the photons observed are emitted from the BEE state and is the major contributor to the observed photon yield. The experimental results indicate 1)  $\tau_r \sim a^3$ , 2) the  $\tau_r$ 's are very similar between the BEE and CE, and 3)  $\tau_r$ 's are much longer than predicted by oscillator strengths measured by absorption[15]. The size dependent scaling parameter for the radiative rate data (Fig. 2.3a) fits to a power-law expression ( $k_r(a) = xa^n$ ) with  $n = -2.8$  for the CE ( $n = -3.8$  for the BEE). This correlates with the predicted behavior, since the oscillator strength ( $f$ ) in CdSe quantum dots increases linearly with size[15, 20] ( $\sim a$ ), and within the strong confinement regime the exciton energy ( $E_{ex}$ ) will roughly scale inversely with the square of the size[2] ( $E_{ex} \sim 1/a^{-2}$ ). Therefore,  $k_r$ , which is a product of the energy squared and the oscillator strength[21] ( $k_r \sim E_{ex}^2 f$ ), will

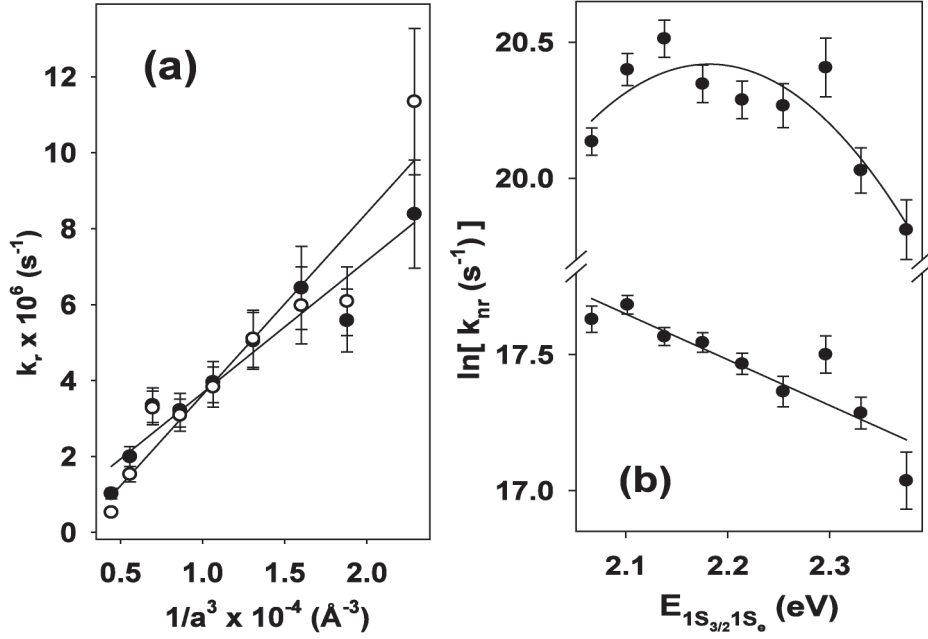


Figure 2.3. Radiative and nonradiative decay rates extracted from correlation of the quantum yields and the luminescence lifetimes. a) A plot of the radiative rate components versus the inverse cube of the radius ( $a$ ), where the lines represents a  $\sim a^{-3}$  fits. Closed circles correspond to the fast lifetime component and the open circles, the slow component. a) A plot of the natural logarithm of the nonradiative rate versus the energy gap (lowest energy absorption feature), with a linear fit for the slow component (BEE, lower curve) and a quadratic fit, meant only as a guide to the eye, for the fast component (CE, upper curve).

scale with the cube of the size ( $k_r \sim 1/a^3$ ). The similarity of the magnitude of the  $\tau_r$ 's (even as a function of size) between the two decay processes strongly imply that they are related in character but perturbed by an extrinsic process, such as the presence of a small electric field perturbation. The very long radiative lifetimes observed ( $\sim 10^2 - 10^3 ns$ ) are consistent with the confinement enhanced exciton exchange interaction[22].

The two-state model can be further supported by inspection of the non-radiative rates ( $k_{nr,i} = 1/\tau_i - 1/\tau_{r,i}$ ), (Fig. 2.3b). An exponential depen-

dence of the nonradiative rate for the long lifetime with the effective bandgap,  $\ln(k_{nr}) \sim -E_{gap}$ , (where  $E_{1S_{3/2}-1S_e} \sim E_{gap}$ ) is consistent with the EGL[16], implying that the nonradiative decay channels are dominated by phonon emission, that the lattice is harmonic over the energy range studied, and in general follows well-understood photophysics in the weak coupling limit. The EGL is an approximation derived from the Franck-Condon overlap of vibrational wavefunctions between two displaced harmonic oscillators (the excited state and the ground state) as a function of the energy difference between them. This correlation is expected for the direct-gap nature of a band-edge exciton recombination in CdSe, and allows the assignment of the long lifetime decay to the BEE in the absence of extrinsic effects.

Analysis of the short lifetime suggests it arises from the CE state, and is influenced by extrinsic surface-related effects. A plot of the short-lived state's  $k_{nr}$  (Fig. 2.3b) does not follow a completely linear dependence with  $E_{gap}$ , reaching a maximum at  $a \sim 25\text{\AA}$ , followed by a reversal in trend. This observation can be attributed to a large lattice distortion in the excited state, where vibronic overlap reaches an eventual maximum in  $k_{nr}$ . Large excited state distortions have also been found in single dot studies where fluctuating electric fields can induce strong exciton-LO phonon coupling[23]. Beyond this maximum,  $k_{nr}$  processes result primarily from thermal activation as the system has technically crossed into the Marcus inverted region (MIR). The connection between the bell-shaped MIR and linear EGL has only been recently verified[24], but can be intuitively obtained by examination of the displacement in energy of any two harmonic oscillators. The lattice distortion, which gives rise to an order of

magnitude increase in  $k_{nr}$  in the CE state (Fig. 2.3b), is most likely a result of Frölich coupling to optical phonons in the system originating from charge screening by lattice reconstruction. The existence of a donor state that perturbs BEE emission has been found in pressure-dependent studies of CdSe[25], where it has been shown that strong electron-phonon coupling to ligand vibrational states induces a minimum in the Gruneisan parameter at the same quantum dot size ( $a \sim 25\text{\AA}$ ) that a maximum appears in our nonradiative relaxation rates, supporting the presence of a strongly distorted state.

## 2.4 Chapter Summary

In conclusion, we have been able to describe the ensemble size-dependent recombination rates of a large sampling of CdSe QDs, through carrier trapping at the surface inducing a charging of the dot core which induces subsequent absorption and emission to occur under this Stark field. We find that an intrinsically long, low energy BEE recombination occurs in competition with an extrinsically short, high energy CE recombination. We show that the radiative lifetimes arise from quantum confinement through the size-dependent relationship,  $\tau_r \sim a^3$ . Although Auger relaxation effects[26] have been neglected, especially Auger photoionization[27], surprisingly, the nonradiative decays can be analyzed using an energy gap analysis (through quantum confinement) based purely on vibronic overlap, without the need to invoke other explanations for the data trend. This extrinsic lifetime decay is being probed further with varying pump rates, since Auger processes scale with carrier con-



centration. In addition, size effects were neglected in the EGL analysis, and these are likely to play a role. We conclude that the BEE follows the EGL, suggesting phonon emission to be the dominant process, while the CE follows the MIR, implying strong lattice distortion presumably due to Frölich coupling.

# Chapter 3

## Maximum Entropy Analysis of CdSe Quantum Dot Lifetimes

### 3.1 Introduction

CdSe quantum dots[1, 28, 29] (QDs) are ideal semiconductor nanomaterials for studying electronic excited state decay processes[5, 30, 8, 31], owing to their ease of preparation[4], their bandgap lying in the visible range, and their nanoseconds-long photoluminescence (PL) lifetime decay[32, 31, 10]. At cryogenic temperatures, they possess a surprisingly long lifetime[6] ( $\sim 1\mu\text{s}$ ) that arises from the electron-hole ( $e^-/h^+$ ) exchange splitting of the exciton, giving rise to a dipole-forbidden transition called the dark exciton[28] and a dipole-allowed transition called the bright exciton[22]. Relaxation into, and emission from, the lower energy dark exciton produces the  $\mu\text{s}$ -long lifetimes observed at these temperatures. At higher temperatures wherein the Boltzmann

energy ( $k_B T$ ) is greater than the  $e^-/h^+$  exchange energy, thermalization results in population of the bright exciton state[9, 33]. Empirically, there is no drastic changes in the lifetimes[9] when  $T > 100K$ , so lifetime studies done at room temperature can be considered to fall within a high-temperature, bright exciton populated regime. This bright exciton state is expected to be the primary contributor to the room-temperature (RT) PL. However, inspection of the RT-PL reveals that mono-exponential kinetics are not obtained in monodisperse samples[34, 32, 10, 31] and that a size distribution argument of 5% still cannot account for the observed non-exponentiality in ensemble measurements.

Single-dot[35, 36, 37] time-resolved spectroscopic studies[10, 38] in this high-temperature regime corroborate these findings and have revealed that the PL lifetime is strongly correlated to the PL intermittency, such that mono-exponential decays can be obtained for dots which are *on* more often, and non-exponential decays are obtained for dots which are *off* more often. Therefore each dot within an ensemble measurement will have its own characteristic lifetime decay[10], and more importantly each decay event will have its own individual lifetime[38]. These studies highlight the role of Auger photoionization (API) in the excited state behavior[10] which is the origin of the intermittency[39, 27, 40], and is a strong contributor to the lifetime decay. Since API results in carriers trapping outside of the QD at lower energy trap centers, such as those found in surface states[41], this implies that surface quality plays a dominant role in the PL lifetime characteristics. In essence, the excited state is coupled to a distribution of trap states, which will cause a strong distortion in its lifetime behavior. It follows that a distribution of trap centers

results in a distribution of trapping rates for the charge carriers, and ultimately a distribution in the observed lifetime decays[10, 42].

The currently accepted model for the PL lifetime decay in CdSe QDs is a 3-state model that characterizes the non-exponential lifetime as a *single, strongly distributed lifetime decay* arising from the recombination of the electron and hole at the semiconductor band-edge, often referred to as the band-edge exciton (BEE) returning the system to its crystal ground state (CGS). In the 3-state model, carrier trapping events produce a distributed charged dot state (CS) that is assumed to be non-emissive[39], inducing distributed non-exponential decay behavior by coupling to the emissive BEE state. The intrinsic radiative and non-radiative rate constants of the BEE are assumed to be unaffected by carrier traps. However, extrinsic nonradiative trapping rates shorten the observed lifetime. Because the charge carrier has the opportunity to trap at a variety of different sites, the ensemble result is that a distribution of mono-exponential decays are observed, corresponding to each specific trapping event with a different lifetime. The averaging of these lifetime decays produces a non-exponential decay. The extraction of this distribution can be performed using several different methods, the simplest being an inverse Laplace transformation[10]. The peak of the lifetime distribution is related to the intrinsic radiative and non-radiative rates while the width of the distribution is related to the number of carrier traps present, which are known to fluctuate depending on the local environment. Therefore this 3-state model consists of two discrete states (BEE and CGS) and one distributed state involving a charge trapping event wherein the QD core is charge imbalanced, called the charged dot state (CS).

An alternative 4-state model exists, which incorporates an emissive charged excitonic state[43, 32, 44]. This model encompasses the 3-state model elements but continues with events that occur while the dot is charged. If the time that the carrier spends in the trap is relatively long, or if the radiation density is high enough, a second absorption of a photon can occur[45] from the CS[32], thus forming a charged exciton (CE). This entity is a doubly excited particle wherein an exciton is formed in the CdSe core and is influenced by the Stark field generated by the trapped charge (on the surface) and its opposite partner (which remains in the core) as well as Coulomb correlation effects[46]. This CE state has been observed and is shown to distort the spectral profile of ensemble QD measurements[32]. Laser power and surface quality are the primary factors that determine the influence of the CE[44]. This CE state is emissive[32] and can obstruct measurement of the single-photon lifetimes considerably by complicating the lifetime decay traces.

Of greater interest to the field is the development of a self-consistent model to explain the enhanced quantum efficiency observed upon the addition of a thick ZnS shell to the surface of a CdSe core[47]. These core-shell structures exhibit increased quantum efficiency that has been ascribed to removal of surface trap centers, which should lead to distributed but nearly mono-exponential decay kinetics arising from the decay of the exciton at the band-edge. Developing a self-consistent model to describe the decay kinetics for core and core-shell QDs is critical for developing a full understanding of the importance of trapping to explain the wildly variant quantum efficiencies and lifetimes in these materials.

It is desirable, then, to seek a method in which these decays can be analyzed without the prior assumption of a kinetic model, as this will be the most rigorous and unbiased approach. In this way, the kinetic model is not a parameter added to obtain the lifetime, but in fact *is* the solution of the lifetime data. While simple inverse Laplace transformations have been used to extract this data[10], they are prone to instrumental artifacts[48] such as baseline distortion and so a more rigorous method that can be applied to all CdSe QD lifetimes is needed.

In this chapter, we show how transient PL data can be analyzed with a powerful fitting method, called the Maximum Entropy Method (MEM), that ultimately allows unambiguous assignment of two distinct excitonic states in CdSe QDs at room temperature. MEM-NLS can provide a detailed picture of the excited state decay processes in materials that have multiple decay processes complicated by a distribution arising from size, shape and trap densities. The analytical power of MEM lies in its *a priori* determination of lifetime distributions through the use of the most conservative estimate.

We first describe our method of acquiring the transient PL, then describe the problem of examining complex kinetic behavior, followed by a short discussion of the solution to this problem offered by the MEM method. We then examine the resulting lifetime distributions from our MEM analysis for CdSe and CdSe/ZnS QDs, wherein we are able to explain our observations in the context of a 4-state model. We find that the addition of an inorganic capping layer to CdSe QDs primarily results in the enhancement of Auger nonradiative processes that quench the charged exciton PL. Finally, our correlations to

single-dot lifetime studies in the literature reveals that the inclusion of photo-induced charging within the excited state behavior provides a complete model for explaining CdSe QD lifetimes in a room-temperature, solvent-dispersed environment.

## 3.2 Experiment and Analysis

### 3.2.1 Sample Preparation, Instrumentation and Analysis Software

CdSe quantum dots were prepared by colloidal techniques[4]. In some cases they were overcoated with a layer of ZnS [34, 49]. The QDs used in this study consisted of two preparations of CdSe, with radii ( $a$ ) of  $22\text{\AA}$ , one of which was further overcoated with a ZnS shell consisting of 3.8 monolayers, estimated from precursor ratios.

Time-resolved spectra were gathered on CdSe QDs dissolved in toluene by 10ps duration pulses at 320 nm (3.875 eV) at a 1 MHz repetition rate obtained by frequency-doubling the output of a synchronously-pumped, cavity-dumped R6G dye laser. Final spot size at the focal point was  $50\mu\text{m}$ . After dispersion of the emitted light through a 1/4-m Chromex monochromator, detection was achieved with a Hamamatsu streak scope. In Fig. 3.1 we show a typical streak image taken of one of our samples, a CdSe QD dispersed in toluene. As can be seen, use of a streak camera as a detection method allows for the collection and analysis of not only the time-resolved decays, but the transient PL. Lifetimes

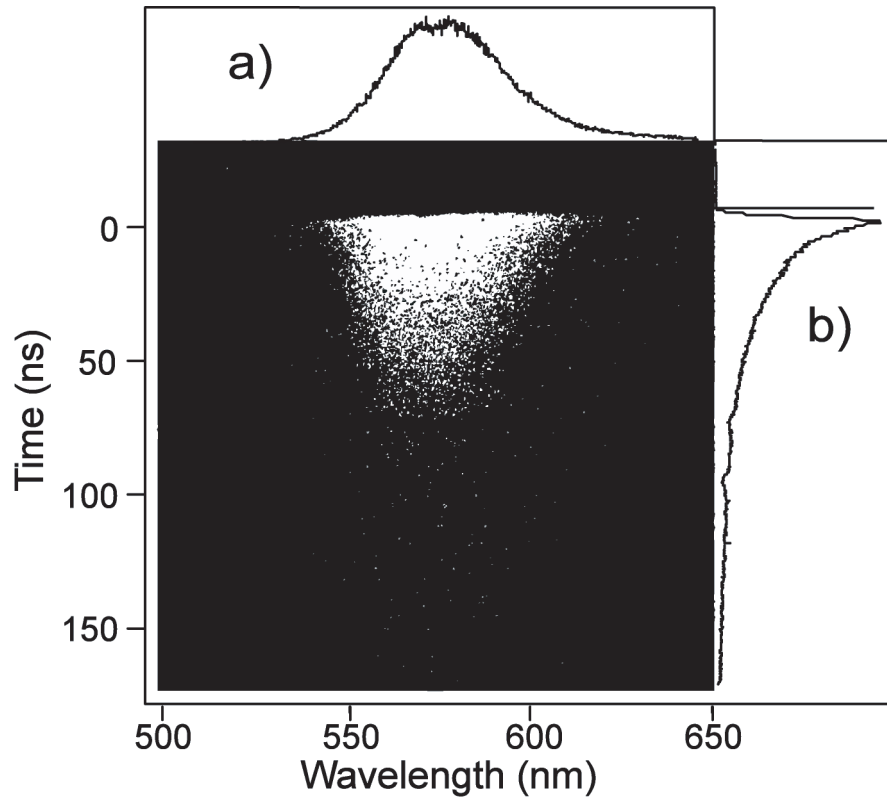


Figure 3.1. Streak image taken of a CdSe QD( $a=22\text{\AA}$ ) where cw-PL spectra can be taken by binning pixels vertically (a) or Time-resolved decays can be taken by binning pixels horizontally (b). The excitation pulse is also shown in (b)

were extracted by binning the pixels vertically (Fig. 3.1b) across the desired wavelength range while transient PL spectra are obtained by binning the pixels horizontally (Fig. 3.1a).

All MEM-NLS fits were performed with MemExp v2.0, developed by P.J. Steinbach[50, 51], using realistic parameters for this particular data set. In particular, rising distributions (negative exponentials) were neglected in this data set. Extrapolated processes were also eliminated such as those that occur at times comparable to the excitation pulse ( $\sim 10\text{ps}$ ) or larger than the empirical



time window ( $\sim 200$ ns). Traditional nonlinear least squares fitting was performed with *Mathematica 4.2*. Transient PL data was analyzed by fitting the PL to single Gaussian functions,  $[I(E_0)e^{-(E-E_0)^2/\Delta E}]$ , which allowed facile extraction of the peak characteristics such as height( $I(E_0)$ ), position( $E_0$ ), and width( $\Delta E$ ).

### 3.2.2 The Problem of Assessing Lifetime Distributions

Complicated decay processes can make choosing the appropriate kinetic model based solely on inspection of the raw data very misleading. As an example, we show in Fig. 3.2 how lifetime data for CdSe( $a=22\text{\AA}$ ) in toluene at room temperature can be fit to 3 distinct lifetime functions. The two most popular models to which CdSe lifetime data are fit are shown, namely a discrete dual decay model and a distributed decay model.

The bi-exponential decay( $D_{Bi}(t)$ ) consists of the fractional contribution ( $x \in 0 \leq x \leq 1$ ) of two lifetimes ( $\tau_1, \tau_2$ ),

$$D_{Bi}(t) = xe^{-t/\tau_1} + (1 - x)e^{-t/\tau_2} \quad (3.1)$$

The stretched exponential decay consists of the William-Watts lifetime ( $\tau_{WW}$ ) and the stretching parameter ( $\beta$ ),

$$D_{WW}(t) = e^{-(t/\tau_{WW})^\beta} \quad (3.2)$$

However, as can be seen in Fig. 3.2, both the bi-exponential fit (dual de-

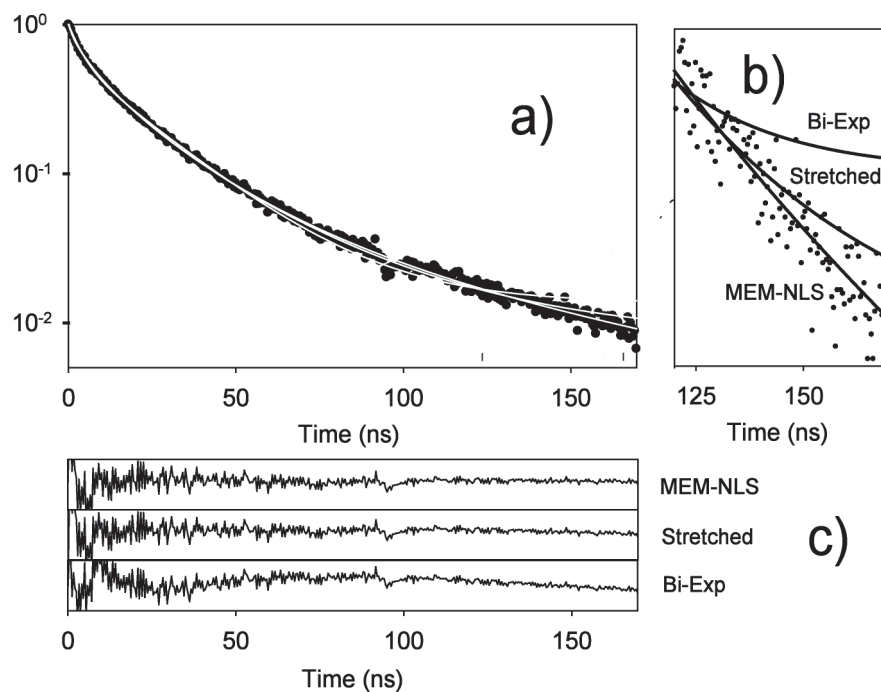


Figure 3.2. Comparison of 3 different fitting techniques for PL lifetime data for CdSe( $a=22\text{\AA}$ )-TOP(O) dissolved in toluene. a) PL decay traces are fit to a bi-exponential, a stretched exponential ( $\beta=0.67$ ) and a distribution function given by the MEM-NLS algorithm. b) An expanded view of the tail of the decay trace in shown in a). c) the residuals for the fits given in a).

cay model), and the stretched exponential fit (distributed decay model) deviate significantly from the data set in the tail region, which is a critical region in assessing fit quality. This suggests that these distributions alone do not accurately reflect the obviously complicated decay kinetics, and consequently do not reflect the underlying physics that influences the decays. Formally the discrete nature of the biexponential process follows the sum of two Dirac delta functions when written in terms of its distribution,

$$f_{Bi}(\tau, x, \tau_1, \tau_2) = x\delta(\tau - \tau_1) + (1 - x)\delta(\tau - \tau_2) \quad (3.3)$$

such that the distribution is infinitely thin and defined only at  $\tau_1$  and  $\tau_2$ . The stretched exponential, also called a William-Watts exponential, is described by a slightly more complicated expression[52]:

$$f_{WW}(\tau', \beta) = \left(\frac{-1}{\pi}\right) \tau' \sum_{k=0}^{\infty} \frac{(-1)^k}{k!} \sin(\pi\beta k) \frac{\Gamma(\beta k + 1)}{\tau'^{\beta k + 1}} \quad (3.4)$$

where  $\tau' = \tau_{WW} / \tau$ . This lifetime distribution function can be evaluated with differing stretching parameter values ( $\beta$ ), as shown in Fig. 3.3. A higher  $\beta$  value corresponds to a tighter distribution which has a more discrete appearance, while a lower  $\beta$  value corresponds to a wider distribution. In addition, the peak of the distribution deviates more strongly (toward longer lifetimes) from the extracted  $\tau_{WW}$  as  $\beta$  decreases and eventually approaches a truly random distribution ( $\beta \rightarrow 0$ ). Whereas discrete exponentials such as the biexponential represent state-to-state transitions with well-defined, quantized energies, distributed kinetics reflect systems with closely spaced continuum-like

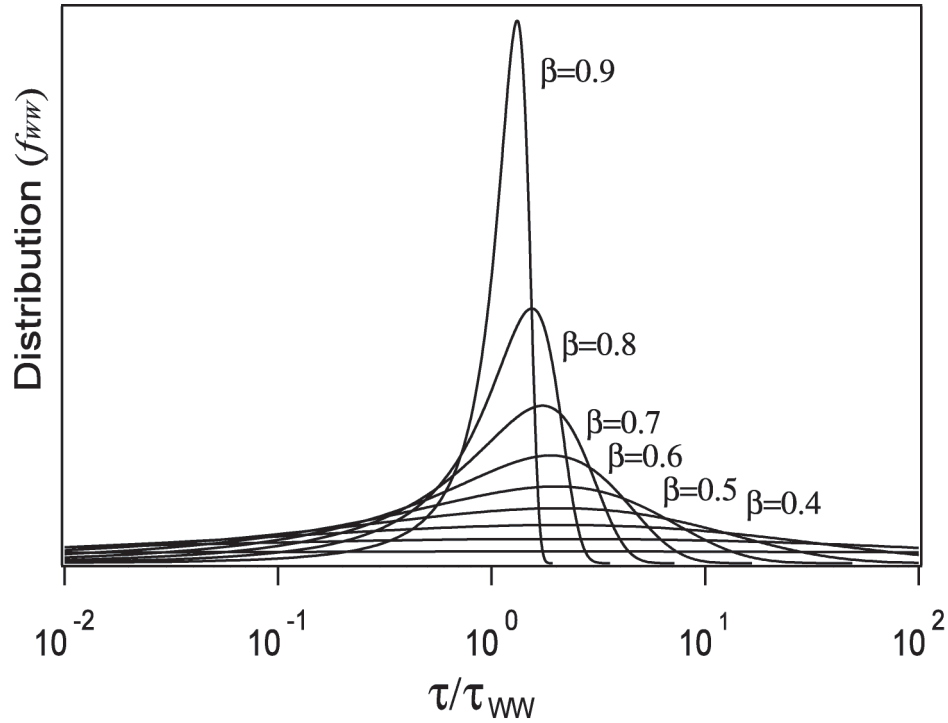


Figure 3.3. The William-Watts distribution function ( $f_{WW}(\tau, \beta)$ ), evaluated at different values of the stretching parameter ( $\beta$ )

energy levels wherein there is a dominant transition process coupled to a continuum of states. As the stretching parameter approaches its maximum value, ( $\beta \rightarrow 1$ ) it can be inferred through the Fermi Golden Rule[21], that the system transitions from continuum-like energy level spacing to discrete-like energy level spacings. The procurement of accurate lifetime distributions therefore strongly impacts our understanding of the energy level structure in CdSe QDs.

The discrete and distributed fits to CdSe QD lifetimes that have been used (Eq. 3.1 and Eq. 3.3) represent only the limiting cases of the true lifetime distribution ( $f(\tau)$ ), which is convoluted with its own time-dependent decay ( $e^{-t/\tau}$ ). In principle, this relationship can be written simply as a convolution integral in the time domain as

$$D(t) = \int_0^{\infty} f(\tau)e^{-t/\tau} d\tau \quad (3.5)$$

Therefore it is mathematically possible to arrive at  $(f(\tau))$  through deconvolution of this integral[53]. Such an approach would allow the extraction of the true lifetime distribution prior to the simplification that leads to Eq. 3.1 and Eq. 3.2. When examining very complicated kinetics, Eq. 3.1 and Eq. 3.2 fail to accurately reflect phenomena such as *both* distributed and discrete processes that compete with one another.

### 3.2.3 The Solution Offered by the Maximum Entropy Method

When performing mathematical transformations on data, families of related solutions are generated[53, 54] that are inherently influenced by variables such as systematic noise. The presence of systematic artifacts can significantly reduce the apparent resolution and data quality, obscuring the underlying processes being investigated. The development of mathematical algorithms to deal with this inherent complication between data collection and its subsequent data analysis has led to several different noise-filtering techniques. MEM is one such technique that has found wide application in many diverse fields, ranging from telescopic image filtering in astronomy[55] and deconvolution of complicated enzyme kinetics in biophysics[56, 51]. Despite its current wide applicability, MEM has entered into the realm of basic exponential analysis only as recently[57, 53] as 1999, and as of this writing, less than 400 articles utilize this method in their data analysis, only 15% of which deal with the analysis of

kinetic data. An even smaller fraction of this 15% use MEM to analyze fluorescence decay data. The majority of the articles composing this 15% have been released only in the past few years. The use MEM has therefore been spreading rapidly in the field of analysis of lifetime data, and to the authors' knowledge, this article represents the first account of its application to any nanoscale system.

The core principle of MEM is that in a system of many variables, some of those variables will be strongly dependent on the behavior of others, such as systematic experimental errors. As such, one can find strong correlation between such parameters and this influences the overall entropy of the solution that incorporates those variables. In this case, entropy, refer to the lack of intrinsic patterns and order found in a multi-variable system wherein some variables may be nonlinearly correlated to each other. These correlated variables may represent undesirable artifacts in the data set, like systematic errors, and may be eliminated by examining the entropy of the solution. It follows that if one were to find the solution with the maximum entropy, and thus the solution with the least amount of systematic noise, one would arrive at a solution that more accurately reflects the underlying physical mechanisms being studied.

We apply a rigorous fitting method to CdSe QD lifetime decay data that allows for the domain transformation of time ( $t$ ) decay traces into lifetime( $\tau$ ) distributions. The MEM[50, 51] is utilized to extract a physically meaningful model to describe excited state decay processes observed in CdSe QDs and allows for a complete, model-free analysis of the lifetime decay characteristics.

Exclusive use of pure Nonlinear Least Squares (NLS) fitting algorithms, such as *Levenberg-Marquadt*[48], in examining excited state lifetimes requires the assumption of a model, where both discrete and distributed kinetics have been previously assumed to fit the data. A MEM fit to lifetime data does not require a model, but in fact *suggests* the model.

In an approach similar to Eq. 3.5, the logarithmic distribution of lifetimes,  $f(\log \tau)$ , can be determined by fitting empirical decay trace, to the convolution function,

$$D(t) = \int_{-\infty}^{\infty} f(\log \tau) e^{-t/\tau} d \log \tau \quad (3.6)$$

The reliance on numerical matrix-inversion to perform this routine necessarily generates a large set of satisfactory inverse matrices with no explicit criterion for selection. MEM analysis produces the maximally noncommittal matrix, or the solution that produces the least correlation between parameters, which in principle represents the most conservative guess. However, the MEM fit quality is often poor and artifact ridden[51, 53], therefore a robust bootstrapped hybrid MEM-NLS (Maximum Entropy Method/Nonlinear Least Squares) routine using Newton-Raphson optimization is employed[50, 51]. MEM-NLS relies on the maximization of a quality parameter ( $Q$ ), which is determined by a weighted linear combination of the entropy ( $S$ ) of the data and the normalized sum of the squares of the residuals ( $\chi^2$ ),

$$Q \equiv S - \lambda \chi^2 \quad (3.7)$$

where  $\lambda$  is a balancing factor. As can be seen,  $Q$  is maximized when  $S$  is maximized and  $\chi$  is minimized. Therefore this hybrid method seeks the solution with the minimum scalar deviation from the data (given by NLS) and the maximally uncorrelated vector deviation (given by MEM). The entropy of the data is related to the true distribution function of the data set ( $f_j$ ) and the iteratively better prior data fits ( $F_j$ ) summed over the index  $j$ .

$$S \sim \sum_j f_j - F_j - f_j \ln \left( \frac{f_j}{F_j} \right) \quad (3.8)$$

The entropy is maximized when its derivative approaches zero ( $\frac{dS}{df} \rightarrow 0$ ), and as a result the fitted prior distribution approaches the true distribution, ( $F \rightarrow f_j$ ).

## 3.3 Results

### 3.3.1 CdSe Quantum Dots: Bare Core

In Fig. 3.2 and Fig. 3.4 we show the fit to a stretched exponential[52](Eq. 3.2), producing  $\tau = 11.8ns$  and  $\beta = 0.67$ . A bi-exponential fit (Eq. 3.1), is also shown, with  $\tau_1 = 4.0ns$ ,  $\tau_2 = 24.0ns$  and  $x = 0.43$ . For comparison, the MEM-NLS determined fit of the data set is also shown, which produces two identifiable peaks in the lifetime distribution shown in Fig. 3.4 with  $\tau_1 = 2.7ns$ ,  $\tau_2 = 19.2ns$ , with the fractional peak area for the short lifetime,  $x = 0.29$ .

As can be seen from the fit quality and the residuals in Fig. 3.2a and 3.2b,



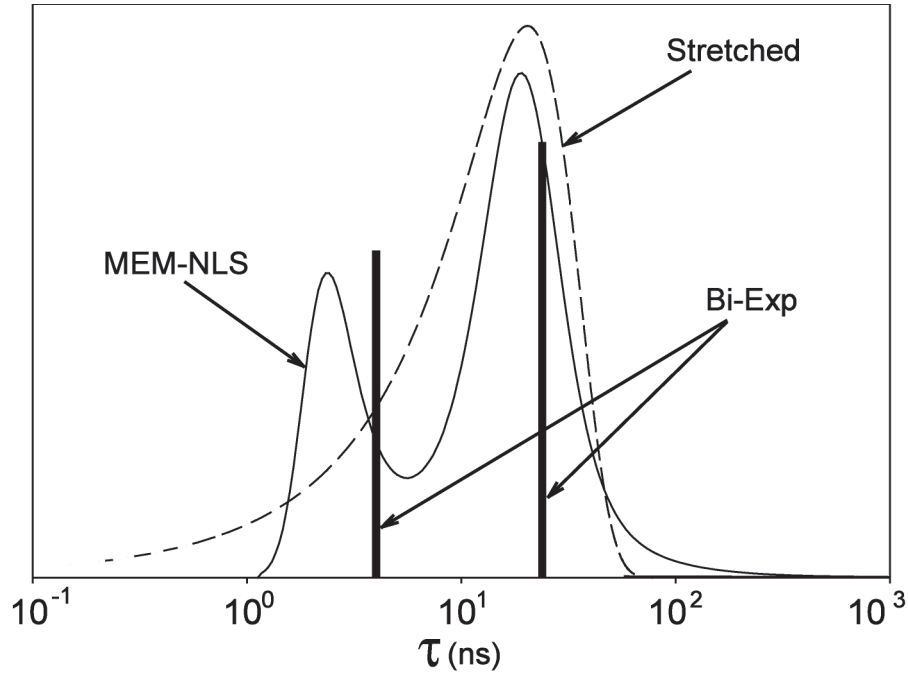


Figure 3.4. A comparison of the 3 distributions used in Fig. 3.2 for CdSe ( $a = 22\text{\AA}$ ) taken at all PL energies observed. The biexponential distribution ( $f_{Bi}(\tau)$ ) is shown as the black bars, the stretched distribution ( $f_{WW}(\tau)$ ) is shown as the dashed line and the MEM-NLS distribution is shown by the solid line.

there is little discernible difference in the time domain using these fitting routines, although at longer times there is a divergence of both the bi-exponential and stretched exponential fits from the data points, while the MEM-NLS fit follows the data set at longer times more faithfully, as seen in Fig. 3.2c This fidelity is made possible by adjustment of the lifetime distribution appropriately, an option not available for the other two predefined distributions. In Fig. 3.4, the three methods are compared in the lifetime domain, where we can clearly see that the MEM-NLS fit has extracted two distinct, but distributed lifetimes.

Surprisingly, there is good agreement in terms of lifetime positions and relative height between the bi-exponential discrete kinetics and the MEM-NLS

distribution. It is also clear that the stretched exponential fit reproduces the position of the dominant long-timescale process, but fails at the actual lifetime distribution since it is unable to account for the short-timescale process that is clearly evident from the MEM-NLS distribution. In addition the value of the stretching term obtained,  $\beta=0.67$ , is inconsistent with what a 5% size distribution should yield,  $\beta \sim 0.95$ . This observation is reflected in Fig. 3.2c where both MEM-NLS and the stretched exponential have similar residuals, with the only variance being lower residual fluctuations at shorter time periods for MEM-NLS, which is consistent with MEM-NLS sensing a second, short timescale process and adjusting the distribution correspondingly.

Further support for a dual emissive state model is found in the spectrally-resolved temporal decays, as shown in Fig. 3.5 where the decay is sampled at different spectral regions of the observed PL which shows only two processes in the decay, whose contributions are wavelength-dependent.

The spectrally integrated lifetime distributions shown in Fig. 3.5b, reveal two distinct lifetime populations, whose relative populations are strongly dependent on the observation window. In fact, at lower energies, the long lifetime BEE component contributes more than the short lifetime CE component. Therefore, the decay traces shown in Fig. 3.5a result almost purely from the spectral dependence of the relative contribution to the intensity of these two states. When combined with the transient PL shift, this provides unambiguous evidence of a 4-state model for the excited state decay processes in CdSe where two states with nearly the same energy but drastically different lifetimes exist in CdSe QDs, rather than a distribution of single excited states as suggested by

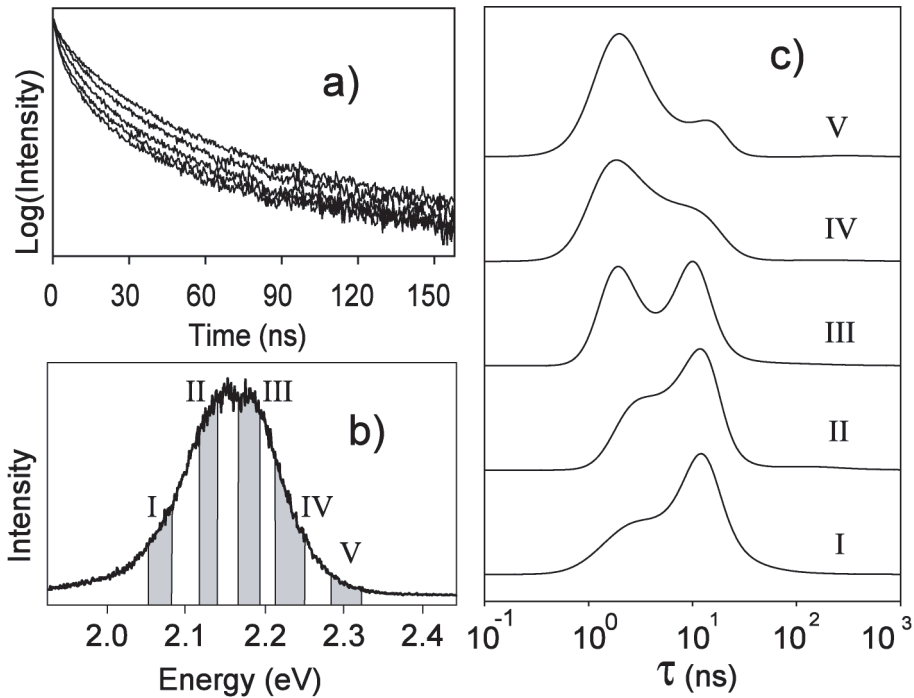


Figure 3.5. Transient PL data for CdSe( $a=22 \text{ \AA}$ ) analyzed in terms of PL energies centered at I(2.07eV), II(2.12eV), III(2.18eV), IV(2.23eV), V(2.30eV). a) shows the normalized decay traces for these energies. b) shows the time-averaged PL, where the shaded areas show the regions being probed in this figure. c) shows the MEM-NLS fits for I,II,III,IV and V.

the 3-state model.

### 3.3.2 CdSe/ZnS Quantum Dots: Core-Shell

The quantum efficiency of core-shell CdSe/ZnS dots is known to increase by as much as a factor of 3 after addition of the ZnS shell[47]. It has long been speculated that the increase in quantum efficiency arises from changes in trap population. Therefore one predicts that the CE will be eliminated with ZnS passivation due to trap removal, providing a fundamental model to explain the observed enhancement in quantum efficiency. In the ZnS-capped CdSe, the

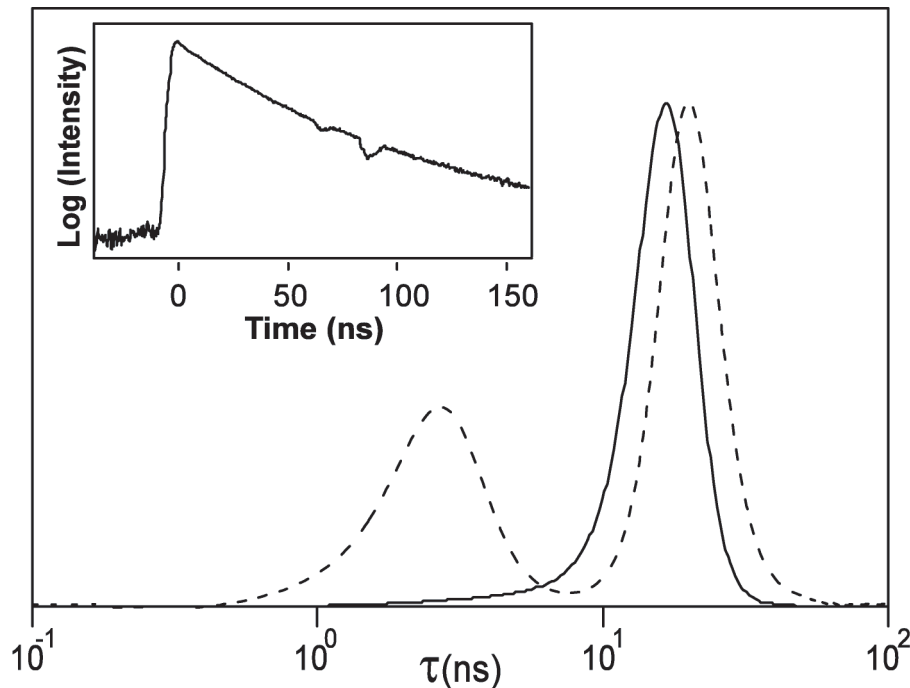


Figure 3.6. The MEM-NLS distribution function for CdSe QD ( $a=22 \text{ \AA}$ ) (dotted line) and after it was capped with a ZnS layer (solid line). Inset: CdSe/ZnS QD ( $a=22 \text{ \AA}$ ) lifetime decay trace. The 2 sharp drops in intensity at 60ns and 80ns observed are artifacts originating from damaged channels in the MCP

ZnS shell has a dramatic effect both on the lifetime distribution, as seen in Fig. 3.6, where we show a CdSe QD prior to and after capping with a ZnS layer. The most dramatic effect observed is the complete disappearance of the short lifetime component. There is also a slight shortening of the lifetime of the the long component after capping as can be seen in Fig. 3.6 as a shift of the peak to shorter lifetimes. As can be seen in the inset of Fig. 3.6 that with the disappearance of the short timescale process, the ensemble decay profile can be described as a single distribution associated with the BEE. This result is consistent with what is found for single-dot lifetime measurements wherein a distributed exponential decay is found in ZnS-capped CdSe[10, 38].

The PL decay can also be monitored as a function of PL energy, in a similar way as Fig. 3.5. In Fig. 3.7a we show the PL decay traces binned over 3 different PL energy ranges, as indicated in the time-averaged PL in Fig. 3.7b. Upon capping, the PL decay traces do not deviate as dramatically as a function of PL energy when compared to the bare core decay traces of Fig. 3.5a. This suggests that the PL manifold observed primarily derives from a single state decay. The MEM-NLS fits are shown in Fig. 3.7c for each of these regions, where we clearly observe a single strong dominant decay process that remains at the same lifetime throughout the energies probed. In Fig. 3.7c-III, we observe the presence of a shorter, weaker lifetime whose position and shape match the short lifetime component observed in the bare core QDs of Fig. 3.5c. This feature appears only in the higher energies of the PL manifold, analogous to the higher energy regions of the the bare core PL of Fig. 3.5c. Therefore it is very likely that the short-lived states observed in CdSe and CdSe/ZnS are in fact the same state, though it is significantly repressed in CdSe/ZnS. In fact, without transient PL the extremely weak presence of the short component could not have been identified in CdSe/ZnS, as the energy integrated scans have averaged out its contribution (Fig. 3.6) since it contributes a vanishingly small proportion to the total PL. In addition there is no shift in the peak of the lifetime distribution across different energies, exactly as would be expected if the decay profile originated from a single state. We note that a broadening of the distribution of this single lifetime state exists at lower energies, and can be explained as resulting from ensemble-averaged spectral diffusion. Since the PL energy of individual QDs change due to local fluctuations in its environment[37], it follows that the lifetime should follow an identical trend. Therefore the use of

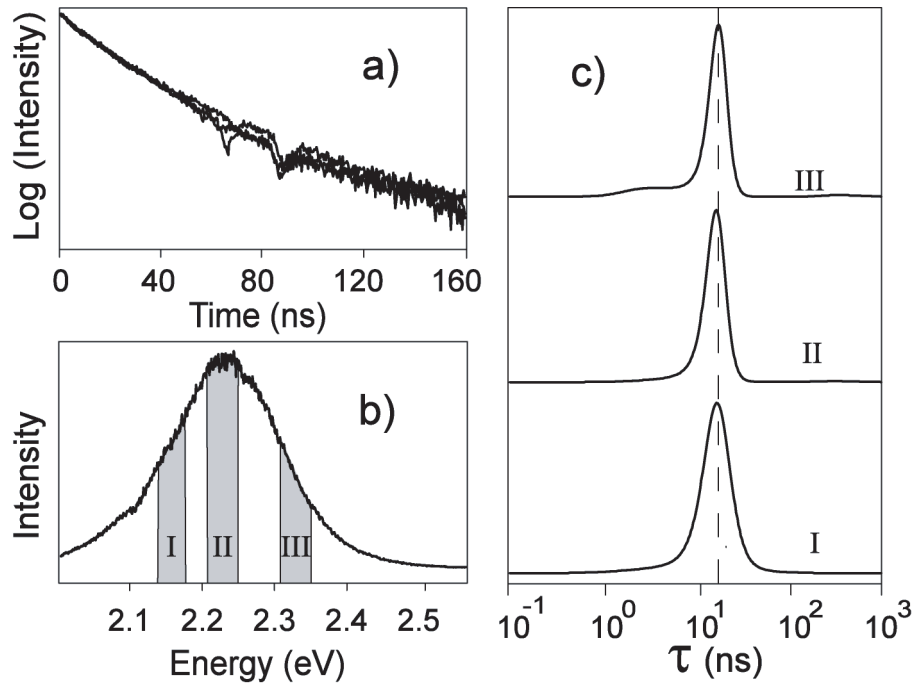


Figure 3.7. Transient PL data for CdSe/ZnS( $a=22 \text{ \AA}$ ) analyzed in terms of PL energies centered at I(2.17eV), II(2.24eV) and III(2.33eV). a) shows the normalized decay traces for these energies. b) shows the time-averaged PL, where the shaded areas show the regions being probed in this figure. c) shows the MEM-NLS fits for I,II,III and the dotted line is a guide to the eye, centered on the peak of I.

transient PL spectroscopy artificially selects the subpopulation prone to a high degree of spectral diffusion by examining this low energy PL area. These low-energy decay events possess stronger charge fluctuation, and therefore a wider distribution of lifetimes.

## 3.4 Discussion

### 3.4.1 A 4-state model

A self-consistent model can be developed based on the MEM-NLS analysis to describe the observed lifetime decays of the resultant behavior differences for core and core-shell QDs. Our results can be discussed using the framework of carrier trapping and subsequent dot-charging as being the primary factors that affect the lifetime decays. A schematic describing this model is shown in Fig. 3.8. Absorption of a resonant photon promotes the QD from its electronic crystal ground state (CGS) to its band-edge excitonic (BEE) state, forming an  $e^-/h^+$  pair within the QD. The presence of defects in surface states causes carriers to localize in these traps, thus separating the exciton. Because not all surface traps are the same, there will be both structural variance (between dots) as well as local environmental effects (between trapping events). This variance will form a distribution of trap sites in energy, and ultimately a distribution of trapping rates, resulting in the widths of the MEM-NLS distributions (or  $\beta$  in a stretched exponential analogy). Formally the distribution of states in which the charge is trapped can be called a charged dot state (CS). Because the BEE state is intimately coupled, through carrier trapping, to the strongly distributed CS state, its behavior will also take on distributed characteristics. These distributed kinetics, in fact, manifest themselves as non-Poissonian intermittency[41] and in distributed excited state lifetime decays.

However, the second phenomenon that can occur is a secondary absorption of a resonant photon by the QD[45], not necessarily during the lifetime of

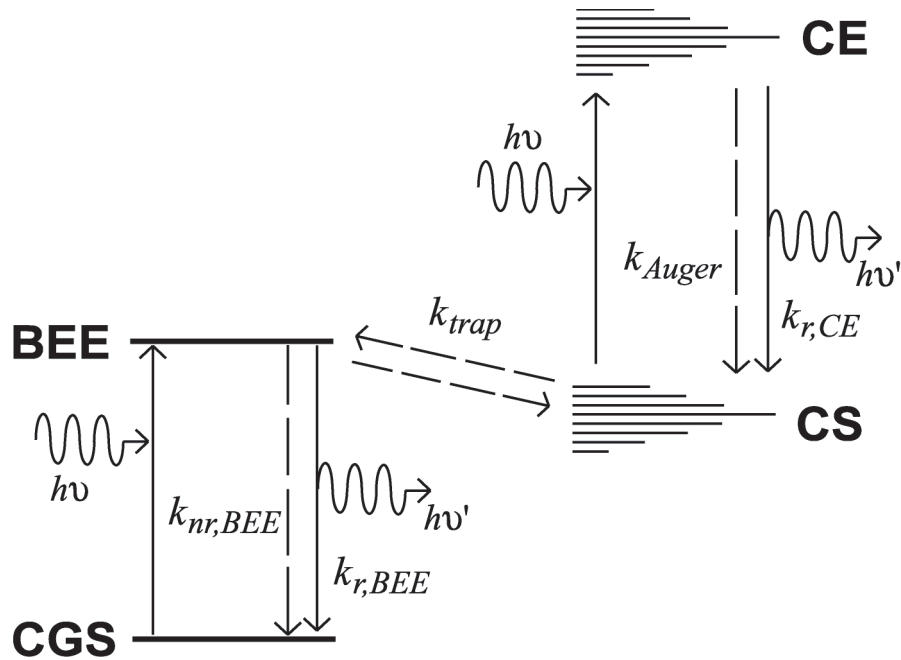


Figure 3.8. Summarized model for CdSe excited states. Shown are the Crystal Ground State (CGS), the Band Edge Exciton State (BEE), the Charged State (CS) wherein the exciton is split as a charge carrier becomes trapped outside the dot, and the Charged Exciton (CE) which forms due to secondary light absorption by the CS. Solid lines represent radiative transitions such as absorption and spontaneous emission ( $k_{r,BEE}, k_{r,CE}$ ) from each state. Dotted lines indicate possible nonradiative paths for different states and include carrier trapping ( $k_{trap}$ ), Auger-processes, ( $k_{Auger}$ ) and intrinsic BEE decays ( $k_{nr,BEE}$ ).



the BEE excited state, but during the persistence time of the trapped charge carrier, which can last for tens of seconds[45]. If this occurs, a second  $e^-/h^+$  pair forms within the QD, producing 3 carriers within the core and a trapped carrier on the outside[45]. Therefore each CS state will be discretely coupled to a path-specific CE state. The strong distribution in the CS state causes the CE state to also be strongly distributed regardless of the discrete nature of the electronic transition. This explains the similar wide distribution found in the short-lived state in Fig. 3.4 and 3.6.

Several strong factors are predicted to affect the kinetics of this 4-state system. The most important of these factors is the trapping of a charge carrier. The single-photon cycling between the CGS and BEE will be strongly affected by this trapping rate, and is the only path that gives rise to the CS and CE state. Therefore controlling the trap density as postulated for core-shell QDs is very important in tuning the kinetics of these QDs.

One possible explanation for the loss of the short component as observed in Fig. 3.6 for the core-shell materials upon capping is due to enhanced passivation of surface trapping sites, effectively inhibiting the formation of the CS state by reducing the trapping rate of the charge carriers. However, if this were the case, then one would expect that the short component would disappear and the long component's distribution would sharpen, since the width of this distribution is directly related to the distribution of trap states. Consequently, mono-exponential kinetics would be observed in the lifetime decay. In fact, this is *not* what we observe. Clearly, the long-lived component remains distributed (Fig. 3.6) and the decay remains non-exponential(Fig. 3.6 inset). Therefore an

alternative explanation is required that accounts for both the disappearance in the short-lived lifetime and the presence of a distributed long lifetime. It is likely that the CS state forms efficiently even with the capping layer present due to the imperfect lattice matching at the interface, explaining the continued width of the BEE state distribution broadening. However the lack of emission from the CE state implies that there exists strong nonradiative coupling that rapidly quenches the PL completely. This nonradiative coupling is likely to occur from Auger-like relaxation processes ( $k_{Auger}$ ), which are expected to dominate due to the multiple charges occupying the QD interior when in the CE state (Fig. 3.8). However, the deactivation of the CE state proceeds by both radiative and non-radiative means, and it is possible to induce this CE state to begin emitting again by acceleration of the radiative recombination velocity. This has already been done using metal surfaces to enhance the radiative coupling, and in fact charged PL is observed in these experiments[43]. Therefore, capping of the CdSe core with an inorganic shell does not remove trap centers, but instead induces stronger Auger relaxation of the CE state back to the CS. This can be physically accounted for when one considers the higher bandgap shell inducing stronger confinement and therefore stronger charge interaction and overlap, leading to accelerated multi-charge processes such as Auger. The shortening of the BEE lifetime coincident with an increase in the quantum yield could also mean a shortening of the radiative lifetime. Stronger spatial confinement of the exciton by the presence of the ZnS capping layer improves the overlap of the electron and hole wavefunction, resulting in a faster recombination and a shortening of the BEE lifetime. This enhanced radiative coupling could partially account for the improved quantum efficiency upon capping.

The shortening of the observed lifetime upon capping (from  $\tau=26.0$  to  $\tau=17.4$ ) is less than 35%. This change in shortening of the BEE lifetime does not account for the nearly 50% increase in the PL quantum efficiency. Therefore, the rise in quantum efficiency must come about not only through improvement of radiative recombination ( $k_{r,BEE}$ ), but hindrance of non-radiative factors in the BEE state. While changes in the intrinsic nonradiative relaxation ( $k_{nr,BEE}$ ) will occur upon capping[8], it is likely that modification of extrinsic nonradiative pathways (such as surface defects) will be most dramatically observed. Although our data suggests that the BEE remains coupled to a distribution of trap states even upon capping, it is likely that the overall number of carrier traps has been reduced, as would be expected by such a drastic change in the surface structure. Such an explanation would account for our observation of improved quantum efficiency and yet still explain the broadening in the BEE state emission. Kinetically, this is shown in Fig. 3.8 wherein  $k_{trap}$  is reduced upon addition of the ZnS shell.

### 3.4.2 Comparison to Single-Dot Studies

Our studies indicate (using MEM-NLS analysis) that these ensemble solution-phase CdSe QDs clearly reveal 3 distinct phenomena, some of which have been observed in their single-dot counterparts: i) there are two distinct lifetimes that compose the decay of the observed photoluminescence, ii) the two lifetimes are distribution-like and not purely discrete decays, iii) there is a shift to higher energies in the transient PL, iv) addition of a capping shell eliminates the short timescale component completely. The presence of two distinct but distributed

states is found unambiguously using MEM-NLS. The transient PL and the spectral dependence of the MEM-NLS distribution (Fig. 3.5) together indicate that the two distributions observed result from two emissive excited states.

MEM-NLS analysis has never been used in the study of the lifetime decays in single-dot measurements, however simple inverse Laplace transformations[10] and suggest the presence of a single but very distributed state on CdSe/ZnS QDs. This is in agreement with our findings since MEM-NLS analysis extracts a single lifetime distribution for core-shell particles (Fig. 3.6). In fact, the relative lifetimes and distributions that are obtained fall roughly in-line with those in single-dot experiments. For example, Bawendi[38] and coworkers find a  $\tau_{WW}=25.0\text{ns}$  and Mews[10] and coworkers find a  $\langle\tau\rangle=20.2\text{ns}$  for the subpopulation of brightly-emitting dots. This compares very well to our findings of  $\tau_2=20\text{ns}$ . This observation provides two points of interest: i) the lifetime decays measured in ensemble solution-phase measurements and single-dot measurements are directly correlated for core-shell CdSe/ZnS QDs and ii) because the ensemble measurement matches the fraction of bright dots very closely, this suggests that the PL characteristics are largely dominated by the long-lived BEE decay as it constitutes  $> 90\%$  of the observed PL, as found in our previous study on uncapped CdSe QDs[32]. As yet, no single-dot lifetime measurements have been done on the bare, uncapped CdSe core. The lower quantum efficiency and poor stability of bare core CdSe QDs makes them undesirable candidates for these experiments. As such there is no direct comparison in the literature, and our observation of this second short-lived lifetime decay through MEM-NLS analysis is therefore unprecedented.

In addition, the proposed 4-state model agrees with experimental data on CdSe/ZnS on a metal surface[43]. The presence of a metal surface on the QD enhances the otherwise non-emissive charged exciton state (CS) (the *off* state) to emit at  $\Delta E=10-22\text{meV}$  lower than the uncharged (BEE) state. Single-electron injection[58] into CdSe/ZnS QWs produces charged exciton emission at  $\Delta E=8-12\text{meV}$ . This agrees very well with our observation of a shift to the blue in our ensemble PL measurements of CdSe where  $\Delta E=9\text{meV}$ . This blue shift is explained as resulting from the competing emissions from the redder shorter-lived CE state PL and the bluer long-lived BEE state PL. Combining our observations with those from these surface-enhanced studies we see that the capping layer suppresses the short-lived lifetime while the presence of a strong oscillating field reverses this process by enhancing the radiative rate. Therefore the results of these single-dot experiments are in agreement with the MEM-NLS ensemble treatment.

Recent observations of totally nonemissive QDs[59] within an ensemble have been shown to affect ensemble PL quantum efficiencies[60]. However, even from the emissive dots observed, there exists an intrinsic quantum efficiency that is consequently reflected in the lifetime. The nonemissive dots are not expected to contribute to the observed PL characteristics, and therefore the ensemble lifetimes measured come directly from the emissive QDs.

## 3.5 Chapter Summary

In summary, we have applied MEM-NLS to transient PL spectroscopy to resolve several important features in CdSe QD photophysics and to provide an example of how a rigorous approach to the PL lifetime data can be used to confirm the existence of dual emissive state behavior. We report the first unambiguous observation of this second PL lifetime which exists only in uncapped CdSe QDs. The addition of the capping shell eliminates this second lifetime. Our ensemble data compares very well to single-dot lifetime data, and using those studies as a basis for explaining our observations, we come to several conclusions regarding the effect of the capping shell and the identity of the observed lifetimes. The long-lived lifetime component from our studies clearly matches ( $<10\%$  error) the lifetime observed in single-dot experiments, allowing us to identify this state as the BEE state. Since no lifetimes studies have been performed on the uncapped variety in single-dot experiments, we report the first observation of this second, short-lived component. Weak PL is observed from this state due to its short lifetime and low quantum efficiency. Although it can be eliminated by a capping shell by increasing Auger processes (our results) it can also be re-activated in this form (Bawendi and coworkers[43]) by radiative rate enhancement from a metallic surface. Consistent with this body of literature, we can identify this short-lived state formally as a charged exciton state, in analogy to observations in both QD and QW excited state processes described previously in the literature.

We are currently undertaking a full characterization of CdSe and CdSe/ZnS QDs using MEM-NLS at varying sizes, capping layer thicknesses, tempera-

tures and applied photo-excitation power in an effort to investigate the trends in the charging of the exciton state and its relaxation processes.

# Chapter 4

## Photoluminescence Activation and Intermittency

Reprinted from *Chemical Physics Letters*, 391, A. Javier, G.F. Strouse, “Activated and Intermittent Photoluminescence in Thin CdSe Quantum Dot Films”, 391, Copyright (2004), with permission from Elsevier.

### 4.1 Introduction

Photo-activated photoluminescence in CdSe quantum dots [28] (QD) has received significant interest by material scientists [61, 31, 62, 63, 64]. The mechanism for this process can be explained by a light and gas mediated equilibrium between a band-edge exciton (BEE) and a charged state (CS) controlling carrier trapping and de-trapping at the dot surface. The power-dependent change in the kinetics of photo-induced brightening and darkening in thin QD



films is revealed to arise from the complementary nature of these processes. In addition, statistically significant fluctuations [41] accompany the photoluminescence(PL) as intermittent drops in intensity, which leads to the postulate that these are discrete blinking [37, 36] events. The blinking is found to be strongly correlated to the ensemble PL behavior, highlighting the importance of Auger processes on ensemble QD PL properties on the order of hundreds seconds.

## 4.2 Experimental Details

Thin films (*ca.* <100nm thick) of lyothermally-prepared CdSe QDs [4] (radius $\sim$ 25Å) were prepared by single-drop spin casting onto sapphire optical flats, and warmed to remove excess solvent. Ar<sup>+</sup> ( $\lambda_{exc}$ =488.0nm, 0.01-2mW) cw-laser-induced PL was collected (laser spot size $\sim$ 15 $\mu$ m) using front-face geometry and subsequently dispersed, after laser light rejection with a holographic notch filter, onto a 1/2-m monochromater using a CCD for detection. The PL was then collected (in air, at room temperature) using 10ms exposure times at 5s intervals with 1000 spectral acquisitions per run. All film PL spectra fit well to a gaussian function,  $I(E)/I(E_0)=exp[-(E-E_0)^2/\Delta E]$ , reflecting the dominance of the size distribution over the homogenous linewidth, allowing facile extraction of PL peak height,  $I(E_0)$ , spectral position,  $E_0$ , and spectral width  $\Delta E$ .

## 4.3 Power-dependence of Carrier Processes

### 4.3.1 Internal Nonradiative Quenching

Rapid charge carrier trapping at surface sites can follow photo-excitation, leaving the oppositely charged carrier in the dot core, thereby producing a charged state. Subsequent exciton formation within this dot produces a charged exciton (CE), whose emission is Stark-shifted [13] (toward lower energy) from the BEE. Nonradiative decay through three-bodied Auger processes at the dot core induce poor quantum efficiency [45] and short lifetimes [10, 32] for the CE. At equilibrium, the BEE and CS populations are mediated by the influx of continuous excitation radiation [36] through steady generation of charge carriers. The persistence time of the CS can be lengthened through electron-hole energy transfer to the surface trapped carrier via an Auger recombination, inducing the dot to remain darker longer and increasing the frequency of intermittency [65]. Therefore, excitation power plays a key role, through carrier generation [66], in stabilizing CS populations. The ensemble result is that there is a build-up of the darker CS dots, producing an overall darkening effect as the BEE population is depleted to increase the CS population. Fluorescence intermittency [65] and spectral diffusion [37] can be regarded as statistical sampling of the equilibrium populations of the BEE, CE and CS states at the single dot level.

### **4.3.2 Photobrightening**

Since the charging of a QD and the lengthening of the CS persistence time is excitation power-dependent, it is expected that a correlation can be found between PL intermittency (carrier trapping) and photo-activation (trapped carrier release). One such activation mechanism involves the interaction of the surface charge with ambient gas adsorbates [67], particularly Lewis electron donors [68, 69] inducing recombination by pushing the surface trapped electron back into the core to recombine with its opposite partner (brightening). Thus, the gas, through Langmuir isotherm physisorption [70] activates an otherwise inhibited PL to increase the observed photon flux. However, reactive gas adsorbates also induce permanent photochemical surface degradation [61, 71], leading to an overall PL quenching. The time-monitored photoluminescence PL will strongly reflect kinetics that increase and decrease the observed PL.

## **4.4 Charge Carrier Kinetics**

### **4.4.1 Curve Fitting Procedure**

The solution-phase (n-hexane) extinction spectrum and a representative film PL immediately after light exposure are shown in the inset of Fig. 4.1. As seen in Fig. 4.1, there is an increase in the PL intensity (brightening) which is followed by a subsequent decrease (darkening) at longer times. This behavior has been observed reproducibly [61] and varies between different sample preparations. Globally, the kinetics can be described as a series of competi-

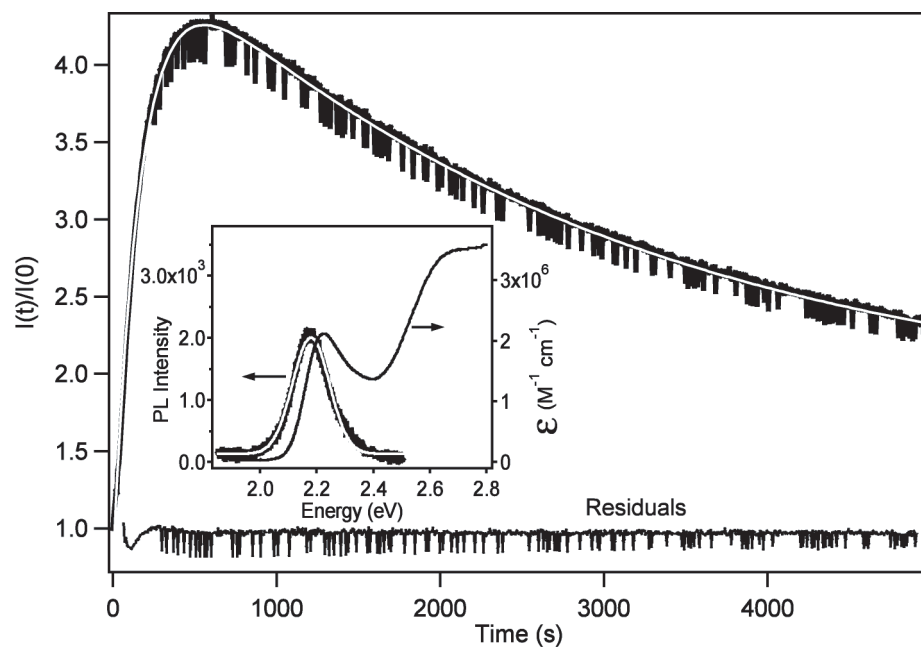


Figure 4.1. Normalized peak intensity of CdSe( $a \sim 25\text{\AA}$ ) thin film PL under exposure to laser light ( $\lambda_{exc}=488.0\text{nm}$ ) and air at room temperature. White dotted line represents a multi-exponential fit with residuals fit shown at the bottom. Inset: Thin film PL and solution-phase extinction spectrum. White line represents a gaussian fit.

tive first order processes that result in the experimental observation of a net increase and decrease in the PL intensity with time under continuous illumination,  $d[QD^*]/dt = [QD^*]/\tau$ , where  $[QD^*]$  represents the fraction of emitting QDs in the ensemble. To fit the complex kinetics in an assumption-free manner, sums of exponentials were used as trial functions for the differential rate equation and involve two PL brightening processes ( $I_\infty (1 - \exp[-t/\tau_b])$ ) and one PL decay process ( $I_0 \exp[-t/\tau_d]$ ), allowing for the extraction of the darkening ( $\tau_d$ ) and brightening ( $\tau_b$ ) time constants for each run. The residuals for this fitting procedure for one of the acquisition runs are given at the bottom of Fig. 4.1, wherein there is only a very small systematic pattern present, accompanied by sharp (single point) intensity fluctuations discussed later as being due to the darkening of a single dot or set of dots within the ensemble.

#### 4.4.2 Power-dependence for a Single Size

The PL intensity response of the film is shown for six different power densities in Fig. 4.2A, where we see a strong power dependence of the two different brightening rates and the darkening rate. At the lowest power density used, 5 W/cm<sup>2</sup> (I), only a darkening is observed. As the power is increased to 13 W/cm<sup>2</sup> (II), there is an increased darkening as seen from the change in the slope of the trace at early times, and the appearance of brightening, on-setting at  $t \sim 4000$ s. A second brightening process is distinctly observable at earlier times for powers between 28-114 W/cm<sup>2</sup> (III, IV) which is the main contributor to the previously observed PL brightening increase in CdSe thin films [61]. At 160 W/cm<sup>2</sup> (V), darkening is no longer observable, and bright-

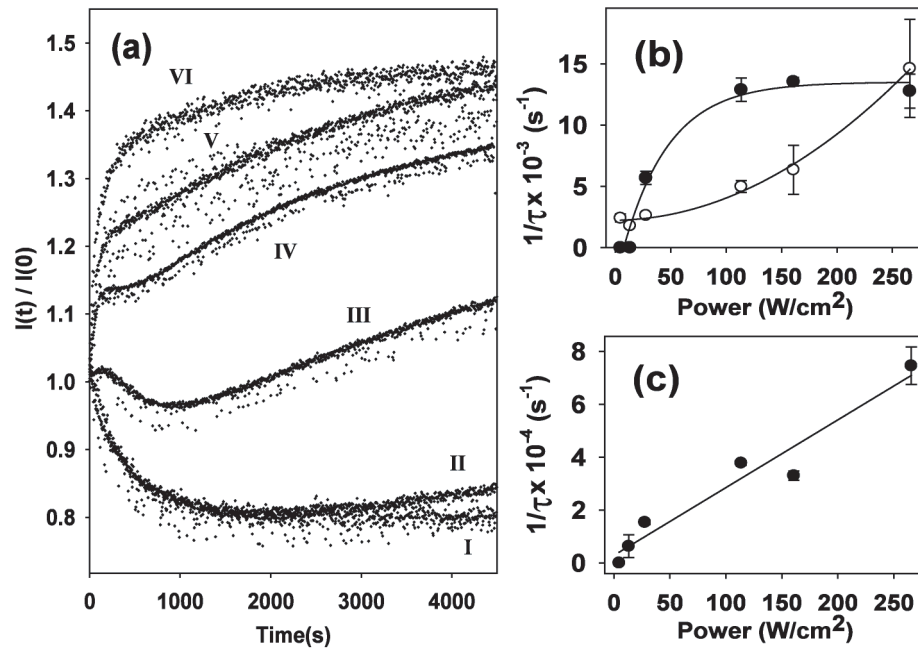


Figure 4.2. a) Normalized peak PL intensity of thin CdSe ( $a \sim 25\text{\AA}$ ) film tracked over exposure time to light and air at different powers: I( $5 \text{ W/cm}^2$ ), II( $13 \text{ W/cm}^2$ ), III( $28 \text{ W/cm}^2$ ), IV( $114 \text{ W/cm}^2$ ), V( $161 \text{ W/cm}^2$ ), VI( $266 \text{ W/cm}^2$ ). b) Inverse brightening times (closed circles) and inverse decay times (open circles) extracted from fitting data in a). c) The slower inverse brightening time from a). Error bars appear on all the points in (b) and (c), though not are all seen since some are comparable to the magnitude of the marker size.

ening dominates. There is an apparent competition between the darkening rate ( $I/\tau_d$ ) and the faster of the two brightening rates ( $I/\tau_{b,f}$ ) such that both rates increase with increasing power, as seen in Fig. 4.2B. The slow brightening rate ( $I/\tau_{b,s}$ , Fig. 4.2C) follows a weak linear dependence, implying that this rate is first-order in excitation power. This behavior follows a simple kinetic model whereby the  $n$  photons absorbed give rise to  $2n$  charge carriers that subsequently interact with surface traps to activate a proportional amount of luminescence. However, the fast brightening rate ( $1/\tau_{b,f}$ ) seems to saturate at  $\sim 0.014\text{s}^{-1}$  with increasing power, suggesting a steady state or equilibrium process for the PL arises at higher photon density. Using a trap-filling model, this can be attributed to saturation through passivation of available trap sites or through depletion of the CS population. That is, the brightening rate approaches a fixed value because the trap site density or CS population becomes the rate-limiting factor in the kinetics.

The darkening rate ( $1/\tau_d$ ) is also nonlinear in power, producing upward curvature with power as opposed to the fast brightening rate, showing downward curvature, as seen in Fig. 4.2B. The dependence of the darkening rate can be fit to the sum of linear and quadratic terms in power, and so it is likely that the physical origin of the linear term is related to the number of carriers available, and this quenching is due to irreversible photochemistry with gas adsorbates [61]. However, there is some reversibility in the darkening behavior that is independent of the presence of any gas [36], and accounts for the origin of the nonlinear darkening rate. This darkening rate increases with carrier density in the QD, leading to many-bodied carrier interactions, such as Auger processes,

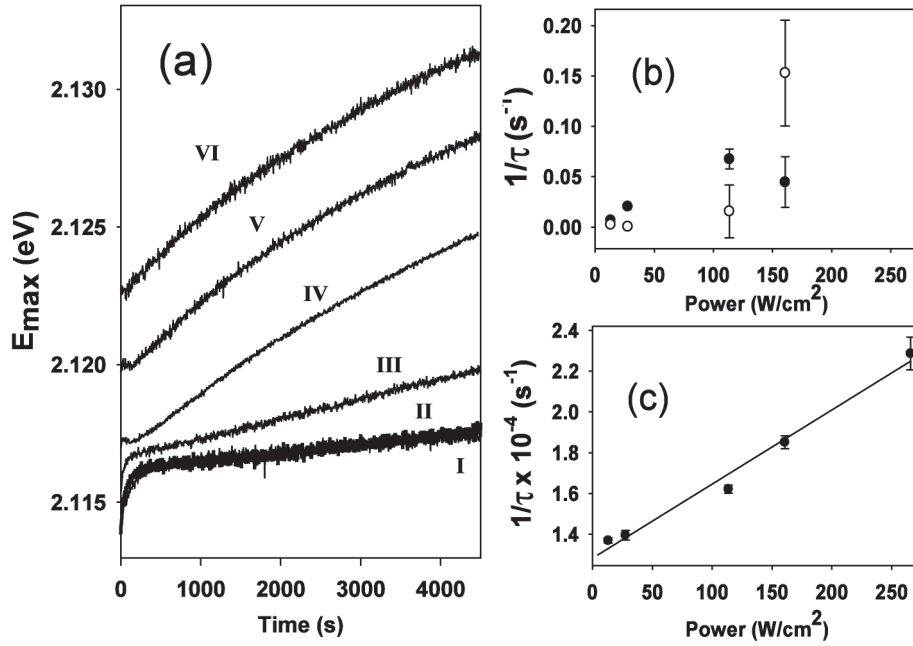


Figure 4.3. a) Peak energy of PL of thin CdSe ( $a \sim 25\text{\AA}$ ) film tracked over exposure time to light and air at different powers: I( $5\text{ W/cm}^2$ ), II( $13\text{ W/cm}^2$ ), III( $28\text{ W/cm}^2$ ), IV( $114\text{ W/cm}^2$ ), V( $161\text{ W/cm}^2$ ), VI( $266\text{ W/cm}^2$ ). b) Inverse time constants for blue shift (closed circles) and red shifts (open circles) extracted from fitting data in a). c) The slower inverse blue shift time constants from a).

which become an important part of the kinetics and are manifested in the darkening rates. Auger processes quench the PL, and since they scale nonlinearly with the number of carriers, they are strongly power-dependent. While Auger photoionization [13] depends on the number of surface traps available and saturation is expected (analogous with the fast brightening rate), it is not necessarily surprising that saturation is absent since Auger electron-hole energy transfer [26] can induce heating of conduction or valence band core-localized charge carriers and are independent of any surface effect, such as traps.

Fig. 4.3 shows the PL peak energy for the same powers used in Fig. 4.2,



where it can be seen that the spectral acquisition runs in Fig. 4.3A show a reversal in energy shift for nearly every run in Fig. 4.3A for  $t < 200$ s, and that the reversal directions are different for different powers. These spectral shifts are treated like intensity changes of Fig. 4.2 by fitting with sums of exponentials, resulting in the time constants found in Fig. 4.3C and Fig. 4.3D, which are remarkably similar to the trends found in Fig. 4.2B and 4.2C. This suggests that the intensity shifts and spectral shifts are correlated, as expected if the redder PL arises from CE dots. Fig. 4.3B shows a nonlinear response of the blue-shifts and the red shifts, with the blue shift showing downward power curvature (similar to the fast brightening rate), and the red shift showing upward power curvature (similar to the darkening rate). In addition, the slow blue-shift that is dominant at longer times and the slow brightening rate are both linear with power, implying that these are correlated. Thus, fast brightening is correlated with a blue-shift in the spectrum, which is due to the shift in the equilibrium from the *redder* CS dots to the *bluer* BEE dots. On the other hand, darkening is always correlated with a red-shift in the spectrum, due to a shift from the *brighter* BEE dots to the *darker* CS dots. Finally, permanent photodegradation induces blue-shifts also [61], and is linked to the slow brightening and slow blue shifting rates, implying complementarity.

The invocation of Auger processes to explain the brightening and darkening kinetics appears plausible upon analysis of the intensity fluctuations embedded in nearly all of the spectral acquisition runs. The times when the dot remained dark could not be observed, which is possibly due to the disparity between the dark interval times and the exposure time. Although this is clearly not a single-

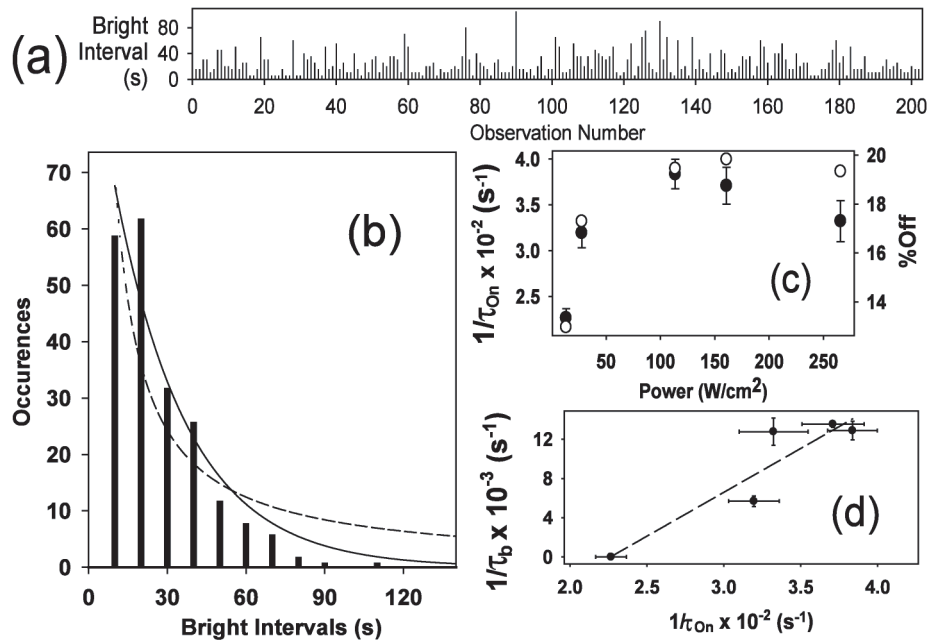


Figure 4.4. a) Bright intervals extracted from residuals similar to Fig. 4.1. b) Histogram of the bright intervals obtained from a) with an exponential (solid line) and power law (dashed line) fit. c) Bright interval time constant ( $\tau_{On}$ ) extracted from exponential fits to histograms like b) (left axis). Percentage of fluctuating spectra (right axis). d) Correlation diagram between the bright interval time ( $\tau_{On}$ ) in c) and the fast brightening time ( $\tau_{b,f}$ ) in Fig. 4.2B

dot experiment, these sharp drops in intensity are always present each time and become more frequent with increasing power. Occasionally, an intensity drop that is  $\sim 2$  times greater than the intensity fluctuations is observed and can be assigned to a process involving two dots switching off coincidentally during the collection interval. The residuals of a brightening trace, similar to Fig. 4.1, are processed to extract the intervals between these sharp drops in intensity and plotted as a function of scan number in Fig. 4.4A, where it can be seen that there is clearly no time-dependent trend. However, once a histogram is constructed with these intervals, as shown in Fig. 4.2B, a pattern clearly emerges, which can be fit to an exponential,  $\exp[-t/\tau_{on}]$ . A power-law fit,  $t^{-t/\tau_{on}}$  is also shown in Fig. 4.4A. From Fig. 4.4A, it is clear that the exponential fit agrees noticeably better with the data than the power-law fit. Both  $\tau_{on}$  and the relative number of fluctuation events ( $\%Off$ ) increase with increasing power (Fig. 4.4B), which is consistent with what is observed in the single-dot literature, as being due to Auger photoionization [37]. However, we can see that at higher powers, both saturate, mirroring the fast brightening rate, suggesting that charging and brightening are related processes.

Support for this relationship is found through correlation between the fast brightening rate ( $\tau_{b,f}$ ) and the bright interval time ( $\tau_{on}$ ), as shown in Fig. 4.4D. Such a correlation is expected since both the brightening rate and the bright interval time are related to the detrapping of charge carriers at surface trap sites. The bright interval time and brightening times show positive correlation, further proof that these two effects are not competitive but complementary, and possibly even sequential.

## 4.5 Chapter Summary

In summary, we propose a model that begins with the initial nonresonant laser excitation from the QD crystal ground state (CGS), followed by fast carrier surface trapping resulting in a CS state, darkening the dot and shifting its emission toward lower energy. An equilibrium exists between the CS and BEE states, controlled by the pump power. The presence of that charge causes an otherwise non-interacting gas adsorbate to interact with the trap site, through attractive surface potential created by the carrier most likely due to the development of an excited state dipole [72] inducing either electrostatic charge solvation, or interaction of molecular orbitals. While the latter interaction leads to a photochemical reaction, the former possibility leads to the displacement of the surface-trapped charge by the gas adsorbate by pushing trapped charge density back into the dot core, producing a rapid brightening process. This is supported by the pump power increasing the brightening rate by producing more CS, effectively driving the equilibrium back to the BEE. In addition, darkening (through Auger processes) also increases with pump power due to stabilization of the CS persistence time, and is further supported by the increase of the PL intermittency. A second, slow and weakly power-dependent brightening process is observed which is likely related to the trap state passivation by gas adsorbates of the BEE population while the linearly power-dependent and slow darkening is due to the irreversible photo-oxidation of the CdSe QD surface. The changes in the PL intensity are correlated with the shifts in the peak energy, in strong support of the above model and stronger verification that we observe two excited state populations: a *brighter, bluer exciton state*

(BEE) and a *darker, redder exciton state* (CE). Finally, since brightening is positively correlated to intermittency, there is compelling evidence that a charged dot forms, then detraps, allowing us to conclude that photo-brightening and photo-induced charging are complementary processes.

## **Chapter 5**

# **Electronic Energy Transfer in a Semiconductor Nanocrystal - Molecular Wire Assembly**

Reproduced with permission from “Energy Transport in CdSe Nanocrystals Assembled with Molecular Wires.” A. Javier, C.S. Yun, J. Sorena, G.F. Strouse. *Journal of Physical Chemistry, B*, (2003), 107, 435-442. Copyright 2003, American Chemical Society

### **5.1 Introduction**

The physics of energy transfer[73] for organic[21, 74] and inorganic materials[75], as well as inorganic-organic hybrids[76], has been an intensive area of investigation for several decades. Recently, it has become an active area

in quantum confined systems[28] for both pure[77, 78] and applied[79] research, and the interaction of the electronic transitions in these dimensionally-confined hybrid systems[80, 81] has been pursued both theoretically[82] and experimentally[83, 84]. The phenomenon of quantum confinement of the Wannier-Mott exciton in CdSe below its Bohr radius[85] ( $a_B \sim 5nm$  in CdSe) and the Frenkel exciton in the organic system below its Frenkel radius ( $a_F \sim 3nm$  for conjugated  $\pi$ -systems[86, 87]) results in size-dependent electronic properties for nanometer-sized semiconductors and conjugated organic molecules. Specifically, the absorption and luminescence characteristics of nanocrystals in the strongly confined regime is size dependent, as shown in Figure 5.1. This allows for a unique opportunity to tune the energies of electronic transitions in both systems, and therefore the magnitude of the interaction of electronic transitions within a composite system.

### **Direct Energy Transfer in Hybrid Systems**

Energy transfer between the inorganic and organic components can be described both in terms of phase-coherent strong coupling and phase-incoherent weak coupling through the dipole-dipole interaction theoretically[88] recent experimental results suggest nanocrystalline materials and organic-inorganic hybrids are best described in the weak coupling regime[83]. This allows the application of Förster theory[74], which typically is used at the limit of “localized oscillators” as a result of the electric dipole approximation. The use of Förster theory allows the quantum efficiency of energy transfer to be related to the spectral overlap integral,  $\langle J \rangle$ , a quantity that accounts for the resonant

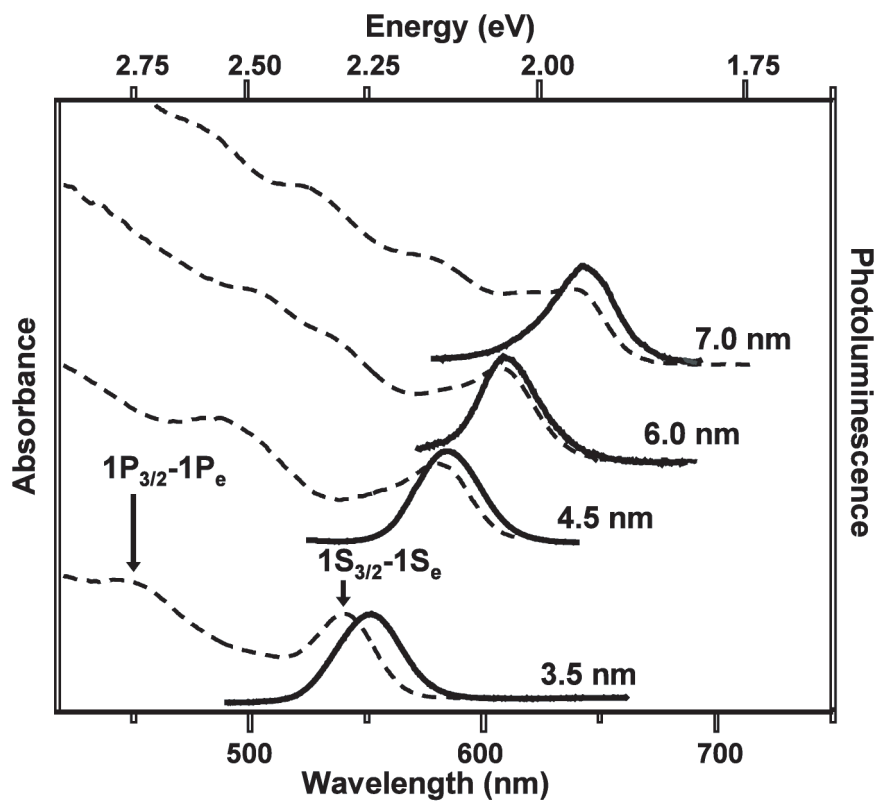


Figure 5.1. Room temperature absorbance (dashed) and photoluminescence (solid) spectra for a series of CdSe nanocrystals coated with TOP/TOPO (diameters given at the right) in toluene. The two prominent exciton transitions are shown.



coupling of the pseudo-continuous electronic transitions of the energy donor and the energy acceptor.

A caveat of the Förster theory approximation is that the magnitude of the coupling will be inversely proportional to the sixth power of the donor-acceptor separation distance, although in the tightly bound composite system where the exciton is largely delocalized over the donor or acceptor volume, the distance will effectively be invariant for a given oligomer length, giving rise to a rate of energy transfer, and consequently a efficiency of energy transfer, dependent on the magnitude of  $\langle J \rangle$ . The application of the weak coupling model arises due to the dissimilarity in the wavefunctions of the molecular orbitals in organic systems and band-like orbitals in nanocrystals that prevents traditional strong interactions. However, strong interactions arising from exciton delocalization within the organic system due to aggregate formation may influence the pathway for energy transfer within these composites.

### **Energy Migration in Hybrid Systems**

The  $\pi$ -stacking of organic systems can lead to aggregates[89] that result in a variety of new pseudo-particles that are not present in the isolated system. As these units are brought closer into contact, a critical stacking distance is surpassed ( $< 0.7nm$ ) that induces drastic changes in the electronic structure of the organic system[90, 91]. Interaction of two monomer units can result in low-order exciton delocalization into simple dimers, excimers or polaron-pairs[92], while the participation of many monomer units can result in high-order exciton delocalization, or aggregate excitons. The new electronic transitions that

arise also participate in energy transport processes and must be included in a complete description of the total energy transfer mechanism. Therefore the pathways of energy transfer in composite systems will be strongly influenced by the packing interactions of the conjugated organic system and their respective populations within that system, as these interactions give rise to the species mentioned above. In the present study, we investigate nanocrystal composites where the photo-excited molecular wire donates energy to the nanocrystal in the form of an electronic excitation. The resonant energy transfer interaction which couples the energy donor (the molecular wire) to the energy acceptor (the nanocrystal) can be tuned in these assemblies by tuning both the length of conjugation in the molecular wire and the nanocrystal size. Moreover, dimers and aggregate excitons are present in these assemblies suggesting that these species interact with the nanocrystal exciton.

## **5.2 Experimental Methods**

### **5.2.1 Synthesis of the CdSe Nanocrystals and the Organic Molecular Wires**

The series of oligo-p-(phenylene-ethynylene)n-dibenzylthiols (n=0,1,3) (O-PE-n) was synthesized by a modification of literature methods[93, 94]. In brief, benzylic thiol formation was achieved by the radical benzylic bromination of 4-iodotoulene followed by nucleophilic substitution with potassium thioacetate. Deprotection of the thiols was done in a basic methanolic solution, purification

by column chromatography and isolation under  $N_2$ , in order to prevent oxidation of the terminal thiol. CdSe nanocrystals between 2.8 nm and 8.0 nm were synthesized as TOP/TOPO passivated nanocrystals by standard lyothermal methodology[95]. Excess TOP/TOPO was removed by repetitive (3x) dissolution of the particles in toluene and precipitation by addition of MeOH.

### **5.2.2 Sample Preparation for Optical Experiments**

CdSe-OPE films were prepared under Ar by slow addition of a 2 mL toluene solution of 0.05M OPE-n to 5 mL of a 0.1 mg/mL CdSe NC in toluene at room temperature. The reaction was allowed to react 24 hours under Ar, producing a solid, which was washed repeatedly with toluene to remove excess CdSe NCs and OPE, then suspended by sonication in fresh toluene for film deposition. Control experiments were conducted on OPE-n protected with terminal acetyl groups on the thiols. CdSe-OPE thin films were prepared by drop casting the suspended material in toluene onto 25.4 mm wide, 0.5mm thick circular sapphire flats. CdSe and thioacetate protected OPE-n films were prepared by drop casting a mixture of CdSe and OPE-n in a minimum volume of toluene onto a sapphire flat.

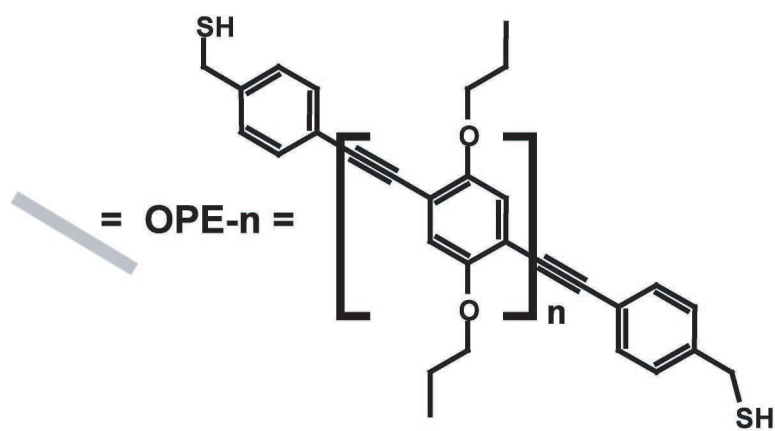
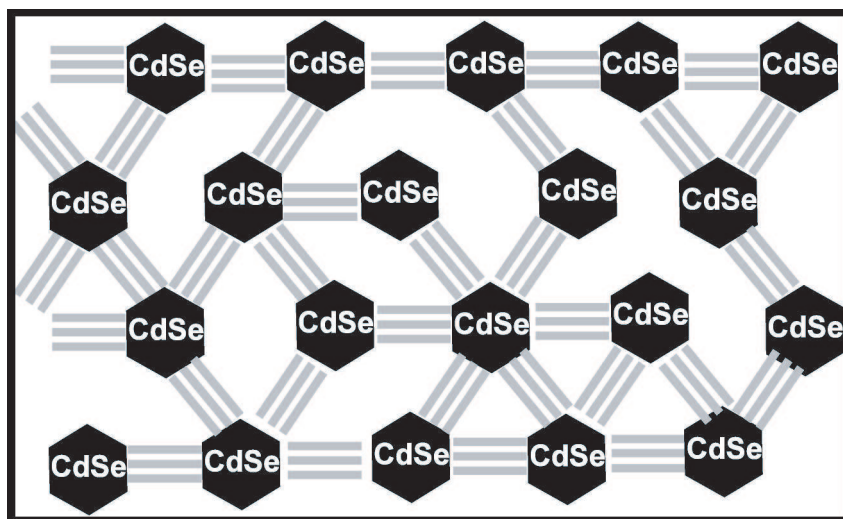


Figure 5.2. TOP: Scheme of CdSe-OPE-n assemblies. CdSe nanocrystals, coated with TOP/TOPO, form amorphous, cross linked assemblies by ligand exchange of the phosphine by the thiol moiety when reacted with OPE-n: oligo-(p-phenylethynylene dibenzylthiol dipropyl ether) (OPE-n, n= 0, 1, 3) BOTTOM: Lewis structure of OPE-n molecules.

## **5.3 Physical Characterization of CdSe/OPE-1 structures**

### **5.3.1 Electron Microscopy**

Transmission electron microscopy (TEM) analysis was performed on 400 mesh Cu grids coated with a  $\sim 5nm$  layer of holey carbon (SPI). Images were obtained on a JEOL 2000 or JEOL 2010 microscope operated at 200 kV in bright field mode.

### **5.3.2 Optical Spectroscopy**

Emission measurements were conducted on samples drop-cast onto sapphire substrates oriented either at  $45^\circ$  or front-face excitation using a continuous wave Omnichrome HeCd laser ( $\lambda_{exc} = 325nm, \sim 1mW$ ) with a UV filter to reject stray plasma or a 75W Hg lamp with a 313nm bandpass filter. The luminescence data was collected with an F/1 optic and dispersed on a CVI Instruments Digikrom 240 monochromator (150 g/mm, 10 m slit width) coupled to a SBIG CCD Model ST-6. The laser line or lamp profile was removed by a UV filter.

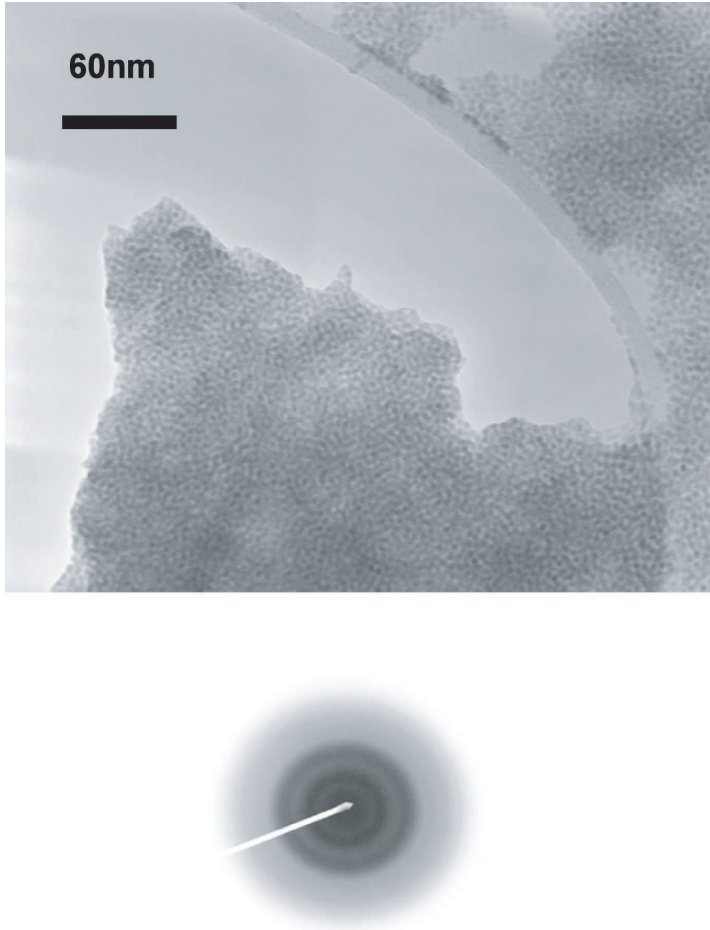


Figure 5.3. Transmission Electron microscopy of CdSe-OPE-n nanocrystal assemblies. TOP: TEM of CdSe-OPE-3 assembled structures. An aggregate of CdSe-OPE is suspended over one a hole of the carbon grid. BOTTOM: Small Angle Electron Diffraction (SAED) pattern from TEM. The observed rings indicate incorporation of wurzite CdSe into the composite without long range ordering of the CdSe nanocrystals.

## 5.4 Results of Optical Studies

### 5.4.1 Scaffolding of the CdSe Nanocrystals

Slow introduction of OPE- $n$  ( $n = 0,1,3$ ) to a solution of CdSe in toluene at RT produces a solid monolith (Figure 5.2). TEM analysis of the CdSe(4.5nm)-OPE-1 monolith show closely packed CdSe nanocrystals (Figure 5.3) lacking orientational order based on SAED ring patterns (Figure 5.3, inset). Similar observations are found for composites formed with OPE-0 and OPE-3. The phenylethynylene core of the organic oligomer which has been used for molecular wire applications[96, 97] was chosen for both its rigidity and low conductivity, the latter of which enhances energy transfer phenomena by impeding the competing phenomenon of electron conduction. The placement of a methylene group between the thiol and the phenyl rings serves to interrupt the conjugation preventing photochemical redox processes at the nanocrystal surface by raising the oxidation potential of the thiol. The assembled monolith cannot be redispersed in solvent following precipitation. Optical absorption in these materials suggests that the composite is composed of  $> 100 : 1$  mole ratio of oligomer to CdSe. Unfortunately, complications arising from light scattering in these solutions limit the accuracy of determination of the mole ratios using absorption measurements.

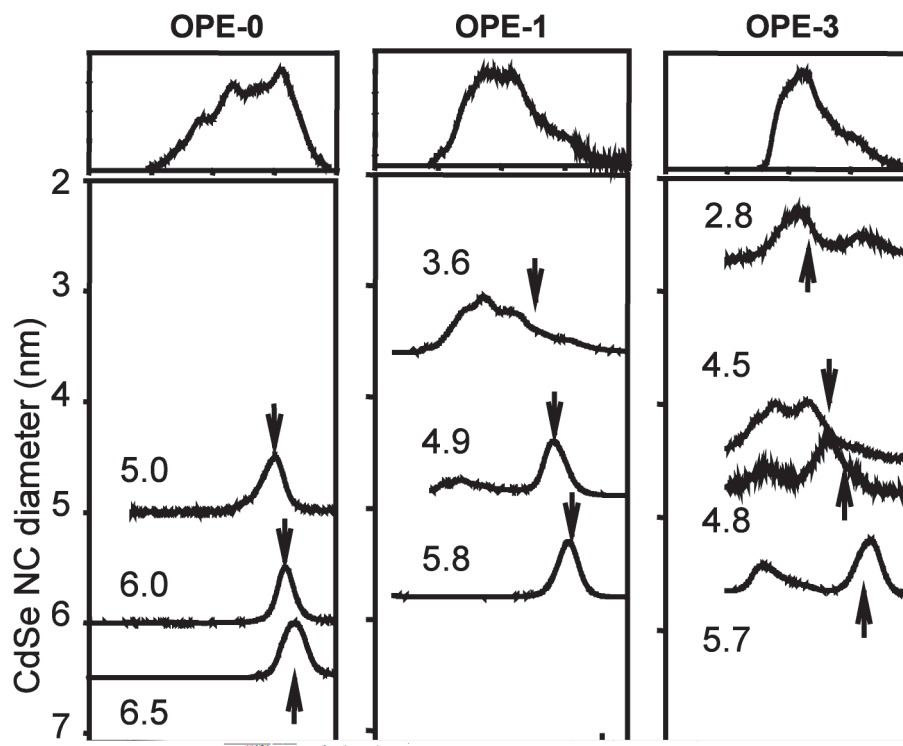


Figure 5.4. Photoluminescence spectra of thin films of OPE-n (top row) and CdSe-OPE-n assemblies at room temperature ( $\lambda_{\text{exc}} = 325\text{nm}$ ,  $\gg 1\text{mW}$ ). Columns pertain to OPE-n sizes ( $n=0, 1, 3$ ) while rows indicate CdSe NC diameters in nanometers. Arrows indicate the expected position of nanocrystal luminescence



## 5.4.2 Photoluminescence Spectra

The PL spectra of OPE-n and OPE-n/CdSe composites when excited at 325nm is shown in Figure 5.4. There is an overall trend in the reduction of the presence of the OPE-n luminescence relative to the nanocrystal band-edge luminescence as the nanocrystal size is increased (from top to bottom) and the oligomer chain length is decreased (from right to left). In fact, for the CdSe-OPE-0, nanocrystal emission is exclusively observed. For assemblies containing CdSe. For sizes below CdSe(4.9nm)-OPE-1, a contribution of the PL from both the nanocrystal and OPE-1 is observed. For the CdSe-OPE-3 sample, contributions from both CdSe and OPE-3 are observed. For all the CdSe-OPE-3 samples studied with strong aggregate components, no PL is observable at 570 and 603nm. No significant contributions from deep trap luminescence from CdSe is observed in the composite structures. In general, there appears to be an improvement in the signal/noise ratio in assemblies with increasing nanocrystal size, implying that the PL quantum yield for these are greater. Exact measurements of quantum yields have not been explicitly measured. The change in the relative contributions of the PL of the two components is a function of nanomaterial size and OPE-n length. The total PL manifold can be assigned by inspection of the concentration dependence of the PL of OPE-1 (Figure 5.5), and the size dependent emission of the nanomaterial. Upon closer inspection of the PL manifold, changes in OPE-n are observed which appear to depend upon nanocrystal size.

Figure 5.5. Concentration-dependent photoluminescence spectra of OPE-1 in toluene at room temperature ( $\lambda_{exc}=325\text{nm}, \sim 1\text{mW}$ ). Inset: Room temperature absorption Spectra of OPE-1 in toluene at the corresponding PL concentrations. Note that both have been normalized to the absorption or luminescence of the molecular species.

## Interchain Transitions of the Molecular Wire

These observations can be understood when considering the effects of interchain interactions that form dimers and aggregate interactions of OPE-n. At very low concentrations ( $10^{-7}M - 10^{-12}M$ ), the luminescence spectrum of OPE-1 arises almost exclusively from the molecular exciton, consisting of the  $S_1 \rightarrow S_0$  transition and its vibronic progression (A, B). A low energy band at 535 nm is assignable to a phosphorescent  $T_1 \rightarrow S_0$  (F), giving a singlet-triplet energy difference  $E_{ST} \sim 1eV$ , which is consistent with typical exchange energies in organic systems. Its strength relative to the singlet fluorescence implies significant mixing of singlet and triplet states, possibly due to increased spin-orbit coupling from the sulfurs in the thiols. As the concentration is progressively increased, contributions from dimers begin to appear as new bands in the PL that are shifted to the red (C, D, E) along with a corresponding new band in the absorbance at 390nm (J) that is red-shifted from the absorbance of the monomer OPE-n (I). Spectral subtraction of the lowest concentration PL spectrum from the higher concentration PL spectra reveals an emission manifold that is structured. This implies that as the concentration is increased, a new species with distinct vibronic structure (C, D, E) is formed with the coincident decrease in the contribution from the isolated OPE-n. The presence of the new absorbance band (J) with increasing concentration implies a ground-state dimer is being formed, but since it is not directly being photo-excited, the luminescence must come from the migration of the energy of the molecular exciton to these dimer states via energy migration. PL excitation spectra of the new bands in the PL overlay very well on the absorbance, especially band J, indi-

cating that these dimer states are the source of the new luminescence. Changes in the relative intensities of these bands in the absorbance spectra with respect to concentration suggest aggregate formation arising from  $\pi$ -stacking effects between OPE-n molecules. When OPE-n is cast as a film, contributions from higher order aggregates arise at lower energy as seen in Figure 5.5 (G, H). It can also be seen from the PL that the bands originating from the molecular species are no longer present, suggesting in the film the observed PL arises primarily from dimeric species and aggregate bands. The presence of the OPE-n molecular species in the absorbance of the film, suggest facile exciton migration to the dimers and aggregates following excitation of the OPE-n molecule. No noticeable band structure evident in the film absorbance accounts for the new aggregate peaks (G, H) found in the luminescence. Similar aggregate spectra arise in PPE, the polymeric variant of the oligomer being studied[98]. These results suggest that exciton states exist in this system that can be described as being delocalized over a larger volume due to interchain interactions and therefore may serve as low energy emissive traps. The actual interaction involves cofacial alignment of planar  $\pi$ -systems[99, 91] which causes a splitting of the molecular orbitals, resulting in a symmetry-forbidden lowest energy excited state recombination. Electron-phonon coupling[100] or misalignment relaxes the selection rule, allowing radiative decay of the lower state which results in a red-shift in the luminescence. Aggregate states can be described as an extension of this model to larger numbers of participating units, causing the energy splitting to be much greater, and therefore to be more red-shifted, just as we observe in the OPE-1 film. The acetyl protected OPE-n also displays new luminescence features when cast into a film. The spectral differences be-

tween the protected and unprotected versions can be explained as a sensitivity of aggregate states to their packing arrangement, which in other studies has been found to strongly depend on many factors, even film preparation<sup>45</sup>.

### **Interchain Transitions within the Hybrid assembly**

As stated earlier, when OPE-n is assembled with CdSe, we observe changes in the OPE-n PL spectrum that are dependent on CdSe size. We can group these changes into three observations, i) the aggregate bands (G, H) appear in these assemblies regardless of the CdSe size used, ii) the dimer bands (C, D, E) of OPE-n appear in the smallest CdSe sizes (2.8nm, 3.6nm), but are not present in the intermediate and larger sizes, iii) the OPE-n molecular luminescence (A, B) appears in the intermediate CdSe sizes only (4.5nm,5.5nm) and not in larger or smaller sizes. Another noticeable result is that the triplet band is not present in the larger nanocrystal sizes (5.0nm in OPE-1), implying that this OPE-n excited state is also coupled to the nanocrystal. These effects are all indicative of a complicated mechanism involving the interactions of individual OPE-n excitations with the size-dependent electronic transition energies of the nanocrystal. In order to understand how OPE-n interacts with these changes, we employ the simplest model involving the interaction of the OPE-n molecular exciton with the nanocrystal, and apply the simplest mechanism, Förster energy transfer. We will later use this model to provide some insight into the interaction between dimer states and aggregate states with the nanocrystal.

## 5.5 Size-dependent energy transfer

### 5.5.1 The Förster Model

#### The Relevance of the Förster Model

Electronic energy transfer in these materials originates from a transition dipole-dipole interaction between the many discrete transitions of the organic oligomer, OPE-n and its aggregates to the discrete and continuum-like states of the nanomaterial. The nature of the interaction can be described in terms of a strong or weak coupling regime between the donor and acceptor states<sup>3</sup>. The amorphous nature of the inorganic-organic hybrid structure for CdSe-OPE-n structures with respect to nanocrystal orientational order (Figure 5.3, inset), the inhomogeneous distribution of CdSe sizes resulting in non-identical potential wells, the lack of periodicity, and the resulting dissimilar discrete transition energies between the CdSe and OPE-n eliminates the strong coupling regime. In the weak coupling limit, the resonant energy is irreversibly transferred from the donor to the acceptor due to the lower lying acceptor electronic transition acting as an energy trap. Assuming vibrational relaxation occurs faster than energy transfer (a result of being in the weak limit) the energy transfer mechanism can be described as a combination of coulombic (Förster mechanism) and exchange (Dexter mechanism) interactions. The strength of the exchange interaction drops off exponentially with respect to the donor-acceptor separation distance, and is only a major contributor to the total energy transfer if all other resonant transitions are forbidden. Therefore, in this case, the energy trans-

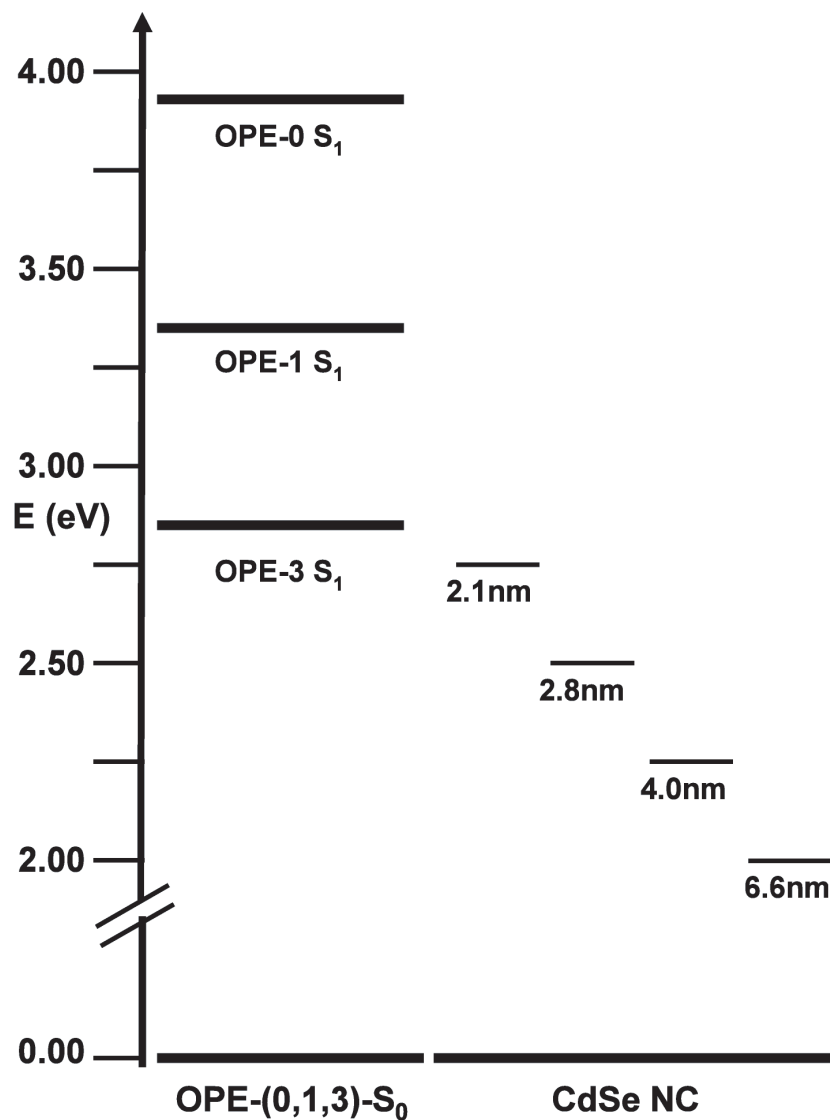


Figure 5.6. Excitation energy diagram for OPE (left) and CdSe (right). The electronic excitation energies of the singlet states have been estimated from the crossing of the absorption and luminescence curves. The exciton energy for the ( $1S_{3/2} - 1S_e$ ) has been estimated from the exciton maximum in the absorbance spectrum, and is shown along with the continuum of gap states.

fer should be well described in a limiting condition as a coulombic interaction between the electronic system of the donor and the electronic system of the acceptor. Observation of the aggregate states in the spectrum confirm the facile relaxation to the lowest organic levels prior to energy transfer, supporting the weak coupling approximation. Within this mechanistic framework, two competitive models exist that describe energy transport, Förster's model involving localized dipole oscillators and an exciton diffusion model. It is likely that the Förster model is the more applicable model due to the short lifetimes of CdSe trapping the excitation more efficiently and the lack of very long-range crystalline domains, effectively reducing exciton mobility. A time-resolved study on a system similar to ours suggests exciton diffusion may play a role in describing the energy transfer mechanism[83], this may be due to contributions arising from aggregates, as discussed later.

### **Applying the Förster Model**

In the CdSe-OPE-n system, with a fixed donor-acceptor distance, the very strong oscillator strengths of the OPE-n and CdSe transitions indicate that the energy transfer process is dominated by the strength of the resonant coupling energy, quantified as the spectral overlap integral  $\langle J \rangle$ .

$$\langle J \rangle = \int_0^{\infty} F_D(\lambda) \lambda^4 \epsilon_A(\lambda) d\lambda \quad (5.1)$$

where  $F_D$  is the normalized fluorescence intensity of the donor, and  $\epsilon_A$  is the molar extinction coefficient of the acceptor. According to Förster's



theory[101], the rate of energy transfer ( $k_{EnT}$ ) is:

$$k_{EnT} = \frac{9000 \ln(10)}{128\pi^5} \frac{\kappa^2 \Phi_D}{\eta^4 N_A r^6 \tau_D} \langle J \rangle = \frac{A}{\tau_D} \langle J \rangle \quad (5.2)$$

where  $r$  is the distance between the donor and acceptor dipoles,  $\Phi_D$  and  $\tau_D$  are the native quantum yield and lifetime of the donor respectively,  $\kappa$  is the relative orientation of the donor and acceptor dipoles,  $\eta$  is the refractive index of the medium,  $N_A$  is Avogadro's number. We estimate the orientation factor  $\kappa^2 = 2/3$ , consistent with an isotropic orientation of transition dipoles within the assembly, which is reasonable considering the disorder in nanocrystal orientation observed in the SAED spectrum in Figure 5.3. For the CdSe-OPE-n system, we have grouped invariant terms for a given organic donor into  $A$ , leaving  $k_{EnT}$  to be directly proportional to  $\langle J \rangle$ . The quantum efficiency of energy transfer ( $\Phi_{EnT}$ ), an experimental observable, can be expressed as a ratio of the rate of energy transfer ( $k_{EnT}$ ) to the sum of the rates of all processes that deactivate the excited state ( $\sum k_i$ ):

$$\Phi_{EnT} = \frac{k_{EnT}}{\sum k_i} \quad (5.3)$$

The quantum efficiency of energy transfer ( $\Phi_{EnT}$ ) in terms of  $\langle J \rangle$  in these hybrid nanocomposites can then be expressed by substitution of (2) into (3):

$$\Phi_{EnT} = \frac{\langle J(R) \rangle}{\langle J(R) \rangle + A^{-1}} \quad (5.4)$$

This allows the rate ( $k_{EnT}$ ) and efficiency ( $\Phi_{EnT}$ ) of energy transfer to be

interpreted entirely by analysis of the spectral overlap integral, which, holding all else constant, is entirely dependent upon CdSe size ( $R$ ).

### **Size-dependence of the Overlap Integral**

This occurs because  $\langle J \rangle$  is a complicated function of the nanocrystal size. For example, if we consider only the  $1S_{3/2} - 1S_e$  transition, we find that the magnitude of the extinction coefficient in CdSe is proportional to the volume ( $\sim R^3$ )[102] and that the energy of the transition is proportional to the inverse square of the radius ( $\sim R^{-2}$ )[85]. The higher order transitions also follow a similar trend though their oscillator strength is not as large[7].  $\langle J \rangle$  increases with increasing nanocrystal size due to the greater overlap of  $\epsilon_A$  with  $F_D$ , and consequently, the rate of energy transfer also increases. Figure 5.6 shows the OPE-n molecular exciton energies relative to the lowest energy CdSe discrete ( $1S_{3/2} - 1S_e$ , solid line) and other higher order and continuous transitions (gray bar) with different CdSe sizes. The OPE-n molecular exciton is always resonant with some CdSe electronic transition, but the dimer states progressively increase in their overlap with CdSe as the size increases, which would in turn lead to greater energy transfer from those states. As the CdSe size is increased above 3nm, the nanocrystal exciton ( $1S_{3/2} - 1S_e$ ) becomes resonant with the OPE-n dimer exciton, and energy transfer is predicted to be more efficient. As the CdSe size is increased further, the  $1S_{3/2} - 1S_e$  nanocrystal exciton is no longer resonant, but OPE-n dimer states remains resonant with other higher energy excitons, as well as a higher density of continuum states, contributing to a general increase in the energy transfer as a function of size.

A similar effect occurs for the aggregate states, but at much larger CdSe sizes. Plots of the spectral overlap integral  $\langle J \rangle$  more clearly illustrate this, as shown in Figure 5.7. Inspection of the calculated value of  $\langle J \rangle$  using the OPE-n protected film luminescence with different nanocrystal extinction spectra (Figure 5.7) reveals that the smallest CdSe sizes show an overlap of the blue edge of OPE-n with the red edge of CdSe(2.5nm). As the CdSe size is increased, the decrease in the CdSe bandgap causes all of the transitions to shift toward the red, overlapping with more OPE-n states, until in the largest size of CdSe (CdSe(6.5) also seen in Figure 5.7) the entire OPE-n luminescence is resonant with either discrete transitions in CdSe or the continuum of bandgap states. This allows the trend in the magnitude of the relative emission in Figure 5.4 to be analyzed by consideration of the size-dependent change in the spectral overlap integral between the OPE-n and the CdSe nanomaterials. For a given family in Figure 5.4, the QD/oligomer concentrations were kept constant, however, the exact concentrations in the final assemblies are difficult to assess. As the spectral overlap increases, an increase in quenching of the OPE-n PL is expected with a corresponding increase in the nanocrystal PL contribution. Förster theory therefore predicts a relative increase in the ratio of CdSe band-edge luminescence to OPE-n luminescence with increasing nanocrystal size (moving vertically downward in Figure 5.4) and decreasing OPE-n chain length (moving horizontally to the left in Figure 5.4).

There are many factors that change dramatically as one moves horizontally in Figure 5.4, including the separation distance and the excited state lifetime. Although Förster's theory has an exact distance dependence, it is only explicit

for distances that are greater than the donor and acceptor dimensions. That is, both the nanocrystal and OPE-n excitons are delocalized across their volumes and are at very close proximity, effectively blurring the exact separation distance. At the relatively short donor-acceptor distances used in these assemblies, the distance dependence of the energy transfer is not expected to be significant. The simple Förster model discussed above describes an average interaction between OPE-n and CdSe. This model, however, does not account for the difference in the luminescence intensity ratios between CdSe-OPE-1 and CdSe-OPE-3, nor does it account for the change in the OPE-n manifold as the nanocrystal size is increased.  $\langle J \rangle$  values between different OPE-n ligands with the same nanocrystal size are very similar, which suggests that another mechanism is responsible for the noticeable change in luminescence when switching organic systems that is unrelated to the resonant interaction between OPE-n and CdSe. This may be attributed to a number of different factors including luminescence lifetime, changes in extinction coefficient and especially differences in packing environments on the nanocrystal surface, all of which may contribute to the resulting luminescence.

Part of the answer lies in the aggregate species that are present as a result of OPE-n interactions with itself. It should be stressed that the calculations for  $\langle J \rangle$  are made with the solid-state luminescence spectra of the OPE-n, which has contributions from aggregates whose populations will differ in the assemblies. In the CdSe-OPE-n assemblies, the aggregate populations will be disturbed by the nanocrystal presence due to changes in the packing interactions. This results in a distortion of the OPE-n luminescence data due to the

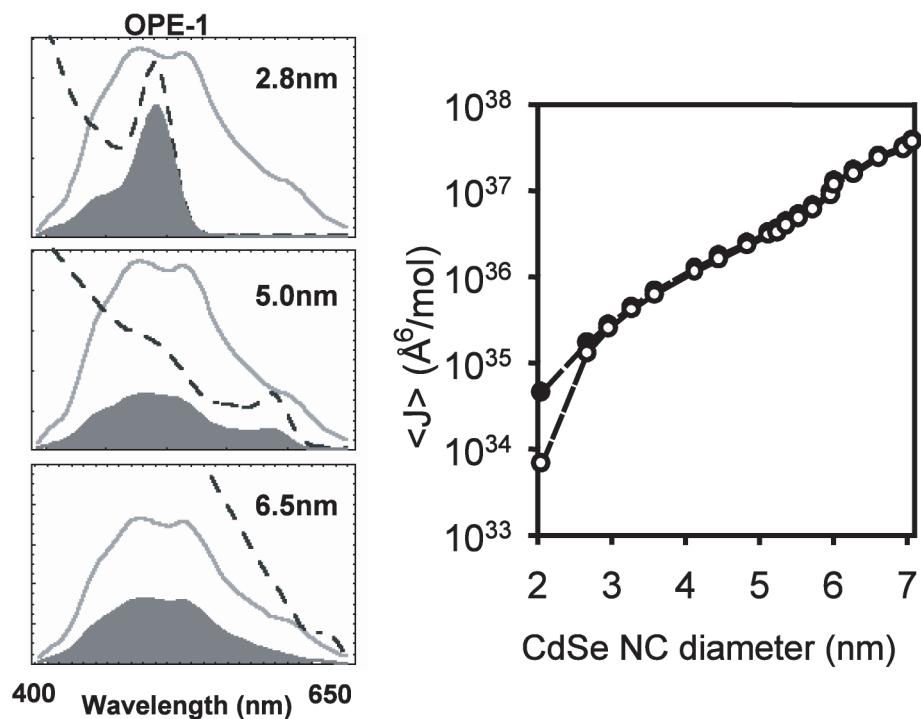


Figure 5.7. Left: The luminescence of OPE-1-protected Film, the absorption of CdSe in toluene at 298K and the spectral overlap integral (filled in) for three representative sizes of CdSe. Top: Plot of  $\langle J \rangle$  for OPE-1 (closed circles) and OPE-3 (open circles).

differences in orientation or different micro-environments of the OPE-n, which lead to changes in the energy transfer.

## 5.5.2 Higher Order Transitions

### Aggregate and Dimer Bands

The spectral changes that accompany the quenching in these assemblies are suggestive of aggregate and dimer participation in the energy transfer. While these assemblies are generally amorphous with respect to nanocrystal place-

ment, the presence of local dimers and aggregate conformations within the assemblies can be inferred from inspection of the PL spectra. Luminescence from higher order structures is clearly visible in the PL spectra of the assemblies in nearly every size nanocrystal and may cause some distortion to the nanocrystal band-edge luminescence in the higher sizes due to overlap, which is highly suggestive that aggregate formation of OPE-n occurs on the nanocrystal surface. Comparison of the PL data for the CdSe-OPE-n composite (Figure 5.4), with the PL (Figure 5.5) for OPE-n shows an apparent distortion in the remnant OPE-n luminescence that causes the spectrum for the OPE-n to shift toward the "blue," as is clearly seen in CdSe(4.8)-OPE-1 and CdSe(4.9 and 5,7)-OPE-3. Closer inspection reveals that there is no shift, rather this occurs due to changes in the intensities of the OPE-n luminescence manifold composed of molecular, dimer and aggregate excitons. The apparent shift can be interpreted as preferential quenching of the lower energy dimer-like transitions preferentially in the composite. These lower energy transitions (C, D, E) disappear with increasing nanocrystal size, and quench faster than the molecular PL (A, B), thereby causing the overall OPE-n luminescence to appear as though it were shifting toward the blue. This observation implies two possibilities: that the interaction between this delocalized dimeric excitation and the nanocrystal excitonic states are stronger than the molecular excitation coupled to the same excitonic states, or that increasing nanocrystal size induces less association among OPE-n ligands. The latter case is unlikely since larger nanocrystal sizes have larger stable crystal facets and should increase the occurrence of domains of dimer species and aggregate domains at the expense of the molecular species. We would in this case observe a reduction in the molecular luminescence with a correspond-

ing increase in the dimer and aggregate luminescence. We observe, however, the opposite effect - the molecular luminescence grows in and the aggregate luminescence is apparently unaffected, but the dimeric luminescence decreases. In fact, aggregate bands appear quite prominently in the smallest nanocrystal sizes, implying that even at these small facet sizes, an aggregate domain can form stably. This leaves the former case, that there must exist a strong interaction between the discrete nanocrystal exciton states and the dimer state of OPE-n.

### **Higher Order Nanocrystal Excited States**

This is not a surprising result since the rate of energy transfer in Förster theory is based upon the strength of resonant transition dipoles, and the nanocrystal oscillator strength is carried predominantly by the  $1P_{3/2} - 1P_e$  and  $1S_{3/2} - 1S_e$ , which happen to be resonant with the OPE-n dimers over the participating nanocrystal sizes. For example, with CdSe roughly in the 4.5 to 5.5nm range, the  $1P_{3/2} - 1P_e$  overlaps extremely well ( $\sim 450 - 500nm$ ) with the dimer luminescence ( $\sim 435 - 500nm$ ). It is possible that the  $2S_{3/2} - 1S_e$  transition also plays a role in the quenching since this transition is also resonant with the dimer states, however it is expected to be due to its resonance with the dimer states rather than its oscillator strength, which is expected to be quite low[39]. The variance of this phenomenon between similar sizes of CdSe, such as CdSe(4.5)-OPE-3 and CdSe(4.8)-OPE-3 is due to the size-dependent changes in the discrete transition energies of the nanocrystal. We stress that the coupling to the continuum of bandgap transitions would not

have the same effect as these increase monotonically toward higher energies and would therefore favor the quenching of higher energy transitions such as the isolated molecular luminescence, which is the opposite of what we observe. Moreover, this effect is not seen in the lowest energy organic system luminescence, the aggregate excitons, since these are the lowest energy states of the composite system.

### **5.5.3 Energy Migration**

The occurrence of dimers and aggregates within the assemblies complicates the simple Förster model of energy transfer. Figure 5.8 is a schematic of the possible pathways for the electronic energy to pursue within the assembly. The excitation originates from the optical pumping of either the OPE-n ligand or the nanocrystal, with the former being the preferential path. Vibrational relaxation occurs first (consistent with a weak coupling model), at which point the excitation can either transfer to the nanocrystal by the Förster mechanism, or become delocalized among different adjacent OPE-n ligands (the former is the preferred path). Low order delocalization can occur to a small number of adjacent OPE-n ligands (dimers) or high order delocalization can occur to a large number of OPE-n ligands (aggregates). These low-order delocalized states can be the dimers mentioned above, excimers or polaron pairs[103], formed due to photo-induced electron transfer to a cofacial molecule, which effectively delocalizes the exciton, or resonant energy transfer to dimer or aggregate states. We have little information indicating which is predominantly observed. Low order delocalized states can transfer their energy to the nanocrystal, while the



aggregate excitations need not. This occurs because the aggregate bands are found lower in energy than the nanocrystal exciton states and as a result are the lowest excitation energy states in several of these assemblies. Due to the low cross section for aggregates in the inorganic-organic composites, the number of aggregate excitons (traps) is difficult to determine directly in these materials. However, the population of aggregate states should increase with increasing chain length and nanocrystal size due to more efficient packing on a nanocrystal facet[104].

Although the concentration of aggregates is small, theory infers very fast (picosecond) Förster energy transfer from a semiconductor nanocrystal to an organic matrix[105]. In a variety of the assemblies present, particularly those with small nanocrystal size and large OPE-n chain length, a back-transfer event is plausible (Figure 5.8, path F). In this case, an excitation originates from either a direct photoexcitation of the nanocrystal or an excitation transferred from a molecular or low-order excitation. This excitation then transfers from the nanocrystal to the aggregate exciton, whereby the aggregate exciton annihilates. This leads to the aggregate exciton as the lowest energy trap for these composite materials, but since nanocrystal disruption of long-range ordering among OPE-n ligands produces a very small population of aggregates, these aggregate states can be thought of as low energy trap centers[106]. A plausible case exists where the aggregate exciton migrates from aggregate domain to aggregate domain, but this event is unlikely since the aggregate domains in these assemblies are expected to be well separated.

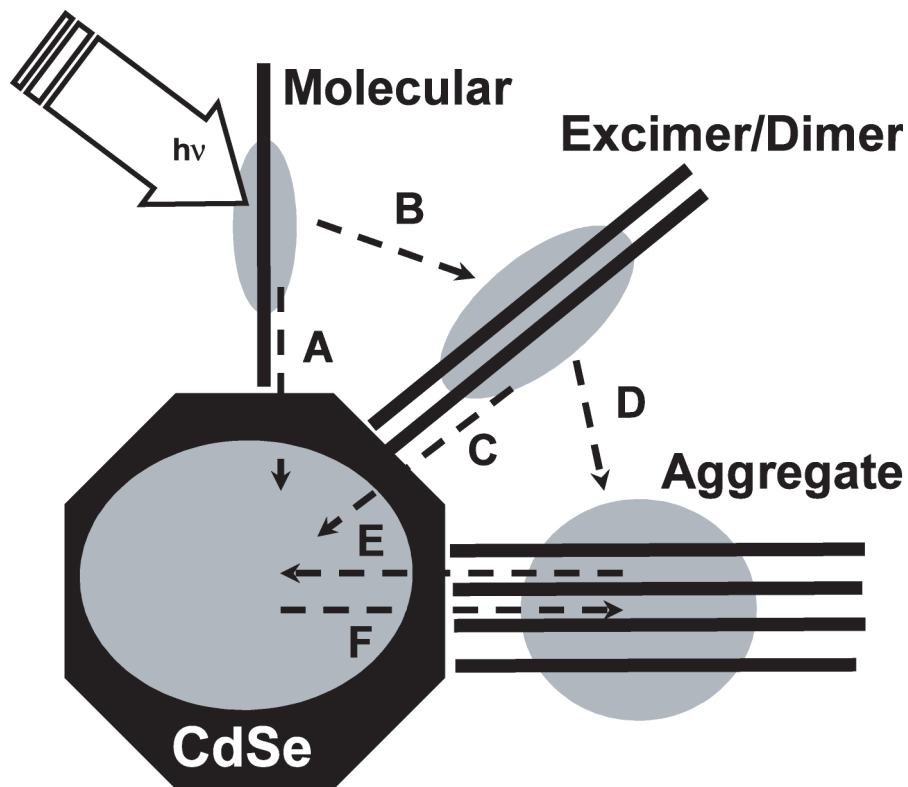


Figure 5.8. Excitation is generated as a molecular exciton which then can migrate to a dimer, delocalize into an excimer or polaron-pair, B, or delocalizes/migrates to an aggregate exciton, D. All three species, molecular exciton, excimer/dimer, and aggregate can transfer energy to the nanocrystal (A,C,E). F is the back-transfer of energy from the nanocrystal to the aggregate.

## 5.5.4 Chapter Summary

Continuous-wave PL studies show that the phenomenon of quantum confinement can be exploited to control energy transfer in inorganic-organic composites by the tuning of resonant interactions, which presumably occur through weak electromagnetic coupling. We show that there is a strong absorption of photon energy by OPE-n followed by a rapid energy injection to CdSe resulting in strong nanocrystal luminescence, the rate of which can be controlled by adjusting the nanocrystal size, which in turn adjusts the resonant interaction of the two. Calculations for this resonant interaction manifested in the spectral overlap integral,  $\langle J \rangle$ , further verifies this. Moreover, the preferential quenching of different polymer configurations implies a strong dependence of the energy transfer on the delocalization of the OPE-n exciton, and that discrete quantum confined nanocrystal states interact with the delocalized excitation. The next chapter is devoted to the time-resolved studies that explore this interaction of delocalized OPE-n excitons and nanocrystal excitons further.

# **Chapter 6**

## **Time-resolved Size-dependent Energy Transfer in Quantum Dot/Molecular Wire Assemblies**

### **6.1 Introduction**

The emergent properties of hybrid inorganic-organic nanomaterials for optoelectronic technologies are dictated by the energetics and orbital interactions of the two systems. Specifically, in the case where the organic and inorganic components are electronically or electromagnetically coupled, probing the time-dependent excited state lifetime measurements can provide important insight into the correlated physics of this hybrid material. In a previous chapter, we showed how resonant interactions between an organic oligomer and CdSe QDs was strongly dependent on CdSe size and oligomer chain length

due to enhanced spectral overlap[107]. In this chapter, we demonstrate how time-resolved studies can reveal a more detailed view of the energy transfer and migration inherent in this hybrid material.

The material being studied is a tightly bound hybrid assembly that forms into large (millimeter-wide) hybrid composites, consisting of oligo-phenylene-ethynylene (OPE-1) units that are coupled through sulfhydryl linkages directly to the CdSe quantum dot surface[107]. The OPE-1 is the interconnecting material that holds the CdSe QDs in place, in a “brick and mortar” motif. The replacement of different CdSe sizes allows for a systematic study on how CdSe size (and consequently exciton energy) plays a role in the flow of electronic energy in this hybrid system. While it is beneficial to consider the two components as possessing only two excited states that participate in the kinetics, it is known that hybrid excited states arising from  $\pi$ -stacking[99, 91, 90] within the solid-state organic matrix form easily and participate in the energy transfer process.  $\pi$ -stacked dimer states, aggregate states, and polaron pairs are some of the known excited states that dominate organic oligomer and polymer solid-state matrices.

Previously, we studied the effects of the CdSe size-dependence and the OPE-n chain length dependence on the excited state properties and energy migration, which has allowed us to choose a model subset from those studies to focus on the energy transfer kinetics. A key feature of the chain length and sizes we have chosen is that the dominant energy transfer process will occur from the OPE-1 dimer state to the CdSe exciton. This is achieved primarily through control of the resonance spectral overlap of the OPE-1 dimer state and

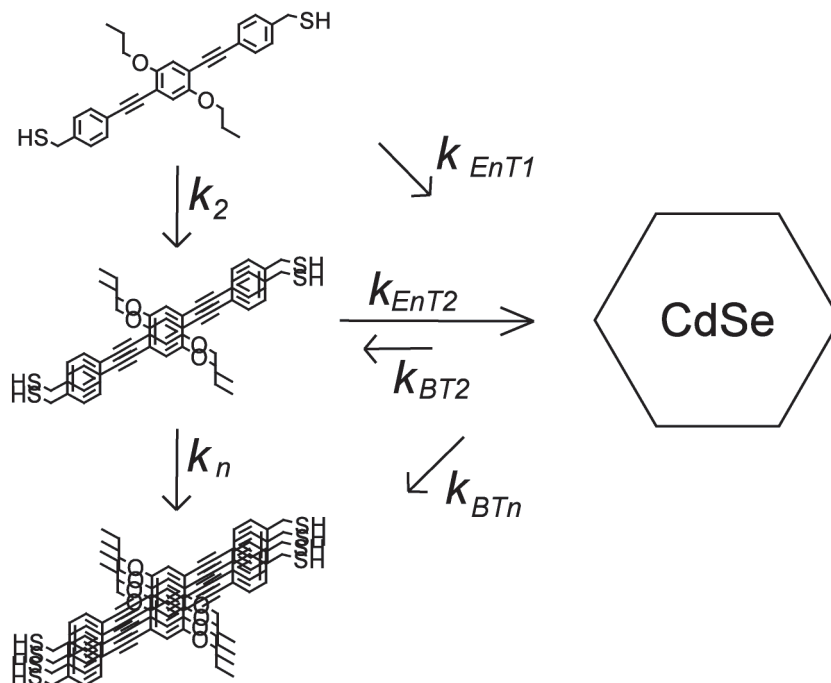


Figure 6.1. Diagram of all possible energy transfer pathways.  $k_2$ :migration from single to dimer,  $k_n$ :migration from dimer to aggregate,  $k_{EnT1}$ :transfer from single to CdSe,  $k_{EnT2}$ :transfer from dimer to CdSe,  $k_{BT2}$ :back transfer from CdSe to dimer,  $k_{BTn}$ :back transfer from CdSe to aggregate

the first CdSe exciton. This greatly simplifies the possible migration pathways, allowing us to use simple kinetic expressions.

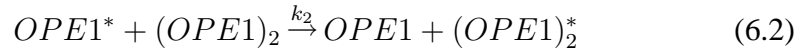
### 6.1.1 Energy Migration Pathways

Fig. 6.1 shows all the possible pathways for the migration of the excitation energy in the system we are studying. From these pathways, we now highlight the important or dominant processes. The diagram includes migration among OPE-1 excited state species as well as back-transfer pathways between CdSe and OPE-1. The excitation begins at the OPE-1 monomer since this excited

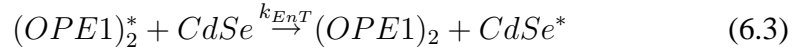
state is resonant with the excitation source and is more abundant than CdSe.



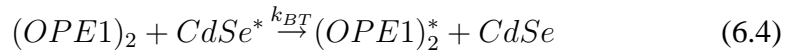
Energy transfer directly from the OPE-1 excited state directly to the CdSe is an unfavorable process since no strong overlap exists between the OPE1 energy and the lowest energy excitons of CdSe. The excitation then migrates to a resonant dimer state,  $(OPE-1)_2$ , the ground state of which is expected to be the dominant species in the assembly due to the close packing interactions.



The dominant energy transfer process in this system then results from the dimer state to the CdSe due to the strongest overlap with the CdSe exciton.



However, this strong resonance can also lead to back-transfer from CdSe to the dimer state.



The excitation eventually leads to many oligomer aggregate states, which are the lowest energy species in the system. In the system we are dealing with, this process should be of only minor importance.

Focusing on the primary energy transfer process in Eq. 6.3 with an associated back-transfer in Eq. 6.4, we can write out the differential equations for this completely as

$$\frac{d[(OPE1)_2^*]}{dt} = - \left( \frac{1}{\tau_{(OPE1)_2^*}} + k_{EnT} \right) [(OPE1)_2^*] + k_{BT}[CdSe^*] \quad (6.5)$$

$$\frac{d[CdSe^*]}{dt} = - \left( \frac{1}{\tau_{CdSe^*}} + k_{BT} \right) [CdSe^*] + k_{EnT}[(OPE1)_2^*] \quad (6.6)$$

This system corresponds to two coupled first-order homogeneous differential equations. We choose the following assumptions to be our boundary conditions for: at the moment of excitation ( $t = 0$ ), the excited  $(OPE1)_2$  population will be  $[(OPE1)_2^*]_0$  and the excited CdSe population will be zero.

The solution[48] for this is, and for our system, the donor and acceptor decays can be written as:

$$[(OPE1)_2^*](t) = [(OPE1)_2^*]_0 \left( \frac{X - 1/\tau_2}{1/\tau_1 - 1/\tau_2} e^{-t/\tau_2} - \frac{X - 1/\tau_1}{1/\tau_1 - 1/\tau_2} e^{-t/\tau_1} \right) \quad (6.7)$$

$$[CdSe^*](t) = \frac{[(OPE1)_2^*]_0 k_{EnT}}{1/\tau_1 - 1/\tau_2} (e^{-t/\tau_2} - e^{-t/\tau_1}) \quad (6.8)$$

where

$$\frac{1}{\tau_1} = \frac{1}{2} \left[ (X + Y) + \sqrt{(X - Y)^2 + 4k_{EnT}k_{BT}} \right] \quad (6.9)$$



$$\frac{1}{\tau_2} = \frac{1}{2} \left[ (X + Y) - \sqrt{(X - Y)^2 + 4k_{EnT}k_{BT}} \right] \quad (6.10)$$

and  $X = 1/\tau_{(OPE1)_2^*} + k_{EnT}$  and  $Y = 1/\tau_{CdSe^*} + k_{BT}$ .  $\tau_{(OPE1)_2^*}$  and  $\tau_{CdSe^*}$  are the native donor and acceptor lifetimes, respectively. In general, we expect to observe a bi-exponential lifetime decay for the  $(OPE1)_2^*$  species and a rising exponential coupled with a decaying exponential decay for  $CdSe^*$ . As seen from Eq. 6.9, the lifetimes obtained are nonlinear combinations of the decay times as well as the energy transfer and back-transfer rates.

In the limiting case where energy transfer is irreversible and no back transfer can occur such that  $k_{BT} = 0$ ,  $1/\tau_1 = 1/\tau_{(OPE1)_2^*} + k_{EnT}$  and  $\tau_2 = \tau_{CdSe^*}$ . It turns out that this approximation allows us to write a condition that directly assesses if back-transfer is involved. This condition arises from examining the equality,  $1/\tau_1 = 1/\tau_{(OPE1)_2^*} + k_{EnT}$ , wherein  $\tau_1$  and  $\tau_{(OPE1)_2^*}$  are directly measured. In order to obtain a non-negative value for the energy transfer rate,  $\tau_1$  cannot be larger than,  $\tau_{(OPE1)_2^*}$ . Therefore, back-transfer occurs if  $\tau_{(OPE1)_2^*} < \tau_1$ .

In addition, the exciton decay of the CdSe QD has been shown to be very complicated and can be strongly influenced by the QD surface. While CdSe possesses an intrinsic native lifetime ( $\sim 20ns$  under ambient conditions), photo-induced charging often leads to non-exponential decays stemming from charged photoluminescence.

As our results and interpretation show, the electronic excitation energy in this hybrid system relies on a resonance condition that is strongly dependent

on the CdSe QD size. Over the CdSe sizes studied, it is the energetic resonance between the CdSe exciton and the OPE-1 dimer-like excited state that strongly dominates the decay kinetics of the final assembly. When this resonance condition is enhanced, energy flows rapidly from the organic oligomer matrix to the CdSe QD. In addition, significant back-transfer also occurs, producing an average repopulation time in the range of a few nanoseconds. Given the strong resonance, and the significantly longer acceptor lifetimes compared to the donor, this back-transfer is expected, due primarily to a thermally stimulated repopulation of donor states.

## 6.2 Experiment

OPE-1 and CdSe QDs coated with TOP/TOPO (tri-octyl phosphine/tri-octyl phosphine oxide) were synthesized using literature methods. The formation of the CdSe-OPE-1 assembly was achieved by slow addition of CdSe to a solution of OPE-1, which was then allowed to assemble overnight before the resultant solid precipitate was washed to remove excess OPE-1. The assembly, which was hundreds of microns wide, was then deposited onto quartz substrates for lifetime measurements. Control experiment preparations consisted of CdSe in nM concentrations dissolved in n-hexane or toluene and a thiol-protected form of OPE-1 (called OPE-1p) in a chloroform or toluene solution or as a thickly deposited solid.

The lifetime measurements were performed using a Hamamatsu streak camera coupled to a CCD for detection and a Nd:YAG-pumped R6G dye laser fre-

quency doubled line (315nm, 10 ps, 1MHz). The advantage of using a streak camera for time-resolved measurements is that it allows us to track the evolution of the PL spectra over the course of the decay. To alleviate the uncertainties in interpreting our data, we use a hybrid Maximum Entropy Method (MEM) to procure the unbiased assignment of lifetime distribution from the PL decay.

### 6.3 Results

In order to understand the interaction between OPE-1 and CdSe, it is important to understand the time-dependent decay of OPE-1 in the solid state. Fig. 6.2 shows the decay profile of OPE-1p in a dilute chloroform solution and cast as a solid film. OPE-1p in solution has a lifetime of 1.4ns, however, casting OPE-1p in a solid converts the exponential lifetime into nonexponential kinetics.

Examining the PL profile (Fig. 6.2 inset) between these two states also reveals a strong overall red-shift in the PL by  $\sim 0.3\text{eV}$  arising from solid-state packing effects. Over the course of the evolution of the film PL, we also note changes in the spectral profile, such that the blue edge of the PL band decreases faster than the red edge of the PL band, as shown in Fig. 6.2(inset), indicative of multiple-excited states.

Fig. 6.3 shows the PL and time-resolved decays of the CdSe QDs used in this study in a dilute toluene solution. With increasing size, the exciton PL band shifts to lower energy and decreases in PL quantum efficiency. The lifetimes of all the sizes studied persist for tens of nanoseconds and exhibit complex

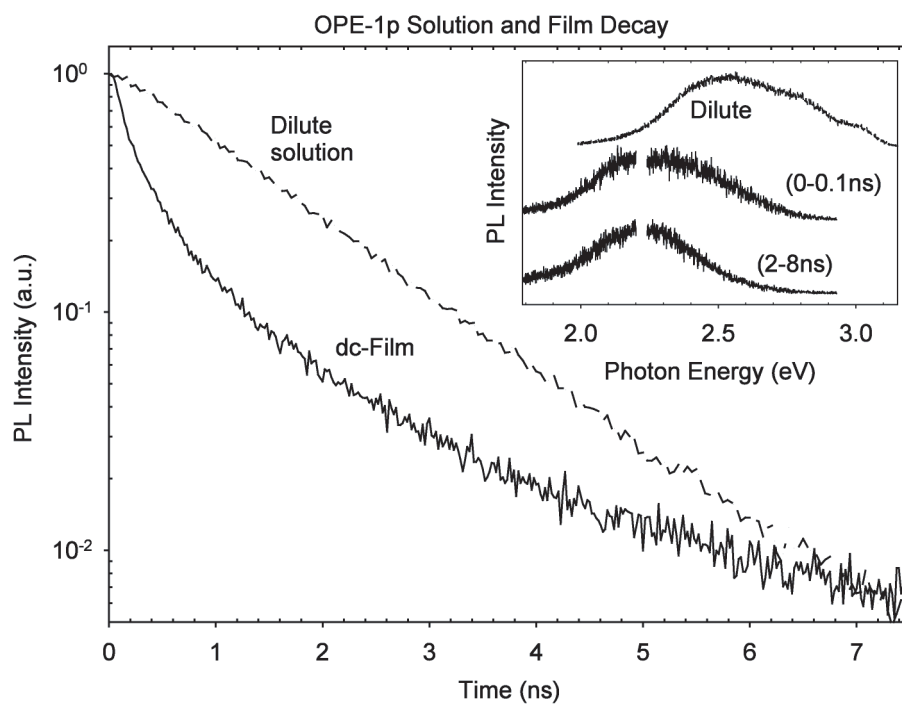


Figure 6.2. Time-resolved PL decay of OPE-1p in a dilute toluene solution (dashed line) and as a drop-cast film (solid line). Inset: Transient PL spectra of OPE-1p film in 2 time regimes (0-100ps and 2-8ns) and OPE-1p dissolved in toluene.

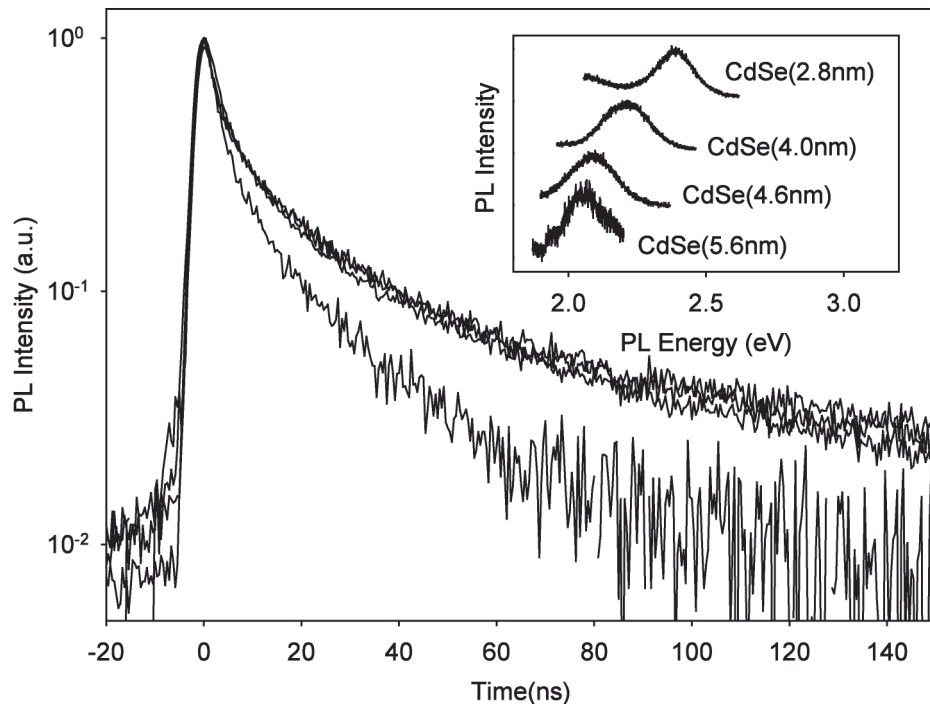


Figure 6.3. Time-resolved PL decay of CdSe QDs of sizes 2.8nm, 4.0nm, 4.6nm and 5.6nm shown in descending order. The corresponding total PL spectra taken from the time-resolved experiment are shown in the inset

decay kinetics. In addition, there is a noticeable reduction in the lifetime of the largest CdSe size studied (5.6nm), though the overall decay still remains on the scale of several nanoseconds. The nonexponential nature of the CdSe decays are a strong function of surface quality, and may contribute to extrinsic short timescale processes. It is generally accepted that the long timescale kinetics reflect single-excitation band-edge exciton decays.

Fig. 6.4 and 6.5 shows the PL and time-resolved decays of the assemblies created with OPE-1 and CdSe of varying sizes. As can be seen in Fig. 6.4, the observed lifetime decays are on the order of a few nanoseconds and bear more resemblance to the OPE-1p component rather than the CdSe component.

Therefore, the decay kinetics of both assemblies containing small CdSe sizes are strongly dominated by the organic matrix. Photon energy is absorbed primarily by the organic counterpart and decays within this component with no energy transfer communication occurring between the two phases. More evidence of this lack of communication is present in the transient PL, wherein the spectra (Fig. 6.4 inset) closely resembles the OPE-1 film spectra over the course of the entire decay. A small variation in the transient PL is found in CdSe(4.0nm) shows that the short-lived OPE-1p component decays faster, which may be indicative of a weak size-dependent effect. In both cases, there seems to be little evidence of CdSe PL, which would have manifested itself as significantly longer lifetimes in the time-resolved decays or sharp overlapping peaks in the transient PL.

Fig. 6.5 shows the time-resolved decays and transient PL for the assemblies of the two largest CdSe sizes we studied. The spectral range was limited to the region where CdSe of the appropriate size was known to emit. The decay observed is more complicated than the smaller CdSe sizes and an abrupt change in the decay time at short timescales is observed. In addition, the decay time magnitude is tenfold longer than the assemblies containing smaller QD sizes and the transient PL (shown in the insets) shows more QD PL than OPE-1 PL. Given these observations in both the time-resolved decay and the transient PL, it is evident that the inorganic QD component dominates the decay kinetics when large CdSe sizes are used.

This abrupt change in slope at short timescales is likely to be due to a re-population of the CdSe emitting state that overlaps with normal CdSe decay. To

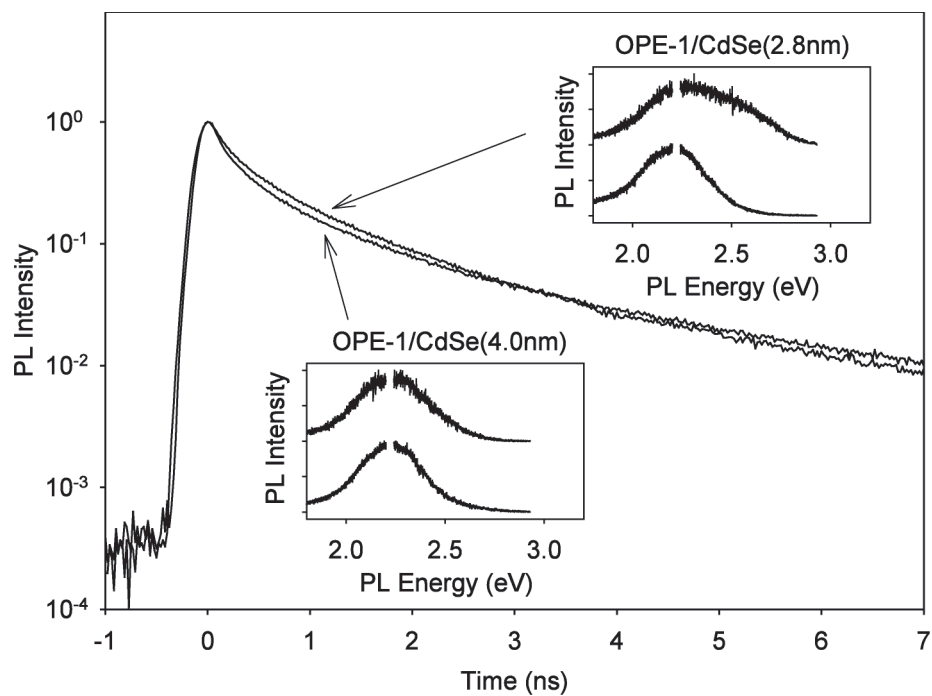


Figure 6.4. Time-resolved PL decay of OPE-1/CdSe assemblies containing CdSe QDs with diameters of 2.8nm and 4.0nm. Insets show the transient PL spectra for the decays in 2 time regimes (0-100ps and 2-8ns)

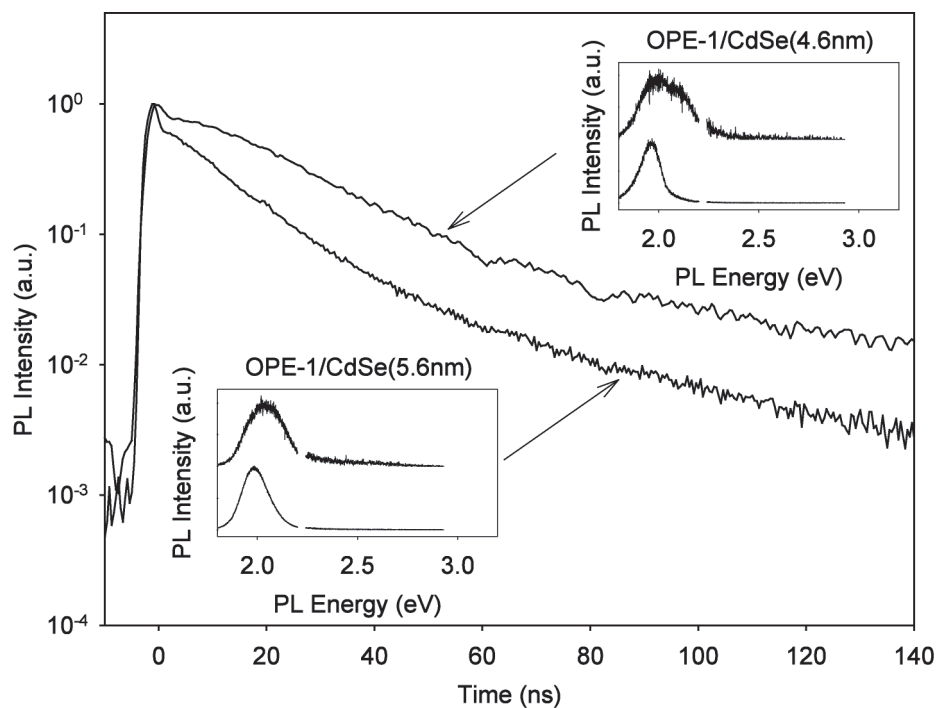


Figure 6.5. Time-resolved PL decay of OPE-1/CdSe assemblies containing CdSe QDs with diameters of 4.6nm and 5.6nm. Insets show the transient PL spectra for the decays in 2 time regimes (0-1ns and 2-140ns)



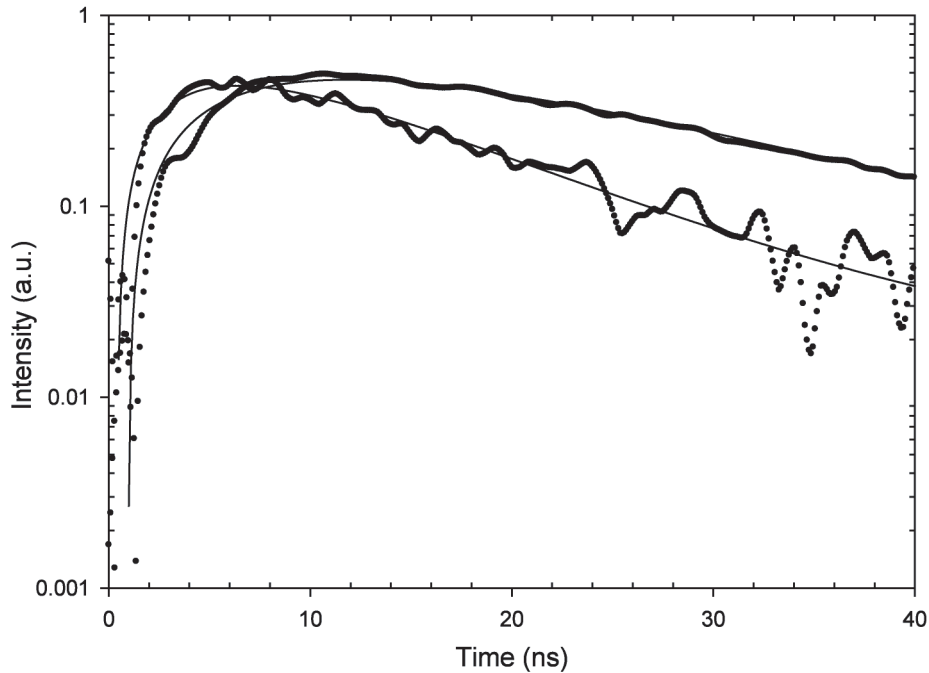


Figure 6.6. Time-resolved decays of OPE-1/CdSe assemblies containing CdSe(4.6nm) and CdSe(5.6nm) wherein the contribution from directly pumped QD PI has been subtracted from the decays. Solid lines indicate fits to a function containing an exponential rise and decay

examine this phenomenon, the native CdSe decay times were subtracted from the assembly decays. We can clearly see the rollover in the CdSe decay time in Fig. 6.6, which represents the population of unexcited QDs which received energy from the OPE-1 matrix. Between the two curves it is evident that the larger QD assembly has a faster population time than the smaller QD assembly, as well as a faster decay time than the smaller assembly.

The kinetics in Fig. 6.6 fit very well to the sum of a single decaying and a single rising exponential,  $f(t) = xexp^{-t/\tau_1} - (1 - x)exp^{-t/\tau_2}$ . The rising exponential decay lifetime is 8.5ns in the assembly containing CdSe(4.6nm) and 3.5ns in the one having CdSe(5.6nm). In both cases, the pre-exponential

factors were nearly identical ( $x \sim 0.5$ ). The decay times, which are expected to be influenced more heavily by the native lifetime of the CdSe acceptor instead of energy transfer, have dropped from 13.6ns to 9.9ns as the CdSe size is increased from 4.6nm to 5.6nm. This is an expected result as the native lifetime of CdSe decreases with increasing size.

As an additional tool for examining the kinetics, the lifetime distributions were extracted from the decay kinetics using a hybrid Maximum Entropy Method / Nonlinear Least Squares method. Fig. 6.7 shows the lifetime distribution for some of the samples studied. The lifetimes from the assemblies of two different sizes as well as the individual components are shown. This fitting procedure accounts for both rising and decaying exponential kinetics.

## 6.4 Discussion

Comparing this limiting case to our data, we see that the rise time we observe should correlate directly to  $\tau_1$ . However, the rise time that we obtain empirically is longer than the lifetime of the OPE-1 donor, which cannot be true if this limiting case of this kinetic model were true. Therefore, the only way for the rise time to be longer than the donor decay time is if back-transfer is introduced ( $k_{BT} \neq 0$ )

The addition of a back-transfer rate produces no simple solution to the kinetic equation. The observed rise time therefore represents components resulting from the donor decay time that is accelerated by the transfer of population via energy transfer to the acceptor and impeded by the back transfer of popu-

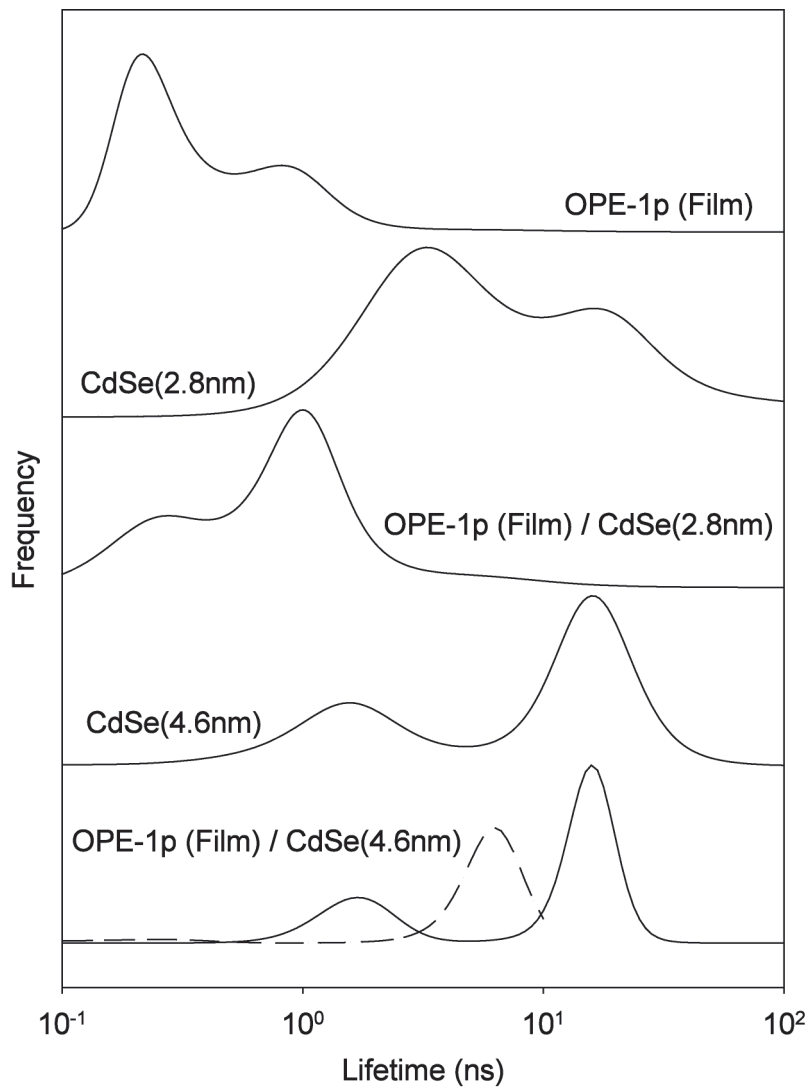


Figure 6.7. MEM-NLS analysis of lifetime distributions (from top to bottom) for an OPE-1 drop-cast film, CdSe(2.8nm)/toluene, an assembly of CdSe(2.8nm)-OPE-1, CdSe(4.6nm)/toluene and an assembly of CdSe(2.8nm)-OPE-1. The solid lines indicate decaying exponential distributions while the dashed line indicates rising exponential distributions.

lation from the acceptor to the donor. This complicated kinetic result obscures the quantitative energy transfer rate, although qualitative conclusions can still be made regarding trends in the kinetics with regard to the differences in CdSe size.

Taking into account the relative PL contribution of the acceptor/ donor (CdSe/ OPE1) over the entire time decay, we note that assemblies containing larger CdSe sizes (above roughly 4nm) favor a strong CdSe PL over OPE1 PL. In fact, we have obtained a null result with 2.8nm CdSe wherein CdSe not only fails to affect the kinetics, but fails even at producing detectable PL. As a result, direct excitation followed by resulting PL of CdSe does not appear to be a favored pathway. Therefore that leaves energy transfer as the primary mechanism through which CdSe is excited. The electronic energy absorbed by the OPE-1 matrix is slowly transferred to CdSe, resulting primarily in the effect of a rise time in the CdSe PL decay kinetics. However, this rise rate is artificially slowed down by the back-transfer rate.

Comparison of this result to the MEM-NLS data shows that the rising lifetime obtained in the above fitting matches the rising distribution in the MEM-NLS Fit. A MEM-NLS fit could not be performed for the CdSe(5.6nm) QD, since there were too few data points within the temporal region of the rise to extract the rising time accurately. As can be seen from Fig. 6.7, the decay distributions of the OPE-1 matrix are very short ( $< 2ns$ ) and possess 2 distinct distributions that result from the complex nature of their decay in the solid state. The change in the transient PL decay for OPE-1 is linked to these two distributions and we can assign the shorter lifetime to the blue edge of the emis-

sion band and the longer lifetime distribution to the red edge of the emission manifold. These kinetics arise most likely from the formation of distinct  $\pi$ -stacked excited state dimers. These dimer-like transitions are red-shifted from the native molecular PL.

CdSe possesses two distinct lifetime distributions, ( $> 2ns$ ) that do not vary greatly as a function of size, as can be seen in both the transient decay, Fig. 6.3, and the MEM-NLS fits, Fig. 6.7. However, the assemblies containing differing CdSe sizes produces drastically different lifetime distributions. In the case of smaller CdSe(2.8nm), the OPE-1 lifetimes are obtained, although at different ratios than the film counterpart, with very little evidence of the longer CdSe lifetimes. This is strongly indicative of a case where OPE-1p is the primary absorbing and emitting species, and no energy transfer occurs to the nanomaterial. The change in the lifetime distribution is most likely due to a different OPE-1 packing morphology, induced by binding to the CdSe surface.

In the case of larger CdSe(4.6nm), the assembled structure displays not only decay pathways, but also rising exponential kinetics. As shown in Fig. 6.7, two decaying (solid lines) and one rising (dashed line) exponentials are obtained. While the decaying exponentials seem to be derived from components from the native OPE-1 and CdSe lifetimes, the rising exponential lifetime is found only in this assembly, and only for larger CdSe sizes. This rising exponential lifetime more than likely occurs due primarily to an energy transfer process from the OPE-1 component to the CdSe component, and is representative of the repopulation rate of the energy acceptor.

While the effect of CdSe size is readily apparent from the MEM-NLS anal-

ysis, which shows that the threshold for energy transfer to proceed is in the neighborhood of 4.0-4.6nm, it is also worthwhile to assess if energy transfer is accelerated beyond this threshold. Since MEM-NLS could not extract the lifetime distributions from CdSe(5.6nm), we compare the time decays of 4.6nm and 5.6nm with the direct-pump CdSe PL subtracted from it. What remains is the kinetics of the unexcited CdSe population that becomes repopulated due to energy transfer from the OPE-1 matrix and which consequently decays as PL from CdSe. The kinetics obtained are shown in Fig. 6.6, which have been fit to a rising and decaying exponential for quantitative results. Examining Fig. 6.6, we see that the rise rate of the larger CdSe(5.6nm) is greater than the smaller CdSe(4.6nm) as evidenced qualitatively in the steeper positive slope and quantitatively in the shorter rise time of 3.5ns vs. 8.5ns. The difference in the decay times obtained is strongly influenced by the differences in the native size-dependent CdSe decays, shown in Fig. 6.3, wherein CdSe(5.6nm) has a naturally shorter decay process than the smaller CdSe sizes.

Although in Fig. 6.6 we have used temporal subtraction of the native CdSe lifetime to simplify our analysis, we cannot attribute this to purely directly-pumped PL. The reasoning behind this is that when one considers the entire study as a whole, the control experiments indicate that CdSe exciton energy and kinetics changes gradually and systematically as a function of size. Absorption cross-sections also follow this trend, and no large jump is expected between CdSe(4.0nm) and CdSe(4.6nm). In contrast, the kinetics of the larger assemblies indicate a combination of decays that originate spectrally from CdSe QDs, but have components that show rapid (on the order of the excitation pulse) and

slow (energy transfer with back transfer, as explained above) excitations. While the rapid excitation can be argued to result from directly pumped PL, this is inconsistent when one considers that assemblies containing slightly smaller CdSe do not show any directly-pumped PL. An explanation that is more consistent with the data is that a second, faster size-dependent energy transfer process occurs from the OPE-1p matrix to the CdSe component. This fast energy transfer process would be comparable in time to the pulse distortion ( $< 1\text{ns}$ ), and would stem from the participation of molecular OPE-1 in the energy transfer process to CdSe.

## **6.5 Chapter Summary**

Performing transient PL studies on OPE-1/CdSe assemblies has allowed us to elucidate some of the complex processes that lead to energy transfer and migration as they pertain to CdSe size. The large sensitivity in the kinetics of this assembly on CdSe size makes this a model material for the study of the flow of electronic energy in multi-phase hybrid systems containing a quantum-confined component.

## **Chapter 7**

# **Photothermal Melting and Energy Migration of Quantum-Dot-doped Organic Oligomer Films**

Reproduced with permission from “Photothermal Melting and Energy Migration in Conjugated Oligomer Films with CdSe Quantum Dots,” A. Javier, R.W. Meulenberg, C.S. Yun, G.F. Strouse, *Journal of Physical Chemistry, B.*, (2005), 109, 6999-7006. Copyright 2003, American Chemical Society

### **7.1 Introduction**

The combination of the rapid processability of conducting polymers[98, 108, 109, 89] with the tunability of semiconductor quantum dots[4, 110, 1] makes the hybridization[111, 102, 83] of these two materials a potential can-



didate for device-oriented designs[81, 112, 113], most notably electro-optical memory. Such unconventional design approaches can ideally lead to hybrid systems that benefit from the strengths of both materials, without suffering from the weaknesses of the precursors. The challenges in this field entail overcoming the strong electrical and optical induced charging[32, 114] of the quantum dots which reduces the quantum yield and therefore the overall performance of the material. Such a challenge can be overcome by employing alternate means of addressing and manipulating the quantum dot such as using resonant dipolar coupling.

In a previous publication[107] we explored the intimate interaction between a phenylene-ethynylene oligomer and CdSe quantum dots, wherein we were able to observe strong size dependent electronic energy transfer that conferred a high degree of interaction between the two systems. The guiding principle in this system was that control of energetically resonant interactions are tunable through quantum dot size. The intimate conjugation between the two systems produced a rigidly bound monolith, whose optical characteristics remained extremely stable. In this manuscript, we report on the study of the unbound variant of this hybrid system, wherein thermodynamic transitions within the oligomeric domains becomes the primary factor for tuning the electronic properties[115]. This system involves a matrix of amorphous oligomer to which quantum dots have been doped in very small quantities ( $< 1\%$ ). Bulk thermodynamic transitions from the oligomer matrix (energy transfer donor) are thus optically detected using the dopant (energy transfer acceptor) PL. Specifically, the films are initially formed in a thermodynamically

metastable phase or glassy state. Direct heating of the film in this amorphous metastable state melts the structure which is followed by a non-reversible transition to a more thermodynamically stable, crystalline phase. The dopants introduced into this matrix do not affect the overall conformation, but act only as optical reporters of the phase transition. Indirect heating by optical means can be achieved and is exploited for using this material in a read-write manner. This demonstration not only underscores the importance of this material as a new optical material, but highlights its potential use as a medium for optically addressable and readable memory.

Electronic energy transfer[73, 116], a nonradiative process where electronic energy is transferred from an electronically excited energy donor to an acceptor moiety, is a phenomenon found in condensed phase materials ranging from biological entities to doped semiconductor crystals[75, 117]. In the latter case, typically the host matrix acts as the energy donor, and the dopant material acts as the energy acceptor. Optical or electrical excitation of the host material can result in efficient dopant photoluminescence as the host's pseudo-particles (excitons, phonons etc..) act as conduits in the transfer of that energy. While this case generally represents coherent energy transfer, it is important to recognize that in amorphous films, energy transfer still occurs via resonant energy migration[118] wherein the energy moves from domain to domain within the host in a random-walk pattern until it reaches the energy acceptor[119]. The rate of this energy diffusion will be strongly dependent on the general conformation and local domain interactions of the host material[120], as well as the electronic energy topography.

Quantum confinement produces size-dependent electron and hole energy levels for CdSe in a size regime between  $\sim 1$ -10nm. The resulting size-dependent trend in the exciton energy provides a remarkable tunability for this material to be exploited in both applied and pure science endeavors. In particular, CdSe can be employed both as an energy trap[77] for the migrating excitation in a host-guest system, and as an optical reporter for when the excitation has arrived at the CdSe quantum dot. Were this material to undergo a structural phase transition, the energy diffusion rate would be strongly affected and therefore the dopant photoluminescence may be strongly enhanced or quenched. This suggests tracking changes in energy transfer through a reporter entity can provide insight into changes in the host lattice conformation. Although a significant number of studies have been performed using CdSe as the dopant in conjugated polymer matrices, to the authors' knowledge, this manuscript reports the first attempt at the use of CdSe QDs as dopants in an oligomer matrix.

While poly-phenylene-ethynylene (PPE) and poly-phenylene-vinylene (PPV) systems have been well-characterized[98, 121], significantly less is known about their oligomeric[122] variants, OPE and OPV. In particular, both theoretical and experimental studies have indicated that the photophysics of conjugated polymers change drastically in the limit of low repeat units, namely oligomers[99]. These short conjugated systems represent the crossover regime between solid-state phenomena[103] and molecular-like excited states. In fact, exciton lengths are not reached until roughly  $30\text{\AA}$ (in the region of more than 5-8 repeat units)[87] in the oligomeric assemblies. In addition, due to the low repeat units, intra-chain transport[123] (parallel to the long axis) is not as dom-

inant and inter-chain energy migration (perpendicular to the long axis) can be strongly favored in these systems. For example, in anthracene matrices, energy migration proceeds by inter-ring transfer with triplet exciton diffusion lengths exceeding  $10\mu\text{m}$ [124]. Ordered PPE films[120] have shown diffusion lengths of up to 10nm. Thermodynamically, since each oligomer has only a few repeat units, their solid state phases are much less thermodynamically stable than their polymeric counterparts owing to fewer inter-chain interactions (co-facial ring stacking and side chain associations) that confer stability[125, 123, 126]. This produces a competition between kinetically favored and thermodynamically favored solid-state phases, wherein kinetically favored but thermodynamically metastable glass states can easily form during the process of film deposition.

This paper is organized as follows: 1) We discuss phase transitions in the oligo-p-phenylene-ethynylene dibenzylthioacetate (OPE-1p) matrix, 2) we show how the optical properties arise from the morphology of the OPE-1p film, 3) we show how the film morphology can be optically manipulated, and 4) we show how CdSe QDs efficiently reports these domain changes and how it can be used for read-write optical memory.

## 7.2 Experimental Details

**Synthesis.** OPE-1p was prepared and purified as described in our previous report[107]. CdSe was prepared with an organic overcoating of HDA (hexadecylamine) as reported previously[4].

**Thin Film preparation.** Solid thin films were prepared in two ways. dc-

Films were made by drop-casting concentrated solutions ( $\sim 1\mu\text{M}$ ) of OPE-1 and/or CdSe QDs in toluene onto sapphire flats and allowed to dry on top of a warm oven. sc-Films were made by spin-casting dilute solutions ( $\sim 1\text{nM}$ ) of OPE-1 and/or CdSe QDs in toluene at slow spinning speeds ( $\sim 10$  monolayers). Doped thin films were prepared in both methods by careful preparation (using  $\mu\text{L}$  syringes) of mixed OPE-1p/CdSe solutions made from stock solutions. In both cases, film thickness was kept optically dilute and transparent ( $< 0.1$  Absorbance at  $\lambda_{exc}$ )

**Differential Scanning Calorimetry.** DSC was performed on 10-12 mg of OPE-1p crystal or on concentrated OPE-1/toluene solutions that were thickly deposited onto the sample pan by drop-casting. Several runs were performed at a ramping speed of  $10^\circ\text{C}/\text{min}$ , and reversibility was tested by repeated cycling.

**UV-Vis Spectroscopy.** Absorbance spectroscopy was performed using a Varian Instruments Uv-Vis spectrometer at room temperature in 1-cm quartz cells for solutions and sapphire flats for thin films. The UV-Vis spectra of doped films and standard solutions showed exclusively OPE-1 absorption, with an undetectable or negligible amount of CdSe present.

**Raman Spectroscopy.** Raman spectra were obtained by front-face sample excitation at 514nm using an  $\text{Ar}^+$  ion laser (Spectra Physics), collection by a f-1 lens and collimation into a 1/2m monochromator (Acton). Laser light rejection was achieved using a super-notch filter.

**Photoluminescence Spectroscopy.** Photoluminescence of solid films was taken using the excitation of either a HeCd laser (325nm) or the filtered 312nm line of a Hg-arc lamp. Samples were placed in a cryostat where a vacuum

of  $10^{-3}$  mm Hg was applied. Heating was achieved resistively through a calibrated heating rod connected to copper rings surrounding the sapphire substrate, producing a temperature range between room temperature to 420K( $\pm$ 5K). In the temperature-dependent experiments, the film was allowed to thermally equilibrate in the dark for at least 10 minutes before being exposed to excitation light. Sample excitation was kept to 2 seconds maximum during these experiments in order to reduce any photo-induced heating.

Front-face excitation was used for the He-Cd system, but 45° rear excitation was used for the Hg arc lamp. The luminescence was collected using a f-1 lens, and collimated to a 1/3-m CVI Spectrometer (150g/mm). Detection was achieved with an air-cooled SBIG CCD (512px x 512px).

## **7.3 Structural Characterization**

### **7.3.1 DSC Analysis**

Inspection of the melting behavior of the OPE-1p films suggest complex liquid-crytalline behavior dependent on the method of preparation (Fig. 7.1). The sample dependent calorimetry seems to arise from subtle packing differences. Such complexity is commonplace in materials that exhibit liquid-crystalline behavior. In the single crystal a strong 1st-order exotherm is observed at 405K (23 J/g), corresponding to a solid-to-liquid (s-l) transition, as found in similar DSC studies on polymeric variants[127]. Just prior to this transition, a small 1st-order solid-to-solid (s-s) transition takes place at 380K

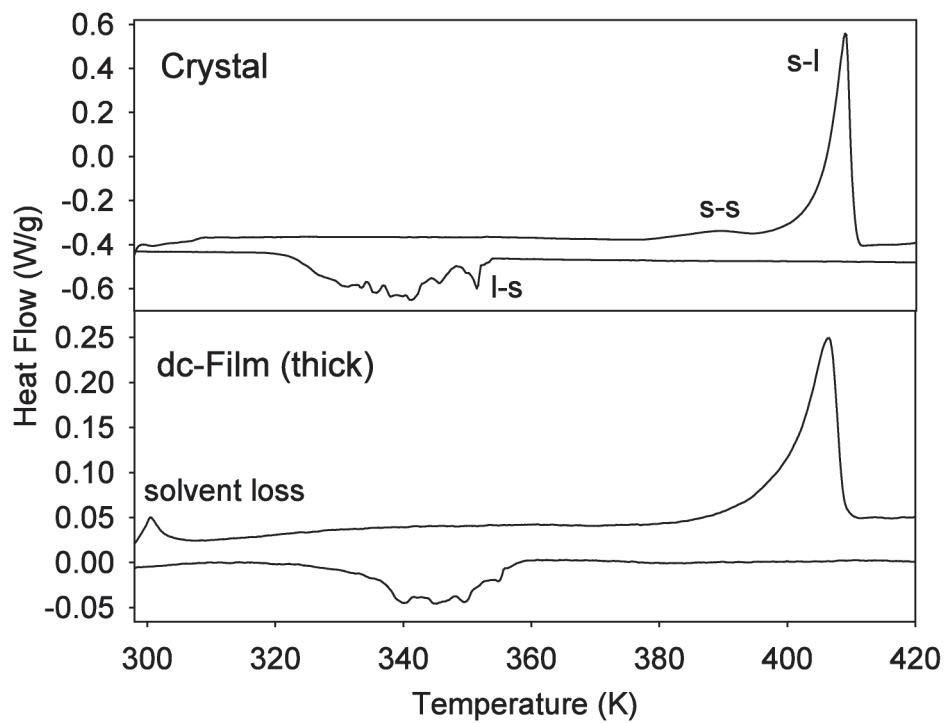


Figure 7.1. Differential Scanning Calorimetry data for OPE-1p in the drop-cast film form (Bottom) and the single crystal form (Top). Features are labelled to indicate the state-state transitions: s-l: solid-to-liquid, s-s: solid-to-solid, l-s: liquid-to-solid.

(5 J/g). The s-s transition indicates the presence of a glassy solid that is accessed before the transition to a completely liquid phase or most likely arises from the melting of the OPE-1p side-chains[128] inducing chain mobility prior to the onset of melting. The glassy solid is reminiscent of liquid crystalline phase transition with the onset of ring mobility. As the material cools from the liquid phase, several small, discrete endothermic transitions (20 J/g) are observed at lower temperatures than the melt at 360K. This behavior is reversible as the crystal is run through several heating and cooling cycles. The cooling behavior differs from what is observed in the polymeric variant, wherein a broadened distribution is found as a result of a distribution of states[127]. In the oligomeric version, since there is a single molecular structure, the discrete transitions must arise from a kinetically-controlled combination of discrete intramolecular (ring twisting) and intermolecular (ring-ring stacking, side-chain packing) interactions, rather than a purely thermodynamic process consistent with the observation of metastable state formation. Comparison of the areas under the DSC curves reveal the process is reversible, just kinetically unfavorable.

The DSC scan of the amorphous drop-cast film (dc-Film) shows a solvent loss peak at 305K which corresponds to the boiling point of toluene, followed by an identical s-l transition (9 J/g), as observed in the crystalline form. However, the transition to the glassy solid is not observed distinctly in the amorphous film. The strong asymmetry of the s-l transition toward lower temperatures indicates the presence of a broadened s-s transition such that the s-s transition occurs over a wider temperature range than the crystal and cannot be



distinguished from the s-l transition. This suggests that the more disordered nature of the glassy dc-film is a kinetically driven process. This is logical in light of the probability of a distribution of states arising from chain disorder in the drop-cast films. Numerical integration of the DSC data reveals that the l-s transition (5 J/g) accounts for 56% of the energy released in the s-l transition. The remaining 44% most likely arises from weak, broad, unresolved peaks.

Assuming that the l-s transitions between the crystal and film to be proportional to each other, the sum of the energy of the s-l and s-s transitions in the crystal accounts for the energy in the s-l transition of the film. Therefore, we can expect drop-cast films to be structurally different from the crystals since the s-s crystalline-glass solid ( $T_g$ ) transition occurs at higher temperatures. The presence of a weak endothermic transition at 385K in the single crystal that moves to higher temperature in the drop-cast film strongly suggests that packing effects play an important role in the thermodynamic phases of the material. The presence of a complicated exothermic transition that does not remotely resemble the corresponding endothermic transition (both in temperature and peak shape) indicates a very complicated cooling cycle that may involve changes in kinetically slow processes arising from local domains in the sample. An important point that we will return to later is that all of these transitions represent reversible macroscopic processes for the average structure, although this does not suggest microscopic reversibility for local domains.

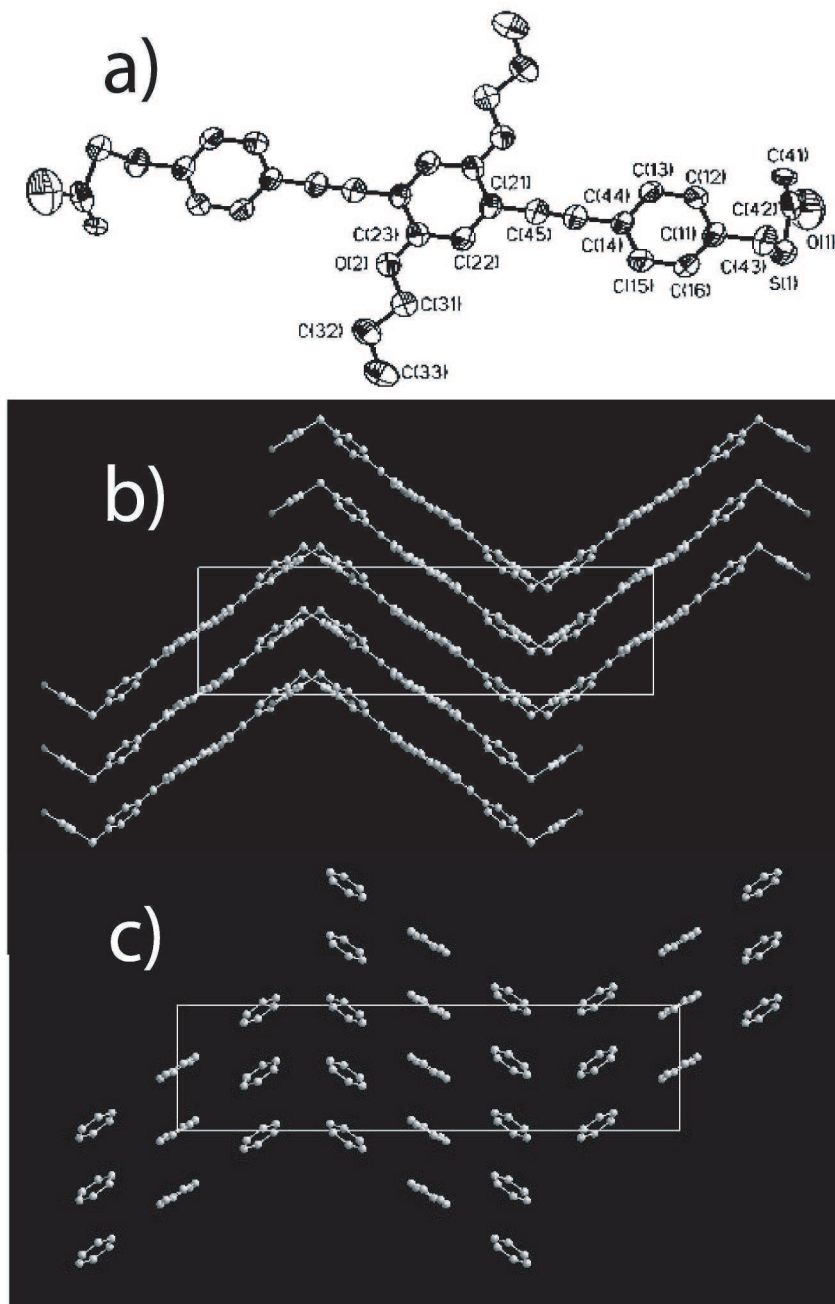


Figure 7.2. XRD Data used to reconstruct the morphology of single crystals of OPE-1p that formed under slow, crystallization. a) shows the electron densities at each atom b) is a 3D representation of the stacking of OPE-1p molecules and c) shows only the phenyl rings to highlight the effect of the interplane twisting within the same molecule.

### 7.3.2 XRD Analysis

XRD Data (Fig. 7.2) on the single crystal reveals an inter-chain separation of approximately  $7\text{\AA}$  as well as a twisted inter-plane geometry, as is expected from the rotationally flexible nature of the intra-molecular triple bonding between alternating phenyl groups. The XRD reveals the strength of the inter-chain  $\pi$ -stacking interactions in distorting the molecular geometry, as the stability afforded by  $\pi$ -stacking interactions causes a deviation in the inter-phenyl groups angle to be greater than zero.

## 7.4 Optical Characterization

### 7.4.1 Raman Analysis

Raman spectroscopy performed on the amorphous film is shown in Fig. 7.3. Only the frequency range of  $1200\text{ cm}^{-1}$  to  $1600\text{ cm}^{-1}$  is shown, as these signals were the strongest and correlate directly to the molecular vibrations. At room temperature, 4 peaks in this frequency range can be clearly identified. The frequencies  $1575\text{ cm}^{-1}$ ,  $1323\text{ cm}^{-1}$  and  $1217\text{ cm}^{-1}$  arise from ring stretches of the aryl moieties [129, 130]. However, the signal at  $1530\text{ cm}^{-1}$  is not a vibration of the OPE-1p molecule, therefore it is suspected that this vibration arises from a symmetry element induced by the crystalline packing. As we study the evolution of these Raman signals as a function of temperature this appears to be the case as it is the  $1530\text{ cm}^{-1}$  that shifts most drastically as the crystal approaches its melting point. Tracking these vibrations as a function of temperature, there

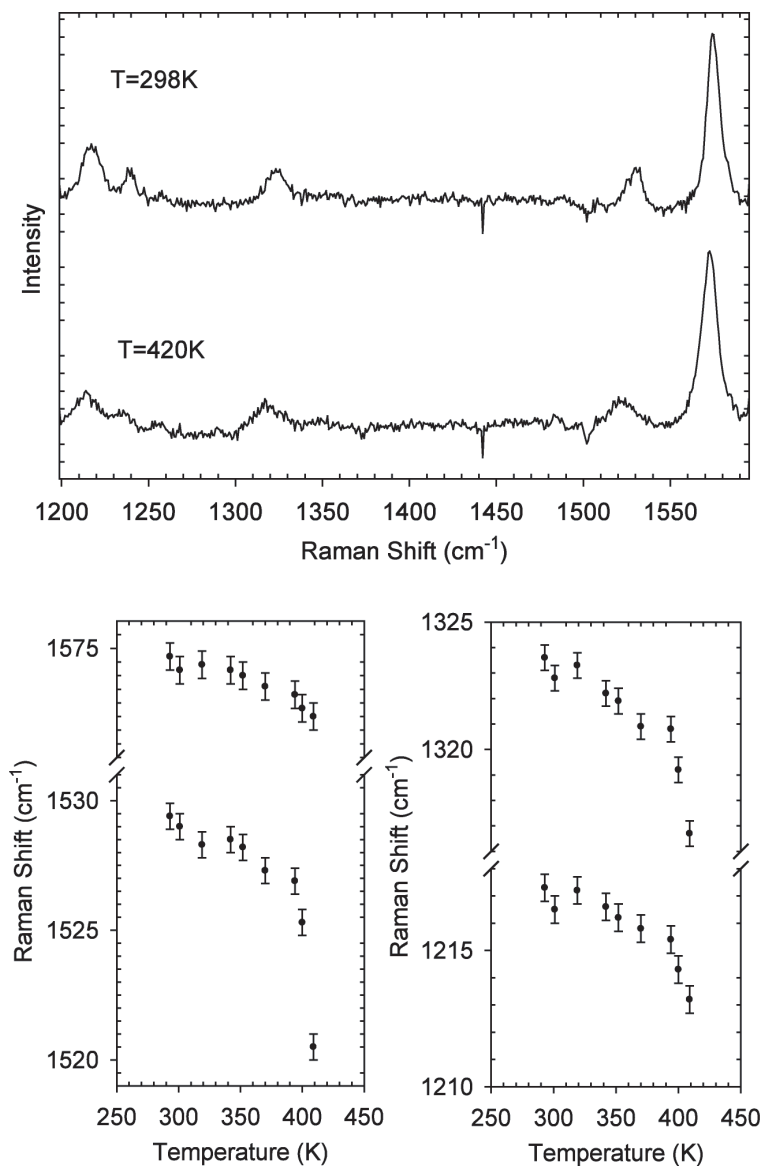


Figure 7.3. Raman Spectroscopy of OPE-1p drop-cast film at different temperatures. Raman Spectra of OPE-1p at 298K (top) and at 420K (bottom). The frequencies of the 4 identified peaks are tracked as a function of temperature (bottom graphs).

is a global shift to lower frequencies that all the observed frequencies show as seen in Fig. 7.3. However, as the melting point of the crystal(407K) is passed, all the raman signals shift strongly to lower frequencies except the 1575  $\text{cm}^{-1}$  mode. This is interpreted as a softening of the crystalline lattice as the melting point is passed.

The 1530  $\text{cm}^{-1}$  mode is not an intrinsic crystal vibration as these tend to be of significantly lower frequency[131]. In addition it would be expected that this mode should disappear as the system approached the isotropic liquid and crystal symmetry is lost. This is not the case as the strength 1530  $\text{cm}^{-1}$  mode remains strong even after the crystal has melted completely.

#### 7.4.2 PL Spectra Fitting Method

Our analysis of the PL properties of OPE-1p begins with a detailed fitting of OPE-1p in a dilute toluene solution ( $\sim 1\text{pM}$ ) using a two-state model accounting for vibronic transitions with 2-D harmonic wells[132],

$$\frac{I(\omega)}{I(\omega_{00})} = \sum_{v_M} \sum_{v_L} \left( \frac{\omega_{00} - v_M \omega_M - v_L \omega_L}{\omega_{00}} \right)^3 \left( \frac{S_M^{v_M}}{v_M!} \right) \left( \frac{S_L^{v_L}}{v_L!} \right) \exp \left[ -4 \ln 2 \left( \frac{\omega - \omega_{00} + v_M \omega_M + v_L \omega_L}{\Delta \omega} \right)^2 \right]$$

where  $v_M$  and  $v_L$  are the ground state vibrational quantum numbers for the medium and low frequency vibrations, respectively, and the sum is over the first

5 of the medium and first 10 of the low frequency numbers. The vibrational frequencies ( $\omega_L, \omega_M$ ), the associated Huang-Rhys factors ( $S_L, S_M$ ) and the excited state displacement energy ( $E_{00}$ ) can also be determined. The line width ( $\Delta\omega$ ) and the PL intensity ( $I(E_{00})$ ) are also fit. The quality of the fit is shown in Fig. 2a in the manuscript. We obtain two frequencies corresponding to resonantly coupled vibrations,  $\omega_L = 351 \pm 3\text{cm}^{-1}$  and  $\omega_M = 1559 \pm 6\text{cm}^{-1}$  and their corresponding Huang Rhys factors  $S_L = 2.8 \pm 0.05$  and  $S_M = 0.96 \pm 0.01$ . The medium frequency mode we obtained matches the strongest signal in our Raman spectrum in Fig.7.3 at  $1570\text{cm}^{-1}$  with less than a 1% difference. This strongly indicates that the excited state decay and even nonradiative pathways relax through ring vibrations.

### 7.4.3 PL Spectra Analysis

Consistent with the expectations from the complex calorimetry data, the PL of OPE-1p films is strongly preparation-dependent; and the initial stock solution concentration and casting method show dramatic changes as shown in Fig. 7.4. This is attributable to the change in population density of various aggregate states trapped by the glassy oligomer structure formed following film casting. In a previous publication[107], we used concentration dependent absorbance and photoluminescence to demonstrate the evolution of the OPE-1p molecules into dimer-like and aggregate configurations arising from strong  $\pi - \pi$  stacking driving forces. In solution, both molecular and dimer PL can be observed, mediated by the self-association equilibrium. The monomer spectrum dominates Fig. 7.4a. The dimer PL can be predicted from

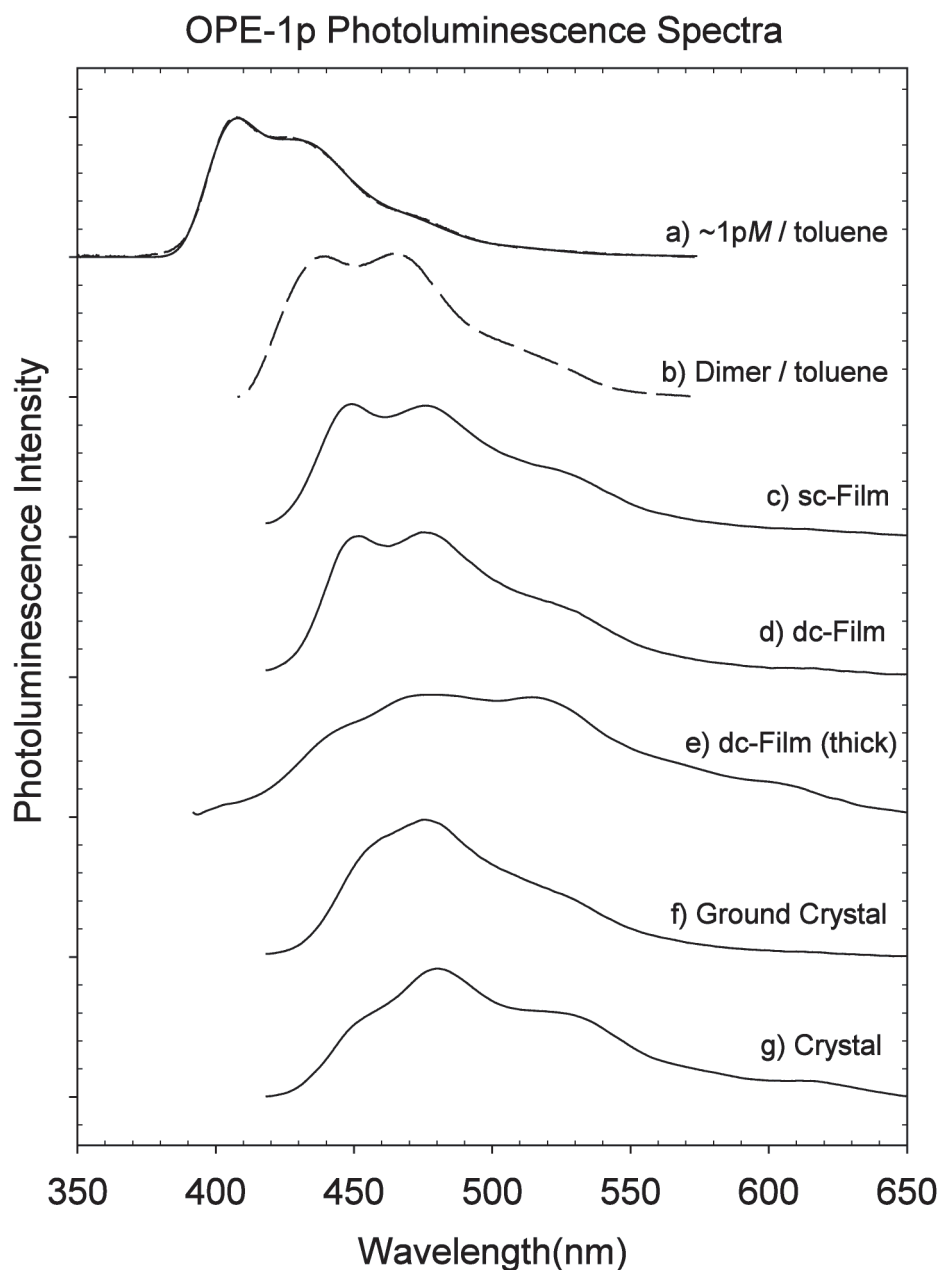


Figure 7.4. PL spectra of OPE-1p under different conditions,  $\lambda_{exc} = 325nm$ , unpolarized. a) Dashed: OPE-1p/toluene solution (very dilute), Solid: fit to Eqn. 7.4.2 b) OPE-1p/toluene solution (concentrated) where (a) has been subtracted. c) Spun-cast film using a dilute stock d) Drop-cast film using a dilute stock e) Drop-cast film using a concentrated stock f) Crystals that have been coarsely ground with mortar and pestle. g) Crystals formed in a chloroform solution

the concentration-dependent PL of OPE-1p solutions by spectral subtraction, as shown in Fig. 7.4b. This dimer state is strongly red-shifted[133] from the OPE-1p molecular PL, indicating that the lowest energy excited state from this interaction is dipole-allowed[99]. The vibronic separation in the OPE-1p dimer reveals an energy spacing of  $1515\text{cm}^{-1}$  that correlates with one of the observed vibrations obtained in the non-resonant Raman spectra (Fig. 7.3) of the drop-cast film ( $1525\text{cm}^{-1}$ ).

When OPE-1p has been allowed to slowly crystallize(Fig. 7.4g), the change in the ratio of the two bluest peaks changes dramatically, in addition to a very dramatic increase of the aggregate band at 620nm. XRD data reveals  $\pi - \pi$  stacking with rings  $< 7\text{\AA}$  separation which gives rise to red-shifted aggregate PL[134] as predicted by Bredas[99, 103]. When the crystal is powdered with a mortar and pestle, again the PL spectra changes dramatically (Fig. 7.4f) and a change in the ratio of the two bluest transitions is observed, suggesting extreme sensitivity of the PL to the nature of the sample environment.

The spun-cast film (Fig. 7.4c) show a similarly shaped spectrum to the extracted solution state dimer-profile, though red-shifted due to changes in solvation. This suggests that much of the film PL structure arises from dimer-like states, making these the strongest emissive species within the films. In addition, due to the high probability for stacking in these molecules, an aggregate[122] band is observable at 620nm that is related to excited states arising from association of more than two OPE-1p units. Drop-cast films (Fig. 7.4d) produce similar spectra to the spun-cast counterparts, although the bluest peak appears to be slightly diminished.



Shown in Fig. 7.4e is a film prepared by drop-casting a 1M solution using several deposition steps, where we see a much broader PL profile that stretches across the entire visible spectrum and possesses peak features of OPE-1p molecules, dimers and aggregates. This casting method appears to produce the widest variation of domain structures, which gives rise to a distribution of structures being probed by the laser, and explains why the PL has elements of crystalline, amorphous, and isolated phases. Therefore, from the series shown in Fig. 7.4, there is an overall trend in increasing PL shift to the red with decreasing OPE-1p intermolecular distances and more crystalline, tighter packed conformations.

#### **7.4.4 PL Temperature Dependence**

The dependence of the PL intensity on the morphology offers a unique opportunity to probe the melting behavior of these oligomer structures. The temperature-dependent PL intensity on spun-cast films (Fig. 7.5), can be correlated with the observed isotherms from the DSC (Fig. 7.1). Trapped solvent loss ( $T=305\text{K}$ ) is trivial to the PL decay as no strong change in solvent loss occurs as the total PL drops by  $< 2\%$  as the solvent boiling point is surpassed. As the solid-liquid phase transition is reached ( $T=405\text{K}$ ), the total integrated PL drops to  $25\%$ . During the cooling cycle, the integrated PL increases linearly with decreasing temperature, reaching  $39\%$  of the original value at room temperature. Therefore, the first heating/cooling cycle is not entirely reversible as the PL never recovers its original intensity. Although this is inconsistent with the observed reversibility of the DSC, it demonstrates the sensitivity of PL to

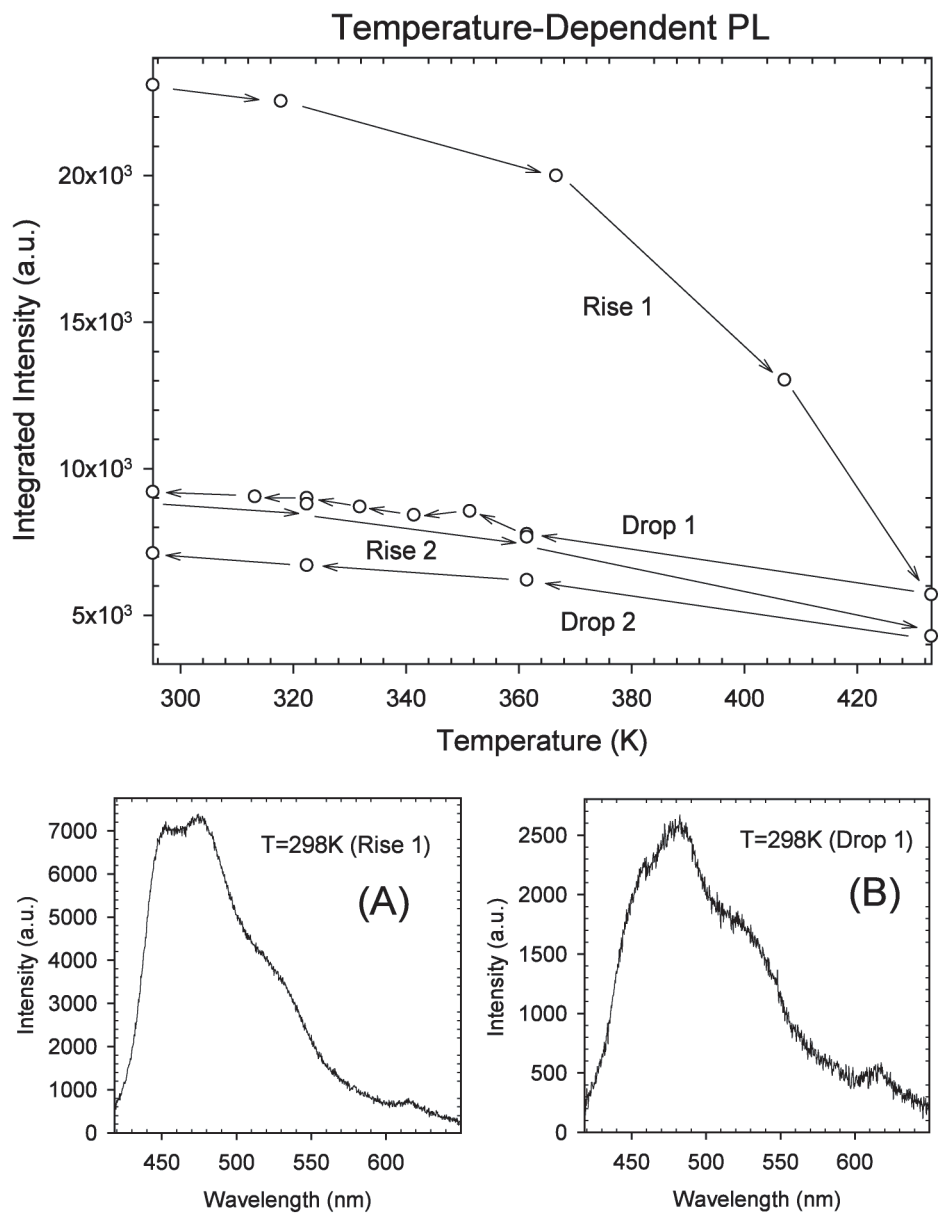


Figure 7.5. The spectrally-integrated PL of OPE-1p drop-cast film as a function of applied temperature. The arrows indicate the direction of the heating cycle (Rise 1,2) and cooling cycle (Drop 1,2).

probe local domains within the film, while DSC probes ensemble behavior.

As the film is cycled through repetitive heating-cooling ramps, the PL shows near reversibility as it tracks the cooling very closely. It reaches a slightly lower PL after the solid-liquid phase transition ( $\sim 21\%$ ). Subsequent cooling shows that the PL changes to  $\sim 30\%$  of its original intensity at room temperature. The irreversibility found in the second heating/cooling cycle ( $< 10\%$  PL change), however, is nowhere near as dramatic as that found in the first heating/cooling cycle ( $> 75\%$  PL change). This suggests a structural annealing process with increasing crystallinity due to removal of the metastable packing in the morphology of the cast film.

The shape of the PL spectrum provides a more systematic calibrant of the morphology changes. As a function of temperature, the PL switches between two forms as shown in Fig. 7.5: (A) a high-temperature liquid form and (B) a low temperature solid form. The changes in the PL are distinctly observed to occur coincident with the transitions found in the DSC. In specific, the initial metastable state of the OPE-1p film appears as (A) and there is no spectral change (apart from overall quenching) as the film is heated past the s-l phase transition. Even as the film cools initially, the spectral shape remains (A). However as the endothermic transitions are surpassed during cooling, the spectra approaches (B) until room temperature is reached. In subsequent heating up to the s-l phase transition, the spectra remains as (B), but switches to (A) as the melting point is surpassed. Further cooling shows that (A) turns into (B) only as the endothermic cooling begins. The behavior is consistent with a kinetically trapped metastable conformation for the oligomers.

Examination of the temperature-dependent PL shows strong irreversibility after the first melting cycle, which contradicts the DSC where strong reversibility is observed over several heating and cooling cycles. Clearly, the PL reflects only a small population of emissive states. However, considering the dramatic change in the PL observed, the meta-stable state must have significantly higher quantum efficiency compared to the dimer-state in order to account for the large disproportionality in population contribution. In polymeric variants it has been suggested that crystalline domains exhibit lower quantum efficiencies than more amorphous regions[120, 98, 121].

## 7.5 Optical Manipulation

The effect of the initial OPE-1p concentration (density) on the final melted form can be examined by performing time-monitored laser PL on the drop-cast and spun-cast films. The drop-cast films are expected to have a higher density of OPE-1p and form into a more ordered state (crystalline aggregate domains) because of it, while the spun-cast films tend to be more amorphous and have a lower OPE-1p density. These results are shown in Fig. 7.6. Here, we can see that over time under continuous irradiation, the PL intensity from the spun-cast films decays almost completely, within 2 hours while the PL from the drop-cast films decays to  $\sim 50\%$  of its original intensity, and remains indefinitely stable at that intensity (Inset of Fig. 7.6). In addition, the spectral shape of the film PL initially resembles the liquid form of Fig. 7.5(A), then transforms into Fig. 7.5(B) over time. Most notably the 450nm peak (molecule/dimer region)

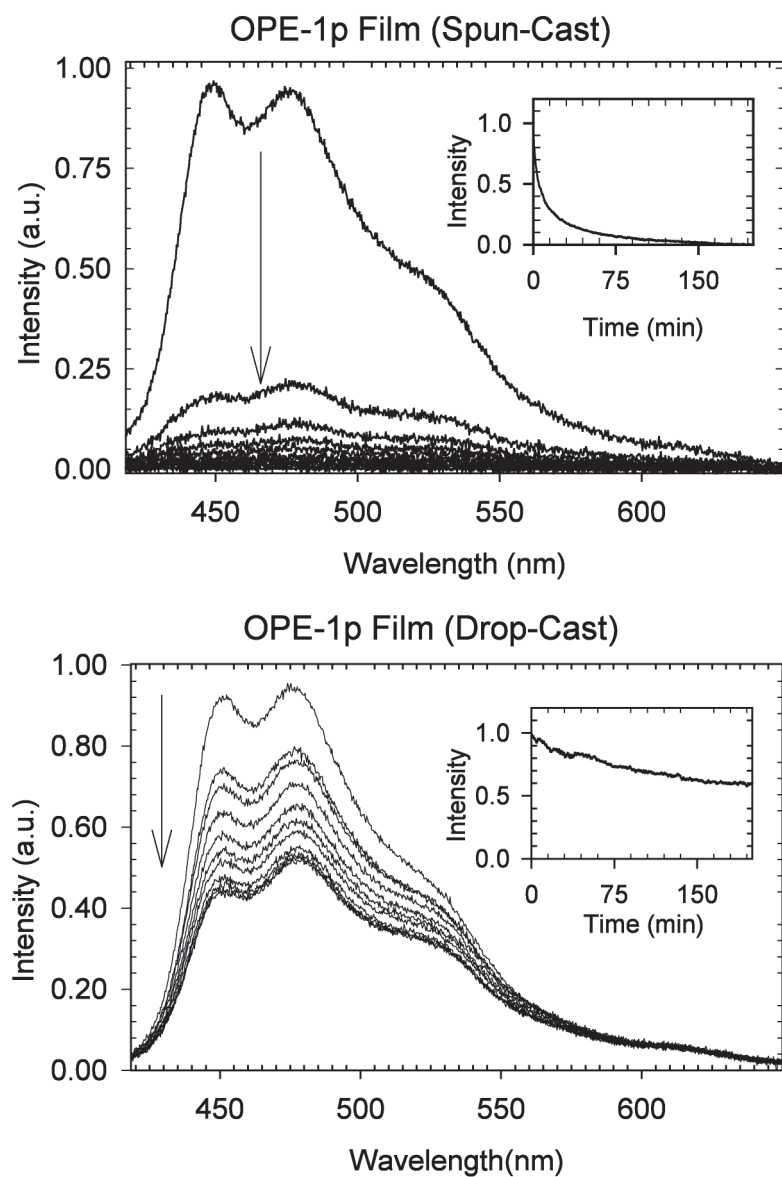


Figure 7.6. Photoluminescence spectra of OPE-1p films as a function of continuous irradiation time for spun-cast films (top) and drop-cast films (bottom). The curves (from top to bottom) represent spectra taken every 20 minutes after irradiation had begun. Insets show integrated PL Intensity as a function of irradiation time.

appears to quench more rapidly than the others (aggregate region).

The different PL behavior from the samples is examined more closely in Fig. 7.7, where we have integrated the intensity over three different spectral regions that correspond to dimer PL (I,II) and aggregate PL (III). In the spun-cast film, we clearly see that the intensity of all three approach zero toward the end of the experiment. However, the dimer states (I,II) clearly decay at a very different rate from the aggregate state (III). In the drop-cast films, the dimer regions behave differently from each other with Region I decaying to a lower overall PL than Region II. In addition, Region III does not decay below the initial intensity and in fact grows in intensity as Region I and Region II decrease in their intensity. In the dc-Film, all three regions appear to approach a stable intensity over the course of the experiment, which is in contrast to the spun-cast film where the intensity fades completely. All 3 regions in the drop-cast film also exhibit step-like increases in intensity at 5 min., 20 min. and 40 min. This phenomenon is also not present in the spun-cast film and could be due to discrete re-ordering of the structure that may correlate to the multiple kinetically trapped endothermic transitions observed in the DSC suggestive of a glassy or liquid crystalline-like ordering.

At a constant temperature (295K), OPE-1p films display strong PL intensity and position instability, even in inert environments(Fig. 7.7). In order to achieve this change in PL, there must be a corresponding change in the structure of the material, specifically, a transition from one thermodynamic phase to the other. This transformation is achieved by the dissipation of the absorbed optical energy through thermal deactivation processes. The heat released in this

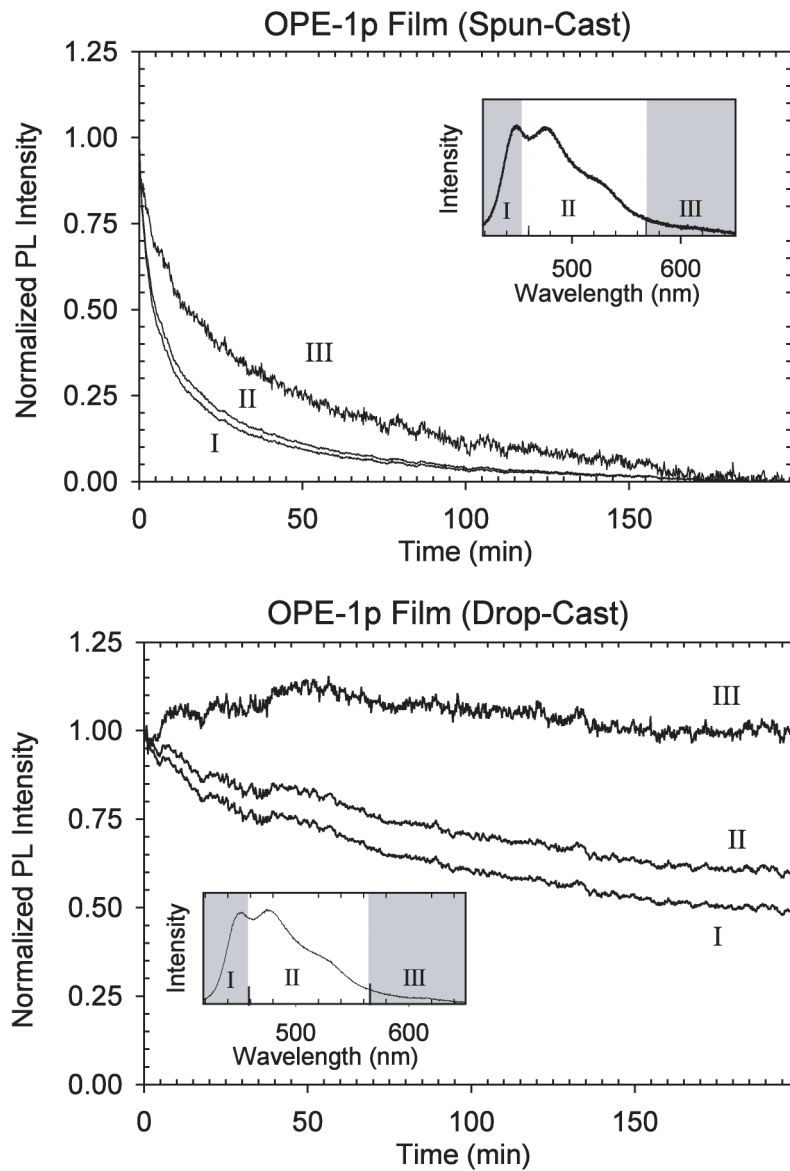


Figure 7.7. The spectrally integrated regions of the PL of OPE-1p films in 3 regions (I, II, III) shown in the insets, is plotted against continuous irradiation time for both spun-cast (top) and drop-cast (bottom) films.

way eventually builds up and causes the local temperature to increase eventually melting nearby chains. This process is very slow and strongly dependent on the applied laser power. The effect of this process on the stacking phenomenon can be seen in Fig. 7.6. The spun-cast sample is much less dense and the heat applied through optical pumping induces the PL to degrade completely (Fig. 7.7). This most likely occurs as a result of the wider separation between the OPE-1p domains. As the system absorbs heat, it begins melting, proceeding to the liquid-like phase. However, since the domains are spaced further apart, cooling into the thermodynamically favorable phase does not occur and the sample remains in the liquid phase. Since the PL signal appears to decay completely and very rapidly, the liquid phase must have very low quantum yield, very low optical cross section at the excitation wavelength, or both. The drop-cast film PL possesses very different characteristics. Although the film PL degrades, it does not degrade below 60% of its original intensity. In this case, the OPE-1p domains are spaced closely enough together that as the melting point is surpassed, cooling of the material proceeds into the thermodynamically stable phase, which is the final phase that the material will adopt when completely melted. In addition, if the PL spectra are spectrally analyzed over regions chosen to display primarily aggregate, dimer and monomer PL as done in Fig. 7.7, one can observe specific structural transformations occurring. In the drop-cast PL, while both monomer and dimer regions decay, the aggregate region increases in intensity, up to 120% of its original intensity. This represents an increase in the population of the aggregate phase, which is indicative of increased crystalline domains in the oligomer packing.



## 7.6 Energy Transfer

The ability to tune optical properties in these films via laser irradiation suggests they may be practical for applications in optical memory via the influence on energy transport pathways. Excitation migration plays an important role in the PL properties of OPE-1p. Migration efficiency will be very different among each thermodynamic phase, and will be strongly dependent on the size of the local domains. For example, migration can be strongly inhibited if the domain size is much smaller than the excitation diffusion length. Poorly formed films have a significant number of microscopic cracks that result in isolated islands of material, confining the migrating excitation. As heat is applied, the material melts and is allowed to cool, the cracks are reduced, freeing the excitation to migrate between islands. In fact, because of the strong similarity of the initially formed OPE-1p films and both the liquified OPE-1p film and the solution-phase dimer, we can infer that the island sizes are small enough that the dimer-PL experiences very little environmental (e.g. inter-dimer) influences.

The diffusion of an excitation in a 3D matrix of donors is a function of only 4 factors:  $D$ , the diffusion coefficient of the excitation;  $\tau$ , the donor lifetime;  $k_{EnT}(r - r_{DA})$ , the energy transfer rate; and  $N_A$ , the number of acceptors in the matrix. The rate of movement of the probability density( $\rho(\vec{r}, t)$ ) of an excitation in the case of 3D matrix of donors is[75]:

$$\frac{\partial}{\partial t}\rho(\vec{r}, t) = \left[ D\nabla^2 - \frac{1}{\tau} - \sum_{j=1}^{N_A} k_{EnT}(|\vec{r} - \vec{r}_j|) \right] \rho(\vec{r}, t) \quad (7.1)$$

From Eqn. 7.1, we can see that migration is favorable as long as diffusion

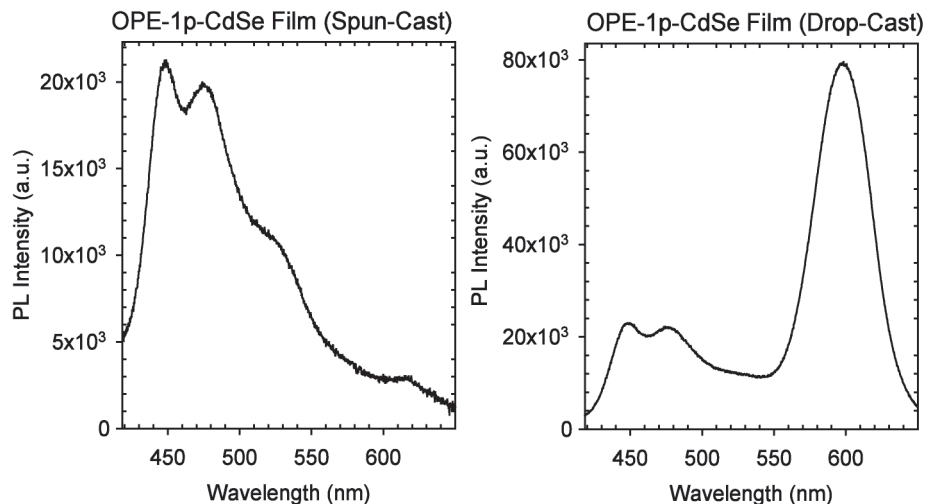


Figure 7.8. The PL spectra of CdSe QD-doped OPE-1p films in spun-cast (left) and drop-cast (right) forms made from *identical* stock solutions, immediately after exposure to light.

proceeds faster than the self-decay of the excitation. However, we also see that even in matrices with large migration rates, and consequently distances, the effective migration rate can be reduced linearly by the number of dopant acceptors.

Now that we understand the physical, energetic and temporal evolution of the host lattice PL, we can be confident about accurately interpreting the QD-doped system where excitation migration plays a role. In this system, several important changes occur that ultimately lead to the determination of the fate of the excitation. An important aspect of host-guest systems is electronic communication between the host and guest, which can sometimes be manifested as migration of an electronic or optical species. Excitation migration can be resonant or nonresonant (phonon-coupled), and coherent or diffusive. In this system we expect the mechanism of migration to be largely resonant and dif-

fusive, owing to the amorphous nature of the film.

Proof that a migration mechanism exists is given in Fig. 7.8, wherein a CdSe-OPE1p film is prepared under two conditions. In the spun-cast form, only OPE-1p PL is seen due to the low density of film material. Here, excitation migration is inhibited as the large gaps between domains prevent the excitation from hopping from domain to domain. However, as the domains are brought closer together, as is representative of the drop-cast sample, excitation migration increases. This increase in excitation migration means that the energy of optically absorbed photons will eventually make it to the lowest energy trap centers in the material. One of these trap centers is the QD, which acts as an optical reporter for this phenomenon. As can be seen in the drop-cast film of Fig. 7.8 this enhanced migration causes the CdSe to dominate the spectrum, nearly triple the intensity of the OPE-1p film.

Primarily, the character of the excitation will couple differently to CdSe in an energetically resonant sense, such that we can expect stronger energy transfer from more resonant states (like the dimer states). Due to the sensitivity of the meta-stable conformations to preparative means, we examine this system under different preparative protocols, in a spun-cast and in a drop-cast form, as shown in Fig. 7.8. Since we will be using CdSe in very small concentrations in the doped films ( $< 0.01\%$ ), it is safe to infer that *structurally* the OPE-1 system, which acts as the host, will largely behave as its undoped form. Colloidal additives are routinely added to plastics to improve properties without significant impact on the structure. Thus the primary effect of the CdSe QDs will be to act as structural probes, functioning *energetically* as excitation traps for

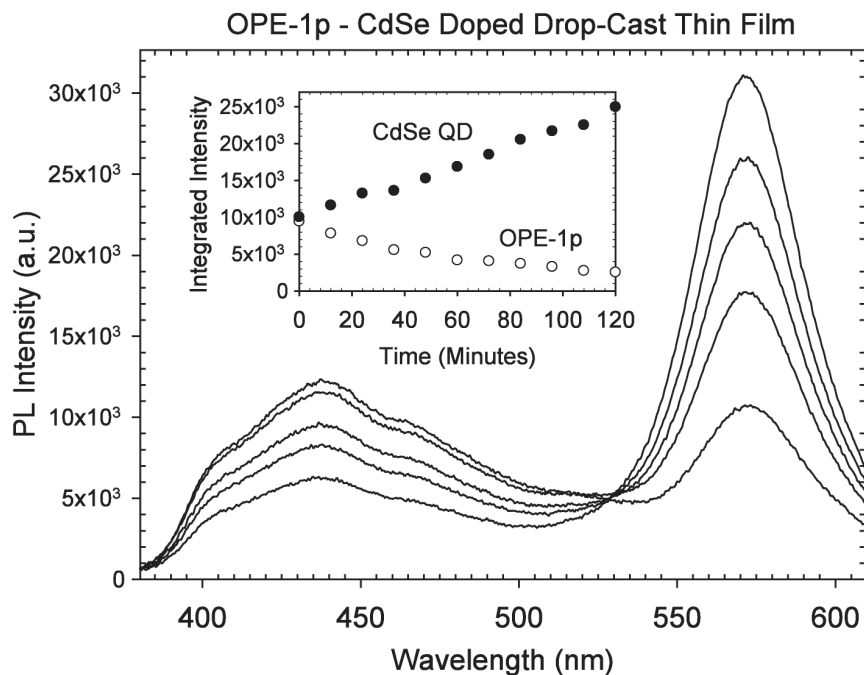


Figure 7.9. The PL spectra of CdSe QD-doped OPE-1p drop-cast film as a function of irradiation time. The inset shows the integrated intensities in the region of OPE-1p PL and CdSe PL

the migrating electronic excitation in the film. This is the nanometer analogue to acceptor-doped semiconductor lattices, where the exciton localizes at these excitation traps, and strong PL is observed from them, i.e. acceptor luminescence.

In the spun-cast form, we observe only pure OPE-1p PL and there is no evidence that CdSe is even present as a dopant. However, we observe a strong combination of OPE-1p and CdSe PL in the drop-cast sample. Therefore, the PL that we observe must be a cooperative effect between the OPE-1p and CdSe, since it is only the casting method that determines the overall PL. This result also gives an example of the amount of PL from CdSe that results from direct excitation of CdSe. At such low dopant concentrations, it is not surprising to

find that directly pumped CdSe PL is negligible. The difference in PL most likely results from differences in the film morphology and density. While both systems are excited by excitation light, the drop-cast film allows for much better energy migration, which in turn allows for better energy transfer to the dopant and eventually higher acceptor PL.

Under continuous illumination, the PL of the drop-cast system will evolve to predominantly CdSe PL, as shown in Fig. 7.9. The data shown in Fig. 7.9 represents an experiment wherein the casting conditions and dopant concentrations were optimized to produce the most dramatic effect on the PL intensity. Here, a thick dc-Film preparation has been used, analogous to Fig. 7.4e, such that a distribution of monomers, dimers and aggregate conformations are formed. Here, we clearly see that thermally induced changes (through optical excitation) in the OPE-1p system strongly influences the energetic dynamics of the film PL. Over time, the OPE-1p PL will decay, while the CdSe PL will rise at the same rate. This shift from OPE-1p as the dominant emitting species to CdSe as the dominant emitting species is reflected in the isosbestic point observed at 530nm.

### **7.6.1 Application: Optical Memory**

An important application of this system is an all-optical information storage and retrieval technology, an “Optical Memory” system. As a prototype, we show how photothermal melting of the OPE-1p matrix induces stronger energy transfer and migration to the CdSe QD, resulting eventually in increased CdSe PL (Fig. 7.9). Therefore, we have used a laser to optically ‘write’ into our film,

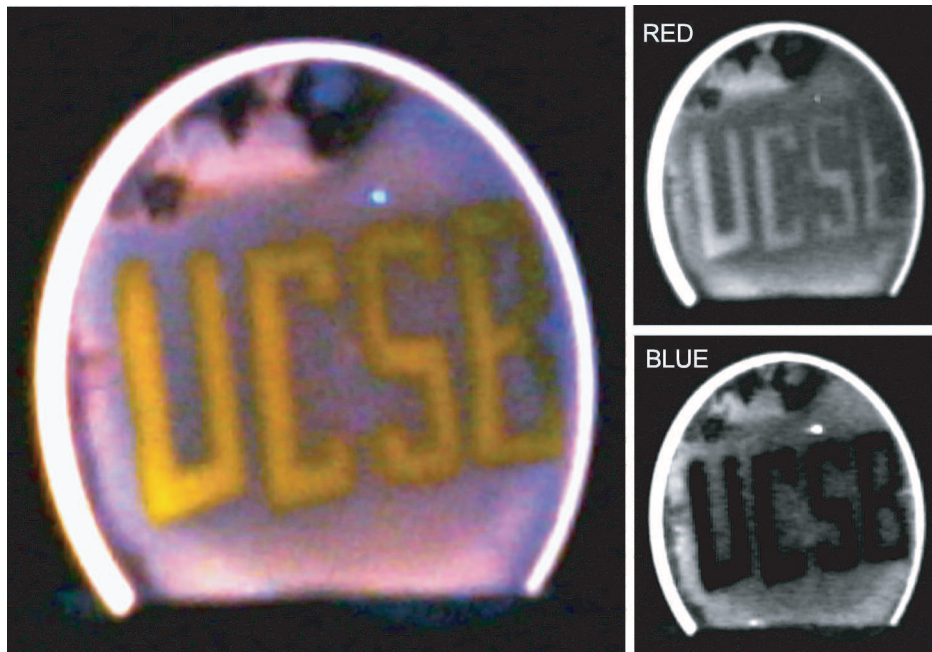


Figure 7.10. Digital photograph of a OPE-1p/CdSe sc-Film illuminated with UV light from a Hg-lamp where an optical mask has been used to etch "UCSB" prior to photography. Color decomposition profiles for this image are shown on the right for red and blue channels.

producing a spectrum with enhanced PL from CdSe. This enhanced PL is then optically 'read' by the monochromator/CCD we used, displaying an all-optical read-only memory system.

To demonstrate the feasibility of using this system, we show in Fig. 7.10 how an OPE-1p film can be "written" using only an optical mask and the collimated UV light from a Hg lamp. After exposure to this light under a mask with the letters "UCSB" cut-out, the mask was removed and a digital photograph of the film was immediately taken, while still under UV illumination. A RGB color decomposition was performed on the color image of Fig. 7.10 and the red and blue color channels are shown on the right hand side of Fig. 7.10.

Clearly, we can see from the blue channel that the OPE-1p PL (primarily blue-emitting) is not present in the regions of the lettering, but is very visible in the regions surrounding it. In the red channel, where CdSe is the primary emissive species, the letters clearly form a readable positive image. Therefore in this demonstration we have shown that exposure of the OPE-1p/CdSe film to UV-light results in primarily red light (from CdSe), the cause of which is directly linked to a photothermal melting and annealing of the OPE-1p domains resulting in more efficient energy migration and transfer to CdSe. As can be seen from Fig. 7.10, using a crude writing method, millimeter resolution can be achieved. Collimated light from the mask is shrunken using a lens system and sub-millimeter writing resolutions were achieved, though they could not be easily photographed.

Several factors exist that control the writing speed and volatility of the memory system. These include film casting density, CdSe dopant concentration, optical laser excitation power and CdSe dopant size.

## **7.7 Chapter Summary**

We have described three important areas to oligomer-QD interactions: 1) the effects of structural phase transitions on the excited states of the OPE-1p film, 2) optically addressing and manipulating the film and 3) using these hybrid films to control energy transfer and migration for the purposes of optical memory applications. The overall picture of the undoped OPE-1p film is that heating of the oligomer film induces a melting of the meta-stable film states

and annealing it to a more tighter, crystalline packing conformation. This is supported by, a red-shift in the overall PL, a distortion in the PL profile and a lowering of the quantum yield all indicating the formation of electronically coupled states as well as the presence of energy migration through the matrix. As the CdSe dopants are added, the energy migrating within the matrix is funnelled into the lower energy quantum dots and results in efficient QD PL. Since the annealing process is relatively slow, we can easily observe that the annealing process is coupled to the energy transfer process, and more importantly, the quantum dots act as the optical probes to this structural transformation.

There is much more that needs to be explored in the study of the excited state decay dynamics of this system, in particular elucidating the primary participants in the energy transfer process as well as applying this technology to more non-volatile memory systems (e.g. WORM, “Write Once Read Many”) through control of laser power.



# Bibliography

- [1] A.D. Yoffe. *Advances in Physics*, 50(1):1–208, 2001.
- [2] L. Brus. *Journal of Physical Chemistry*, 90:2555, 1986.
- [3] Jacques I. Pankove. *Optical Processes in Semiconductors*, pages 161–163. Dover Publications, Inc., 1971.
- [4] S.L. Cumberland, K.M. Hanif, A. Javier, G.A. Khitrov, G.F. Strouse, S.M. Woessner, and C.S. Yun. *Chemistry of Materials*, 14:1576–84, 2002.
- [5] M. G. Bawendi, W. L. Wilson, L. Rothberg, P. J. Carroll, T. M. Jedju, M. L. Steigerwald, and L. E. Brus. *Physical Review Letters*, 65(13):1623–6, 1990.
- [6] M. G. Bawendi, P.J. Carrol, William M. Wilson, and L. E. Brus. *Journal of Chemical Physics*, 96(2):946–954, 1992.
- [7] D.J. Norris and M.G. Bawendi. *Physical Review B-Condensed Matter*, 53:16338–16346, 1996.

- [8] L.M. Robinson, H. Rho, J.C. Kim, H.E. Jackson, L.M. Smith, S. Lee, M. Dobrowolski, and J.K. Furdyna. *Physical Review Letters*, 83(14):2797–2800, 1999.
- [9] S. A. Crooker, T. Barrick, J. A. Hollingsworth, and V. I. Klimov. *Applied Physics Letters*, 82(17):2793–2795, 2003.
- [10] Germar Schlegel, Jolanta Bohnenberger, Inga Potapova, and Alf Mews. *Physical Review Letters*, 88(13):137401/1–137401/4, 2002.
- [11] A.J. Nozik. *Annual Review of Physical Chemistry*, 52:193, 2001.
- [12] V.I. Klimov. *Journal of Physical Chemistry, B*, 104:6112, 2000.
- [13] S. A. Empedocles and M. G. Bawendi. *Science*, 278(5346):2114–2117, 1997.
- [14] D.V. Regelman, E. Dekel, D. Gershoni, E. Ehrenfreund, A.J. Williamson, J. Shumway, A. Zunger, W.V. Schoenfeld, and P.M. Petroff. *Physical Review B-Condensed Matter*, 64:165301, 2001.
- [15] C.A. Leatherdale, W.K. Woo, F.V. Mikulec, and M.G. Bawendi. *Journal of Physical Chemistry, B*, 31:7619, 2002.
- [16] R. Englman and J. Jortner. *Molecular Physics*, 18:145, 1970.
- [17] S.A. Empedocles and M.G. Bawendi. *Journal of Physical Chemistry, B*, 278:2114, 1997.
- [18] O. Chemiavskaya, L. Chen, M.A. Islam, and L. Brus. *Nano Letters*, 3:497, 2003.

- [19] G. Crosby and J.N. Demas. *Journal of Physical Chemistry, B*, 75:991, 1971.
- [20] B. Zorman and R.A. Friesner. *Journal of Chemical Physics*, 118:5937, 2003.
- [21] N.J. Turro. *Modern molecular photochemistry*. University Science Books, Mill Valley, Calif., 1991.
- [22] Al L. Efros, M. Rosen, M. Kuno, M. Nirmal, D. J. Norris, and M. Bawendi. *Physical Review B-Condensed Matter: Condensed Matter*, 54(7):4843–4856, 1996.
- [23] V. Turck, S. Rodt, O. Stier, R. Heitz, R. Engelhardt, U. W. Pohl, D. Bimberg, and R. Steingruber. *Physical Review B-Condensed Matter*, 61:9944, 2000.
- [24] N. Mataga, H. Chosrowjan, S. Taniguchi, Y. Shibata, N. Yoshida, A. Osuka, T. Kikuzawa, and T. Okada. *Journal of Physical Chemistry, A*, 106:12191, 2002.
- [25] Robert W. Meulenberg and Geoffrey F. Strouse. *Physical Review B-Condensed Matter*, 66(3):035317/1–035317/6, 2002.
- [26] V. I. Klimov, D. W. McBranch, C. A. Leatherdale, and M. G. Bawendi. *Physical Review B-Condensed Matter*, 60(19):13740–13749, 1999.
- [27] Todd D. Krauss, Stephen O’Brien, and Louis E. Brus. *Journal of Physical Chemistry, B*, 105:1725–1733, 2001.

- [28] A.L. Efros and M. Rosen. *Annual Review of Materials Science*, 30:475–521, 2000.
- [29] Manoj Nirmal and Louis Brus. *Accounts of Chemical Research*, 32:407–414, 1999.
- [30] David F. Underwood, Tadd Kippeny, and Sandra J. Rosenthal. *Journal of Physical Chemistry, B*, 105:436–443, 2001.
- [31] Xiaoyong Wang, Lianhua Qu, Jiayu Zhang, Xiaogang Peng, and Min Xiao. *Nano Letters*, 3(8):1103–6, 2003.
- [32] Artjay Javier, Travis Jennings, Donny Magana, and Geoffrey F. Strouse. *Applied Physics Letters*, 83:1423–5, 2003.
- [33] Olivier LaBeau, Philippe Tamarat, and Brahim Lounis. *Physical Review Letters*, 90(25):257404, 2003.
- [34] Margaret A. Hines and Philippe Guyot-Sionnet. *Journal of Physical Chemistry*, 100:468–471, 1996.
- [35] Xavier Michalet, Fabien Pinaud, Thilo D. Lacoste, Maxime Dahan, Marcel P. Bruchez, A. Paul Alivisatos, and Shimon Weiss. *Single Molecules*, 2(4):261–276, 2001.
- [36] Felix Koberling, Alf Mews, Gunther Philipp, Ute Kolb, Inga Potpova, Marko Burghard, and Thomas Basche. *Applied Physics Letters*, 81(6):1116–1118, 2002.
- [37] Stephen Empedocles and Mounji Bawendi. *Accounts of Chemical Research*, 32:389–396, 1999.

- [38] Brent R. Fisher, Hans-Juergen Eisler, Nathan E. Stott, and Mounji G. Bawendi. *Journal of Physical Chemistry, B*, 108:143–148, 2004.
- [39] Al. L. Efros and M. Rosen. *Physical Review Letters*, 78(6):1110–1113, 1997.
- [40] Thomas Basche. *Journal of Luminescence*, 76-77:263–269, 1998.
- [41] M. Kuno, D.P. Fromm, S.T. Johnson, A. Gallagher, and D.J. Nesbitt. *Physical Review, B*, 67:125304, 2003.
- [42] A.M. Kapitonov, A.P. Stupak, S.V. Gaponenko, E.P. Petrov, A.L. Rogach, and A. Eychmuller. *Journal of Physical Chemistry, B*, 103:10109–10113, 1999.
- [43] K.T. Shimizu, W.K. Woo, B.R. Fisher, and M.G. Bawendi. *Physical Review Letters*, 89(11):117401, 2002.
- [44] L. Besombes, K. Kheng, L. Marsal, and H. Mariette. *Physical Review B-Condensed Matter*, 65:121314, 2001.
- [45] R. G. Neuhauser, K.T. Shimizu, W.K. Woo, B.A. Emedocles, and M.G. Bawendi. *Physical Review Letters*, 85(15):3301–3304, 2000.
- [46] Arno Hartmann, Yann Ducommun, Eli Kapon, Ulrich Hohenester, and Elisa Molinari. *Physical Review Letters*, 84(24):5648, 2000.
- [47] Dmitri V. Talapin, Andrey L. Rogach, Andreas Kornowski, Markus Haas, and Horst Weller. *Nano Letters*, 1(4):207–211, 2001.

- [48] J.N. Demas. *Excited State Lifetime Measurements*. Academic Press, 1983.
- [49] J. Li, Y. A. Wang, W. Guo, J. C. Keay, T. D. Mishima, M. B. Johnson, and X. Peng. *Journal of the American Chemical Society*, 125:12567, 2003.
- [50] Peter J. Steinbach, Roxana Ionescu, and C. Robert Matthews. *Biophysical Journal*, 82:2244–2255, 2002.
- [51] Peter J. Steinbach. *Journal of Chemical Informatics and Computer Science*, 42:1476–1478, 2002.
- [52] C.P. Lindsey and G.D. Patterson. *Journal of Chemical Physics*, 73(7):3348–57, 1980.
- [53] Andrei A. Istratov. *Review of Scientific Instruments*, 70(2):1233–1257, 1999.
- [54] Aleksander Siemiarczuk, Brian D. Wagner, and William R. Ware. *Journal of Physical Chemistry, B*, 94:1661–1666, 1990.
- [55] T.J. Cornwell and K.F. Evans. *Astronomy and Astrophysics*, 143:77–83, 1985.
- [56] Anand T.N. Kumar, Leyun Zhu, J.F. Christian, Anrey A. Demidov, and Paul M. Champion. *Journal of Physical Chemistry, B*, 105:7847–7856, 2001.
- [57] H. Gzyl. *The Method of Maximum Entropy*. World Scientific, 1995.

- [58] J. Seufert, M. Rambach, G. Bacher, A. Forchel, T. Passow, and D. Hommel. *Applied Physics Letters*, 82(22):3946, 2003.
- [59] G.M. Credo, M.D. Mason, and S.K. Buratto. *Applied Physics Letters*, 74(14):1978–1980, 1999.
- [60] Y. Ebenstein, T. Mokari, and U. Banin. *Applied Physics Letters*, 80(21):4033–4035, 2002.
- [61] S. R. Cordero, P. J. Carson, R. A. Estabrook, G. F. Strouse, and S. K. Buratto. *Journal of Physical Chemistry, B*, 104(51):12137–12142, 2000.
- [62] Noseung Myung, Yoonjung Bae, and Allen J Bard. *Nano Letters*, 3(6):747–749, 2003.
- [63] T. Dannhauser, M. O’Neil, K. Johansson, D. Whitten, and G. McLendon. *Journal of Chemical Physics*, 90(23):6074–6, 1986.
- [64] Junichi Kimura, Shinya Maensomo, and Yukio Yamaguchi. *Nanotechnology*, 14:69–72, 2003.
- [65] K. T. Shimizu, R. G. Neuhauser, C. A. Leatherdale, S. A. Empedocles, W. K. Woo, and M. G. Bawendi. *Physical Review B-Condensed Matter*, 63(20):205316/1–205316/5, 2001.
- [66] B. C. Hess, I. G. Okhrimenko, R. C. Davis, B. C. Stevens, Q. A. Schulzke, K. C. Wright, C. D. Bass, C. D. Evans, and S. L. Summers. *Physical Review Letters*, 86(14):3132–3135, 2001.
- [67] Fazila Seker, Kathleen Meeker, Thomas F. Kuech, and Arthur B. Ellis. *Chemical Reviews*, 100(7):2505–2536, 2000.

- [68] Gerald J. Meyer, George C. Lisensky, and Arthur B. Ellis. *Journal of the American Chemical Society*, 110(15):4914–18, 1988.
- [69] Amjad Y. Nazzal, Lianhua Qu, Xiaogang Peng, and Min Xiao. *Nano Letters*, 3(6):819–822, 2003.
- [70] Robin R. Chandler and Jeffery L. Coffey. *Journal of Physical Chemistry*, 95(1):4–6, 1991.
- [71] Wilfried G J H M van Sark, Patrick L T M Frederix, Dave J Van den Heuvel, Hans C Gerritsen, Ageeth A Bol, Joost N J van Lingen, Celso de Mello Donega, and Andries Meijernik. *Journal of Physical Chemistry, B*, 105:8281–8284, 2001.
- [72] V. L. Colvin and A. P. Alivisatos. *Journal of Chemical Physics*, 97(1):730–3, 1992.
- [73] V.M. Agranovich and A.A. Maradudin. *Electronic Excitation Energy Transfer in Condensed Matter*. Modern Problems in Condensed Matter Sciences. North-Holland Publishing Company, 1982.
- [74] A.A. Lamola, N.J. Turro, P.A. Leermakers, and A. Weissberger. *Energy transfer and organic photochemistry*. Interscience Publishers, New York, 1969.
- [75] B. Di Bartolo and A. Karipidou. *Energy transfer processes in condensed matter*. Plenum Press, New York, 1984.
- [76] F. Bassani, G.C. La Rocca, D.M. Basko, and V.M. Agranovich. *Physics of the Solid State*, 41:701–703, 1999.



- [77] C.R. Kagan, C.B. Murray, and M.G. Bawendi. *Physical Review B-Condensed Matter*, 54(12):8633–8643, 1996.
- [78] M.L. Brongersma, J.W. Hartman, and H.A. Atwater. *Physical Review B-Condensed Matter*, 62:R16356–16359, 2000.
- [79] D.M. Willard, L.L. Carillo, J. Jung, and A. Van Orden. *Nano Letters*, 1:469–474, 2001.
- [80] N.C. Greenham, X.G. Peng, and A.P. Alivisatos. *Physical Review B-Condensed Matter*, 54:17628–17637, 1996.
- [81] W.U. Huynh, X.G. Peng, and A.P. Alivisatos. *Advanced Materials*, 11:923–927, 1999.
- [82] V.M. Agranovich, D.M. Basko, G.C. La Rocca, and F. Bassani. *Journal of Physics-Condensed Matter*, 10:9369–9400, 1998.
- [83] M. Sirota, E. Minkin, E. Lifshitz, V. Hensel, and M. Lahav. *Journal of Physical Chemistry, B*, 105:6792–6797, 2001.
- [84] C.E. Finlayson, D.S. Ginger, and N.C. Greenham. *Chemical Physics Letters*, 338:83–87, 2001.
- [85] M.L. Steigerwald and L.E. Brus. *Accounts of Chemical Research*, 23:183–188, 1990.
- [86] M. Knupfer, T. Pichler, M.S. Golden, J. Fink, M. Murgia, R.H. Michel, R. Zamboni, and C. Taliani. *Physical Review Letters*, 83:1443–1446, 1999.

- [87] M. Knupfer, E. Zojer, G. Leising, and J. Fink. *Synthetic Metals*, 119:499–502, 2001.
- [88] V. M. Agranovich, G. C. La Rocca, F. Bassani, H. Benisty, and C. Weisbuch. *Optical Materials*, 9:430–436, 1998.
- [89] C.J. Collison, V. Treemaneeekarn, W.J. Oldham, J.H. Hsu, and L.J. Rothberg. *Syn. Met.*, 119:515–518, 2001.
- [90] J. Cornil, D. Beljonne, J.P. Calbert, and J.L. Bredas. *Advanced Materials*, 13:1053–1067, 2001.
- [91] J. Cornil, J.P. Calbert, D. Beljonne, R. Silbey, and J.L. Bredas. *Synthetic Metals*, 119:1–6, 2001.
- [92] E. Frankevich, H. Ishii, Y. Hamanaka, T. Yokoyama, A. Fuji, K. Yoskino, A. Nakamura, and K. Seki. *Physical Review B-Condensed Matter*, 62:2505–2515, 2000.
- [93] L. Jones, J.S. Schumm, and J. M. Tour. *Journal of Organic Chemistry*, 62:1388–1410, 1997.
- [94] S.L. Huang and J.M. Tour. *Tetrahedron Letters*, 40:3347–3350, 1999.
- [95] C.B. Murray, C.R. Kagan, and M.G. Bawendi. *Annual Review of Materials*, 30:545–610, 2000.
- [96] L.C. Brousseau, J.P. Novak, S.M. Marinakos, and D.L. Feldheim. *Advanced Materials*, 11:447–449, 1999.

- [97] J.P. Novak and D.L. Feldheim. *Journal of the American Chemical Society*, 122:3979–3980, 2000.
- [98] Robert Deans, Jinsang Kim, Michelle R. Machacek, and Timothy M. Swager. *Journal of the American Chemical Society*, 122:8565–6, 2000.
- [99] J. Cornil, D.A. dosSantos, X. Crispin, R. Silbey, and J.L. Bredas. *Journal of the American Chemical Society*, 120:1289–1299, 1998.
- [100] E.M. Conwell. *Physical Review B-Condensed Matter*, 57:14200–14202, 1998.
- [101] J.R. Lakowicz. *Principles of Fluorescence Spectroscopy, 2nd Ed.* Kluwer Academic/Plenum: New York, 1999.
- [102] O. Schmelz, A. Mews, T. Basche, A. Herrmann, and K. Mullen. *Langmuir*, 17:2861–2865, 2001.
- [103] Z. Shuai and J.L. Bredas. *Physical Review B-Condensed Matter*, 52(19):13730–3, 1995.
- [104] R.W. Meulenberg and G.F. Strouse. *Journal of Physical Chemistry, B*, 105:7438–7445, 2001.
- [105] D.M. Basko, V.M. Agranovich, F. Bassani, and G.C. La Rocca. *Physica Status Solidi a-Applied Research*, 178:69–72, 2000.
- [106] A. Ruseckas, E. Namdas, M. Theander, M. Svensson, A. Yartsev, D. Zigmantas, M.R. Anderson, O. Inganäs, and V. Sundström. *Synthetic Metals*, 119:603–604, 2001.

- [107] Artjay Javier, C. Steven Yun, Joseph Sorena, and Geoffrey F. Strouse. *Journal of Physical Chemistry, B*, 107:435–42, 2003.
- [108] Thuc-Quyen Nguyen, Vinh Doan, and Benjamin J. Schwartz. *Journal of Chemical Physics*, 110(8):4068–78, 1999.
- [109] P. Wang, C.J. Collison, and L.J. Rothberg. *J. Photochem. Photobiol. A*, 144:63–8, 2001.
- [110] D.E. Fogg, L.H. Radzilowski, B.O. Dabbousi, R.R. Schrock, E.L. Thomas, and M.G. Bawendi. *Macromolecules*, 30:8433–39, 1997.
- [111] Ying Wang and Norman Herron. *Journal of Luminescence*, 70:48–59, 1996.
- [112] D.S. Ginger and N.C. Greenham. *Physical Review B-Condensed Matter*, 59(16):10622–9, 1999.
- [113] B.O. Dabbousi, M.G. Bawendi, O. Onitsuka, and M.F. Rubner. *Applied Physics Letters*, 66(11):1316–8, 1995.
- [114] Artjay Javier and Geoffrey F. Strouse. *Chemical Physics Letters*, 391:60–63, 2004.
- [115] Artjay Javier, C. Steven Yun, and Geoffrey F. Strouse. *Materials Research Society Proceedings*, 776:17–22, 2003.
- [116] J.E. Bernard, D.E. Berry, and F. Williams. In Baldassare Di Bartolo, editor, *Energy Transfer Processes in Condensed Matter*, volume 114 of *Series B: Physics*, pages 1–102. Plenum Press, 1983.

- [117] C. Klingshirn. In Baldassare Di Bartolo, editor, *Energy Transfer Processes in Condensed Matter*, volume 114 of *Series B: Physics*, pages 285–370. Plenum Press, 1983.
- [118] L.M. Herz, C. Silva, R.T. Phillips, S. Setayesh, and K. Mullen. *Chemical Physics Letters*, 347:318–324, 2001.
- [119] Klemens Brunner, John A.E.H. van Haare, Bea M.W. Langeveld-Voss, Herman F.M. Schoo, Johannes W. Hofstraat, and Addy van Dijken. *Journal of Physical Chemistry, B*, 106(27):6834–41, 2002.
- [120] Igor A. Levitsky, Jinsang Kim, and Timothy M. Swager. *Journal of the American Chemical Society*, 121:1466–72, 1999.
- [121] Jinsang Kim, Sean K. McHugh, and Timothy M. Swager. *Macromolecules*, 32:1500–7, 1999.
- [122] Hong Li, Douglas Powell, Randy K. Hayashi, and Robert West. *Macromolecules*, 31:52–8, 1998.
- [123] Simon Dellsperger, Florian Dotz, Paul Smith, and Christoph Weder. *Macromol. Chem. Phys.*, 201:192–8, 2000.
- [124] P. Avakian and R.E. Merrifield. *Physical Review Letters*, 13:541–3, 1964.
- [125] Uwe H.F. Bunz, Volker Enkelmann, Lioba Kloppenburg, David Jones, Ked D. Shimizu, John B. Caridge, Hans-Conrad zur Loye, and Gunter Lieser. *Chemistry of Materials*, 11:1416–24, 1999.

- [126] Daniel Ayuk Mbi Egbe, Carsten Peter Roll, Eckhard Birckner, Ulrich-Walter Grummit, Regina Stockmann, and Elisabeth Klemm. *Macromolecules*, 35(10):3825–37, 2002.
- [127] P. Wautelet, M. Moroni, L. Oswald, J. Le Moigne, A. Pham, and J.Y. Bigot. *Macromolecules*, 29:446–455, 1996.
- [128] David Ofer, Timothy M. Swager, and Mark S. Wrighton. *Chemistry of Materials*, 7:418–425, 1995.
- [129] S.C. Graham, D.D.C. Bradley, R.H. Friend, and C. Spangler. *Synthetic Metals*, 41-43:1277–1280, 1991.
- [130] Wei Zhao, Hong Li, Robert West, and John C. Wright. *Chemical Physics Letters*, 281:105–110, 1997.
- [131] Kikujiro Ishii, Hideyuki Nakayama, Kunio Tanabe, and Masataka Kawahara. *Chemical Physics Letters*, 198(1-2):236–239, 1992.
- [132] George A. Allen, Russel P. White, D. Paul Rillema, and Thomas J. Meyer. *Journal of the American Chemical Society*, 106:2613, 1984.
- [133] Liming Ding, Daniel A.M. Egbe, and Frank Karasz. *Macromolecules*, 37:6124–31, 2004.
- [134] C. S. Yun, A. Javier, and G.F. Strouse. unpublished results.